



UPPSALA
UNIVERSITET

UPTEC F 21008

Examensarbete 30 hp
Januari 2021

Investigation of High-Temperature Sensors for Tube Monitoring Applications

Andreas Sving



UPPSALA
UNIVERSITET

**Teknisk- naturvetenskaplig fakultet
UTH-enheten**

Besöksadress:
Ångströmlaboratoriet
Lägerhyddsvägen 1
Hus 4, Plan 0

Postadress:
Box 536
751 21 Uppsala

Telefon:
018 – 471 30 03

Telefax:
018 – 471 30 00

Hemsida:
<http://www.teknat.uu.se/student>

Abstract

Investigation of High-Temperature Sensors for Tube Monitoring Applications

Andreas Sving

This report covers the investigation of the next generation of sensors to be used in the sensor based tube system known as Sentusys(TM). One essential feature of the next generation of sensors is high-temperature endurance. The sensors (strain gauges and thermocouples) have been produced by means of thermal spraying techniques, short-pulse laser ablation and laser cladding. It has been found that the sensors seem to work in general, however, much research and development remain.

Keywords: sensor, high-temperature, thermal spray, laser micromachining, laser cladding, strain gauge, thermocouple

Handledare: Gustaf Sjöblom
Ämnesgranskare: Uwe Zimmermann
Examinator: Tomas Nyberg
ISSN: 1401-5757, UPTec F21 008

Sammanfattning

Sandvik har utvecklat ett sensorbaserat rörsystem under namnet Sentusys™. Sentusys™-rör innehåller integrerade och skyddade sensorer som används för fortlöpande övervakning av industriella processer och som är lämpade för farliga miljöer. Sensorerna är anslutna till en molntjänst. Via denna skickas information om processparametrar så som temperatur, töjning och vibration till användaren.

Nästa generation av sensorer för Sentusys™-rör är under utveckling. Dessa sensorer ska erbjuda en förbättrad funktionalitet och de ska noggrant kunna mäta ett flertal fysiska parametrar. En väsentlig egenskap hos dessa nya sensorer är att de även ska fungera vid mycket höga temperaturer, åtminstone upp till 600 grader Celsius. Sensorerna (töjningsgivare och termoelement) har tillverkats genom termisk sprutning, kortpuls laserablation och så kallad "laser cladding" – en påläggningsmetod som kompletterar termisk sprutning.

Syftet med detta arbete var att införskaffa mer kunskap om hur denna nästa generation av sensorer beter sig under förväntade förhållanden. Arbetet omfattade elektriska mätningar på sensorerna, statistisk analys av mätdata samt granskning gällande samband mellan mätdata och sensorproduktionsparametrar.

Det har visat sig att sensorerna tycks fungera överlag. Dock kvarstår fortfarande mycket forskning och utveckling.

Table of Contents

| | | |
|---------|--|----|
| 1 | Introduction | 1 |
| 2 | Background..... | 2 |
| 2.1 | Electrical resistance | 2 |
| 2.2 | Strain..... | 2 |
| 2.3 | Wheatstone bridge circuit..... | 2 |
| 2.4 | Four-terminal sensing | 3 |
| 2.5 | Strain gauge | 3 |
| 2.5.1 | Operating principle of the metal strain gauge..... | 4 |
| 2.5.2 | Gauge factor of the metal strain gauge..... | 4 |
| 2.5.3 | Transverse sensitivity..... | 5 |
| 2.5.4 | Mechanical hysteresis..... | 5 |
| 2.5.5 | Thermal drift..... | 6 |
| 2.6 | Thermocouple | 6 |
| 2.6.1 | Operating principle..... | 6 |
| 2.7 | Thermal spraying | 7 |
| 2.7.1 | Plasma spray..... | 8 |
| 2.7.2 | Flame spray | 9 |
| 2.8 | Laser ablation..... | 9 |
| 2.9 | Laser cladding..... | 10 |
| 3 | Experimental..... | 11 |
| 3.1 | Production of next generation of sensors | 11 |
| 3.1.1 | Thick film strain gauges | 11 |
| 3.1.1.1 | Coupons | 11 |
| 3.1.1.2 | Tubes..... | 12 |
| 3.1.2 | Laser cladde thermocouples..... | 13 |
| 3.2 | Evaluation of next generation of sensors..... | 14 |
| 3.2.1 | Thick film strain gauges | 14 |
| 3.2.1.1 | Strain response | 14 |
| 3.2.1.2 | Heat response | 15 |
| 3.2.2 | Laser cladde thermocouples..... | 16 |
| 4 | Results..... | 18 |
| 4.1 | Thick film strain gauges | 18 |
| 4.1.1 | Strain response | 18 |
| 4.1.2 | Heat response | 23 |

| | | |
|---------|---|----|
| 4.1.2.1 | Coupons | 23 |
| 4.1.2.2 | Tubes | 26 |
| 4.2 | Laser cladde d thermocouples..... | 31 |
| 5 | Discussion..... | 34 |
| 5.1 | Thick film strain gauges | 34 |
| 5.1.1 | Strain response | 34 |
| 5.1.2 | Heat response | 35 |
| 5.1.2.1 | Coupons | 35 |
| 5.1.2.2 | Tubes | 36 |
| 5.2 | Laser cladde d thermocouples..... | 37 |
| 6 | Conclusions | 39 |
| 6.1 | Thick film strain gauges | 39 |
| 6.2 | Laser cladde d thermocouples..... | 39 |
| 6.3 | Future work..... | 39 |
| 7 | References..... | 40 |
| | Appendix 1 - Strain response measurements for the coupons | 41 |
| | Appendix 2 - Heat response measurements..... | 66 |

1 Introduction

Sandvik has developed a sensor-based tube system known as Sentusys™. Sentusys™ tubes contain integrated and protected sensors that are used for in-process, online monitoring of industrial processes and are well-suited for hazardous environments. The sensors are connected to a cloud service, and through this, information about process parameters such as temperature, strain, and vibration is sent to the user. [1]

The first generation of Sentusys™ tubes uses welded thermocouples and glued strain gauges with plastic carriers that endures temperatures up to only 350 degrees Celsius. In the first generation tubes, long leads are used for connecting the sensors, which can cause extreme difficulties in the production.

The next generation of sensors for Sentusys™ tubes is currently being developed. These will offer enhanced functionality and the ability to accurately measure a wide assortment of physical parameters. One essential feature of these sensors is that they should be able to operate in high temperatures; up to at least 600 degrees Celsius. The sensors are produced by means of thermal spraying techniques, short-pulse laser ablation and laser cladding. Thermal spraying as a means of production was chosen because Sandvik already produces a range of metal powders suitable for the process. Furthermore, with thermal spraying, it is easy to produce sensors on big surfaces, in addition to short production cycles.

The purpose of this work is to gain more knowledge about how the next generation of sensors behave in anticipated conditions. The experimental part of this work includes electrical measurements on next generation sensors. Moreover, statistical analysis of measurement data, and dealing with the correlation between sensor production parameters and measurement data, is part of this work. [2]

This work was performed at Sandvik Intelligent Tube Systems/Specialized Business Units, a department within PA Tube, from August to December 2020.

2 Background

2.1 Electrical resistance

The electrical resistance of a material depends both on its electrical resistivity and its dimensions. In the ideal case, where the specimen of the material is uniform, and both the electric field and current density are constant throughout the specimen, the electrical resistance of the specimen can be calculated by equation 1, where R is the resistance, ρ is the material's resistivity, A is the cross-sectional area of the specimen and l is the length of the specimen.

$$R = \rho \frac{l}{A} \quad (1)$$

The electrical resistivity of a specimen is dependent on several factors, some of which include the material, the specimen's microstructure, and the temperature. The resistivity of most materials changes with the temperature. For moderate changes in temperature, the change in resistivity is approximately linear to the change in temperature. Equation 2 shows the linear approximation where T is the temperature, T_0 is a fixed reference temperature, ρ_0 is the resistivity at T_0 and α (called the temperature coefficient of resistivity) is an empirical parameter fitted from measurement data.

$$\frac{\rho(T)}{\rho_0} = 1 + \alpha(T - T_0) \quad (2)$$

Since equation 2 only is a linear approximation, α is different for different reference temperatures and the approximation only holds around the reference temperature. [3]

2.2 Strain

The term strain is mostly used to describe the elongation and contraction processes. Strain, ϵ , is defined as the relative change of length, $\Delta l/l_0$, of an object. Strain is positive for elongations, negative for contractions, and has the unit [meter/meter]. Thus, strain can be seen as an unitless ratio. Strain can be caused either by mechanical stress (e.g. tension or compression forces acting upon the object) or as a result of heating or cooling. [4, pp. 13,19]

2.3 Wheatstone bridge circuit

The Wheatstone bridge circuit allows for very small changes of resistance to be measured with great accuracy. An illustration of the Wheatstone bridge circuit can be seen in figure 1. The four branches of the Wheatstone bridge circuit are formed by the resistances R_1 to R_4 . The corner points 2 and 3 are the connections for the bridge's excitation, which usually is an applied and stabilized voltage U_B . The corner points 1 and 4 are the connections for the bridge output voltage v_o , i.e. the measurement signal.

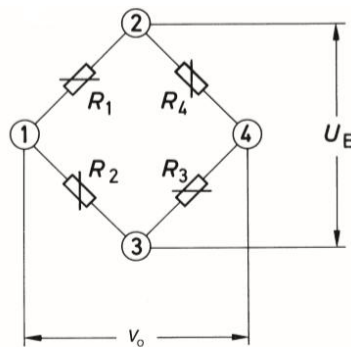


Figure 1: Illustration of the Wheatstone bridge circuit. K. Hoffmann, "An introduction to Stress Analysis and Transducer Design using Strain Gauges", HBM.

If a voltage U_B is applied to corner points 2 and 3, this voltage is divided up between R_1 and R_2 respectively R_4 and R_3 , as a ratio of the two resistances. The output voltage becomes:

$$V_o = U_B \left(\frac{R_1}{R_1 + R_2} - \frac{R_4}{R_3 + R_4} \right) \quad (3)$$

When the circuit is balanced, i.e. $R_1/R_2 = R_4/R_3$, the output voltage is zero. If e.g. R_1 is a strain gauge, the resistance in this branch will change when strain is applied. Thus, the circuit gets unbalanced and an output voltage, relative to the resistance change, can be measured. [4, pp. 126-128]

2.4 Four-terminal sensing

Four-terminal sensing, also known as Kelvin sensing, is an electrical impedance measuring technique which uses separate current-carrying and voltage-sensing leads. See figure 2 for measurement configuration.

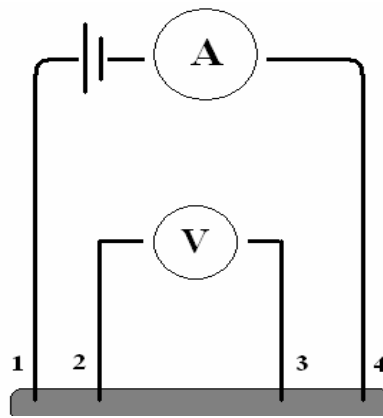


Figure 2: Four-terminal sensing. *Wikipedia contributors, "Four-terminal sensing", Wikipedia.*

Four-terminal sensing allows for more accurate impedance measurements since separation of the current-carrying and voltage-sensing leads eliminates the lead and contact resistance.

With four-terminal sensing, a current is supplied through the current-carrying leads. This generates a voltage drop across the impedance. The voltage-sensing leads connections are made immediately adjacent to the target impedance so that they do not include the voltage drop in the current-carrying leads or contacts. Since almost no current flows to the measuring instrument, the voltage drop in the voltage-sensing leads is negligible. [5]

2.5 Strain gauge

When measuring strain using strain gauges, the strain should ideally be transferred without loss from the object to the strain gauge. This requires a close connection between the strain gauge and the object experiencing the strain. There are many different types of strain gauges. The most usual type is resistive (e.g. metal and semiconductor) strain gauges. However, there are other types of strain gauges, some of which are capacitive and mechanical.

The strains measured with a strain gauge are often very small, thus, for a resistive strain gauge, the change of resistance is also very small and difficult or impossible to measure directly. Therefore, strain gauges need to be included in a measurement system. A usual approach is to include the strain gauge in some type of Wheatstone bridge circuit. [4, pp. 2-12, 15-16]

2.5.1 Operating principle of the metal strain gauge

The metal strain gauge's operating principle is based on the strain-resistance relationship of electrical conductors.

The resistance in an electrical conductor depends on its length and cross section area; thus, the resistance will change if the conductor is under strain. The strain-resistance relationship is described by equation 4, where $\Delta R/R_0$ is the relative change of resistance in the conductor and ν is Poisson's ratio. [4, pp. 12-13]

$$\frac{\Delta R}{R_0} = \varepsilon(1 + 2\nu) \quad (4)$$

However, also the resistivity in a conductor may change due to temperature changes and microstructural changes in the conductor. The change of resistance in a conductor then follows equation 5, where $\Delta\rho/\rho_0$ is the relative change of resistivity.

$$\frac{\Delta R}{R_0} = \varepsilon(1 + 2\nu) + \frac{\Delta\rho}{\rho_0} \quad (5)$$

When choosing the material of which a metal strain gauge is manufactured, the relative change of resistivity caused by microstructural changes, should be as small as possible in order to get as good strain-resistance relationship as possible over the complete measurement range, which can be seen in equation 5.

It has been found that the relationship between the relative change of resistance and the strain for conductors has different initial slopes for different materials. The different initial slopes can be explained by variations in the change in resistivity due to the microstructure. However, it has also been found that, for many materials, the slope changes to $\Delta R/R_0 = 2\varepsilon$ at the transition from elastic to plastic deformation, regardless of their initial slopes. Then, when it is assumed that the Poisson's ratio at the plastic deformation region has the value 0.5, equation 5 becomes:

$$\frac{\Delta R}{R_0} = \varepsilon(1 + 2 * 0.5) + \frac{\Delta\rho}{\rho_0} = 2\varepsilon + \frac{\Delta\rho}{\rho_0} = 2\varepsilon \quad (6)$$

Thus, the microstructural part $\Delta\rho/\rho_0$ becomes zero. Therefore, materials with also an initial slope of about 2ε are preferred in the construction on strain gauges, so that the influence of microstructural changes gets as small as possible over the whole elastic region. [4, p. 13]

2.5.2 Gauge factor of the metal strain gauge

The gauge factor, i.e. the strain gauge's sensitivity, is the relationship between the relative change of resistance and the strain for a strain gauge in its active direction. The active direction is set by the direction of the conducting paths of the measuring grid, see figure 3.

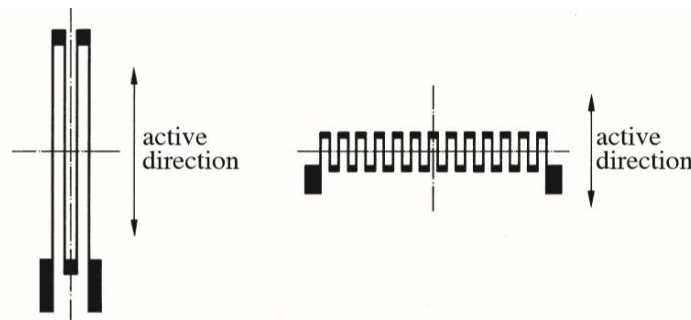


Figure 3: A strain gauge's active direction. K. Hoffmann, "An introduction to Stress Analysis and Transducer Design using Strain Gauges", HBM.

The difference between the gauge factor and the slope of the relationship between the relative change of resistance and the strain for conductors, mentioned in section 2.5.1, is that the gauge factor is a parameter for the complete strain gauge, including influences from the measurement grid's configuration as well as the strain transfer conditions into the measurement grid.

The gauge factor, represented by the symbol k , is expressed by the ratio of the relative change of resistance and the strain, as shown in equation 7.

$$k = \frac{\Delta R/R_0}{\varepsilon} \quad (7)$$

The gauge factor's units are $[(\Omega/\Omega)/(\text{m/m})]$, in practice they cancel out so that k appears as an unitless ratio. Average gauge factors for strain gauges with some regular alloys can be seen in table 1. [4, pp. 53-54]

| Measurement grid alloy | Composition [%] | Average gauge factor, k |
|------------------------|----------------------------|---------------------------|
| Constantan | 57 Cu, 43 Ni | 2.05 |
| Karma | 73 Ni, 20 Cr, res. Fe + Al | 2.1 |
| Nichrome V | 80 Ni, 20 Cr | 2.2 |
| Platinum-tungsten | 92 Pt, 8 W | 4.0 |

Table 1: Average gauge factors for strain gauges with some regular alloys. *K. Hoffmann, "An introduction to Stress Analysis and Transducer Design using Strain Gauges", HBM.*

2.5.3 Transverse sensitivity

A change of resistance can also be observed for strain transverse to the active direction, although usually very slight changes when compared to changes of resistance for strains in the active direction. The geometry of a strain gauge is usually configured to minimize transverse strain effects.

A transverse gauge factor, k' , can be found similarly to the (standard) gauge factor, k . The transverse sensitivity, q , is then defined as the ratio between the transverse gauge factor and the gauge factor, see equation 8. [4, pp. 56-57]

$$q = \frac{k'}{k} \quad (8)$$

2.5.4 Mechanical hysteresis

Mechanical hysteresis of a strain gauge is the difference in the measured value for rising and falling strain loadings. One specific definition of hysteresis of a strain gauge, with respect to universal test conditions, is the following. Hysteresis is the largest difference at the abscissa of a curve for rising and falling strain loadings through a complete strain cycle with extreme values of $+1000 \mu\text{m/m}$, $-1000 \mu\text{m/m}$, $-1000 \mu\text{m/m}$, and $+1000 \mu\text{m/m}$, see figure 4.

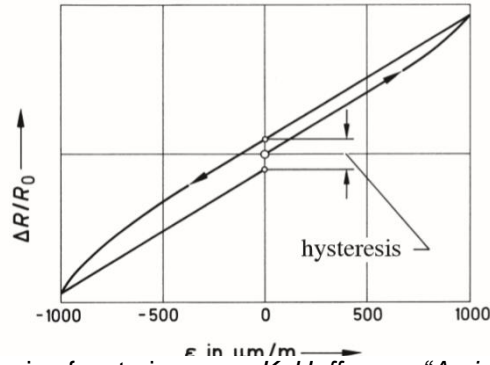


Figure 4: Definition of hysteresis of a strain gauge. K. Hoffmann, "An introduction to Stress Analysis and Transducer Design using Strain Gauges", HBM.

2.5.5 Thermal drift

Thermal drift is non-reversible zero-point changes in the strain gauge. Thermal drift is mainly caused by microstructural changes and oxidation or corrosion of the measuring grid. It may also be due to stress relief in the strain gauge as a result of thermal influences. [4, p. 67]

2.6 Thermocouple

A thermocouple is made up out of two different electrical conductors, forming an electrical junction at one end. A thermocouple produces a temperature dependent voltage as a result of the thermoelectric effect. This voltage can be used to measure the temperature at the junction. The voltage produced by a thermocouple is generally low, in the microvolt range per degree Celsius temperature difference. Even though the current that flows is very low, power can be generated by a single thermocouple.

In difference to most other temperature measuring devices, a thermocouple is self-powered and requires no external excitation. The biggest disadvantage with thermocouples is the accuracy; errors less than one degree Celsius are difficult to achieve. On the other hand, thermocouples can measure a wide range of temperatures, so they are well suited for extreme temperatures. [6]

2.6.1 Operating principle

The operating principle of the thermocouple is based on the thermoelectric effect, or more precisely the Seebeck effect.

The Seebeck effect refers to the electromotive force that occur whenever there is a temperature gradient in an electrical conductor. Under open-circuit conditions, the voltage gradient is directly proportional to the temperature gradient in a conductor, which can be seen in equation 9, where ΔV is the voltage gradient, $S(T)$ is a temperature-dependent material property (known as the Seebeck coefficient), and ΔT is the temperature gradient.

$$\Delta V = -S(T)\Delta T \quad (9)$$

The configuration principle for a thermocouple used for temperature measurements is shown in figure 5. There are three temperature regions marked out, the desired junction temperature T_{junc} , a known reference temperature T_{ref} at the other ends of the thermocouple conductors (often at the input to the measurement apparatus) and the temperature inside the measurement apparatus, T_{meas} . Here, the thermocouple conductors are made up out of the materials A and B. Inside the measurement apparatus material C (usually copper) is used for conductors.

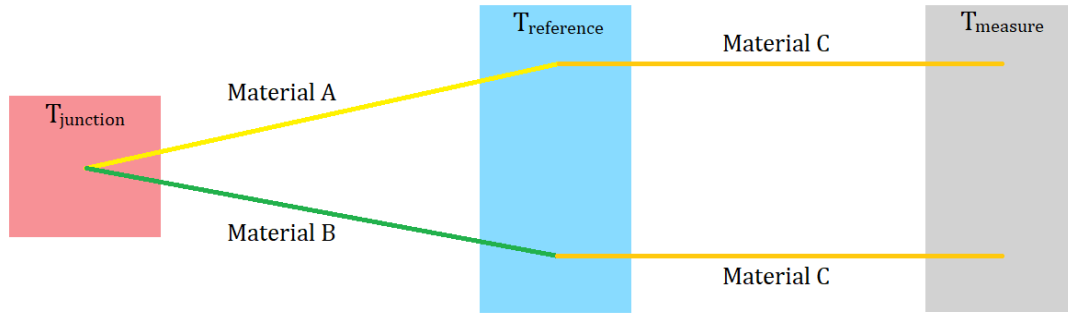


Figure 5: The configuration principle for a thermocouple used for temperature measurements.

Since materials *A* and *B* have different Seebeck coefficients, there will be a potential difference between the two thermocouple conductors. This difference in potential can then be used to calculate T_{junc} . From the open end of the thermocouple to the measurement point, both conductors are extended with the same material *C*, with the same Seebeck coefficients. Therefore, there will be no additional potential difference between the two conductors after T_{ref} . This results in that the voltage measured at T_{meas} is the same voltage as at T_{ref} . The measured voltage is shown in equation 10, where $S_+(T)$ and $S_-(T)$ is the Seebeck coefficient of the materials of the conductor attached to the positive and negative terminals of the measurement apparatus respectively.

$$V_{meas} = \int_{T_{ref}}^{T_{junc}} S_+(T) - S_-(T) dT \quad (10)$$

Equation 10 can be solved for T_{junct} from V_{meas} if T_{ref} , $S_+(T)$, and $S_-(T)$ are known. [6]

One of the commonly used thermocouples is the K-type thermocouple, which is made out of chromel ($Ni_{90}Cr_{10}$) and alumel ($Ni_{95}Mn_2Si_2Al_1$). [7]

2.7 Thermal spraying

Thermal spraying is a family of coating processes in which softened or molten particles of various materials are sprayed at high velocities onto a surface, on which they flatten out ('splat') and adhere, to form a cohesive coating. Thermal spraying processes vary considerably with regard to heat input to the target substrate and the bonding process is mainly mechanical. Thermal spraying as a concept is illustrated in figure 6.

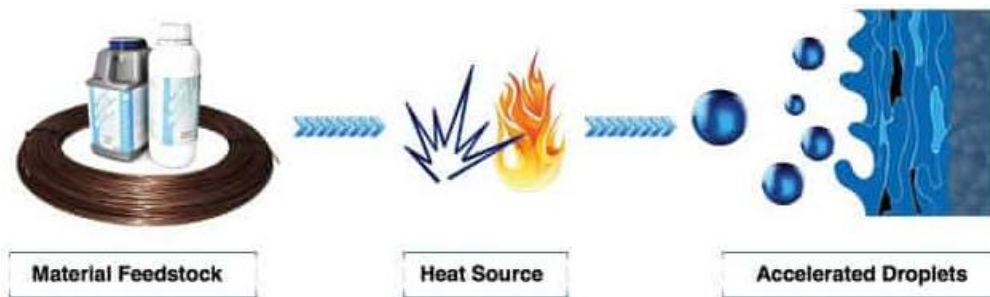


Figure 6: The principle of thermal spraying. *Metallisation Limited, "Introduction to Thermal Spray and Engineering Applications"*.

Thermal spraying techniques can provide coatings with various materials, including metals, ceramics, plastics and composites. The coating thickness ranges from 20 micrometers to several millimeters and can be deposited over a large area at high deposition rate, depending on spraying technique and the feedstock. The feedstock is usually in either wire or powder form. A combustion process or electrical arc discharge is usually used as the energy source to heat the ejected material. [8] [9]

2.7.1 Plasma spray

In plasma spraying processes (illustrated in figure 7), a jet of plasma with temperature in the order of 10 000 degrees Celsius is produced. The plasma is most often created in an electric arc between the nozzle (acting as an anode) and a cathode inside the plasma gun. The feedstock material (usually in powder form) is injected into the plasma jet in front of the nozzle, in which the material is softened or melted and propelled towards the target substrate at a high velocity. The material strikes and 'splats' onto the substrate, creating a strongly adherent, cohesive coating.

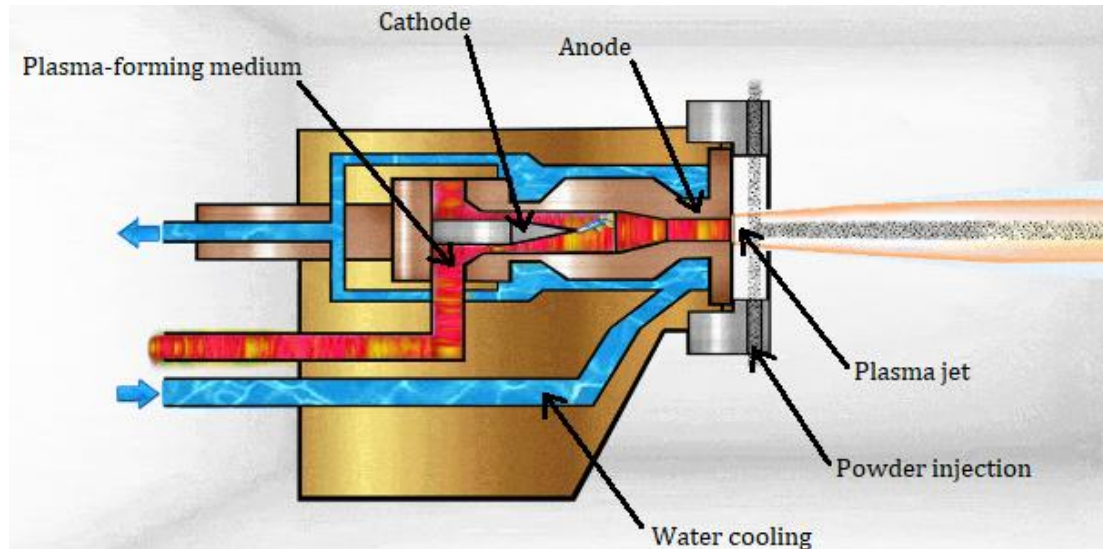


Figure 7: Plasma spraying process. *Metallisation Limited, "Plasma Spray"*.

There are many different types of plasma spraying configurations, of which the configuration illustrated in figure 7 is the most common. The different types can be categorized by various properties stated in table 2. [8] [10] APS is usually the best choice for spraying ceramic materials.

| | | | |
|-------------------------------|--|--|--|
| Plasma jet generation: | Inside a direct current, high power electric arc (DC plasma) | Via induction from a coil around the plasma jet (induction Plasma or RF plasma) | |
| Plasma-forming medium: | A gas (GSP, gas-stabilized plasma) | Water or other suitable liquid (WSP, water-stabilized plasma) | A hybrid of GSP and WSP |
| Spraying environment: | In air (APS, atmospheric plasma spraying) | In a closed chamber, filled with an inert gas of evacuated (CAPS, controlled atmosphere plasma spraying). Variations of CAPS are: High-pressure plasma spraying (HPPS), Low-pressure plasma spraying (LPPS), Vacuum plasma spraying (VPS). | Under water (UPS, Underwater plasma spraying). |

Table 2: Plasma spraying categories.

2.7.2 Flame spray

In flame spraying processes (illustrated in figure 8), an oxygen-fuel mixture combustion flame is used to melt the feedstock (usually in the form of a wire). The melted material is then atomized, usually by compressed air, to create a spray stream that will coat the target substrate. [11]

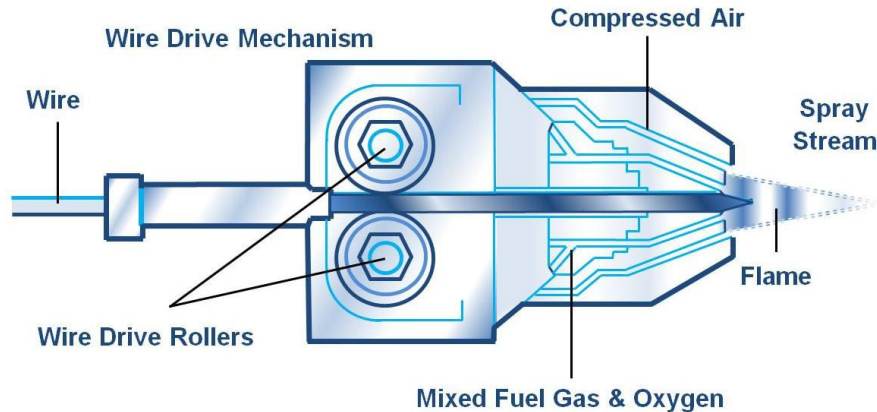


Figure 8: Flame spraying process. *Metallisation Limited, "Flame Spray Equipment"*.

The high-velocity oxygen-fuel (HVOF) flame spraying process is different from other flame spraying processes. The gas leaving the nozzle is at supersonic speeds and the feedstock is usually in powder form. HVOF produces a very strong and dense coating with very low porosity and oxide inclusion. [12]

2.8 Laser ablation

Laser ablation is the process in which material is removed from an object's surface by irradiating it with a laser beam. Usually a pulsed laser with pulse duration ranging from femtoseconds to milliseconds is used.

With longer durations (ns or slower), the irradiated material is heated by the absorbed energy and either evaporates or sublimates. Heat is also transferred to surrounding material, which can cause micro-cracking in the object. Un-evaporated material can be ejected and adhere to the surface, also, the surrounding surface itself can be damaged during the ablation. With ultra-short durations (ps or faster), the irradiated material is typically converted to a plasma. This results in practically no heat transfer to the surrounding material, no micro-cracking, and an undamaged surrounding surface. See figure 9 for illustration and comparison between long-pulse laser beam ablation compared to ultrashort laser pulse ablation.

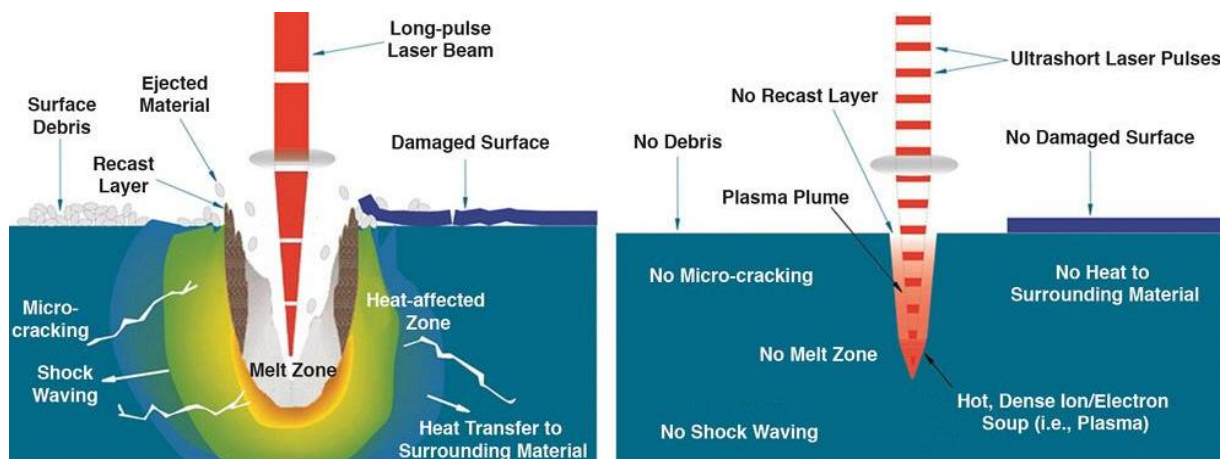


Figure 9: Long-pulse laser beam ablation compared to ultrashort laser pulse ablation. *E. Lundin, "Small-scale laser cutting for stent, tube fabrication", The tube & Pipe Journal*.

The depth over which the laser energy is absorbed depends on the material's optical properties, and the laser's wavelength and duration. The mass ablated from the object per laser pulse is referred to as ablation rate. [13] [14]

2.9 Laser cladding

Laser cladding (also known as laser metal deposition or direct energy deposition) is a welding method to deposit material to a substrate using a focused laser beam. Feedstock material, in the form of a powder or a wire, is fed onto the substrate, which at the same time is being melted by the laser forming a so called "melt pool" onto the substrate. Four different feedstock material feeding systems are shown in figure 10. Moving the substrate (if the laser nozzle is stationary) or the laser nozzle (if the substrate is stationary) allows the "melt pool" to solidify and adhere to the substrate, thus creating a solid track. [15] A big advantage with laser cladding is that overlapping layers can be realized without masking, which is needed if thermal spray would be employed.

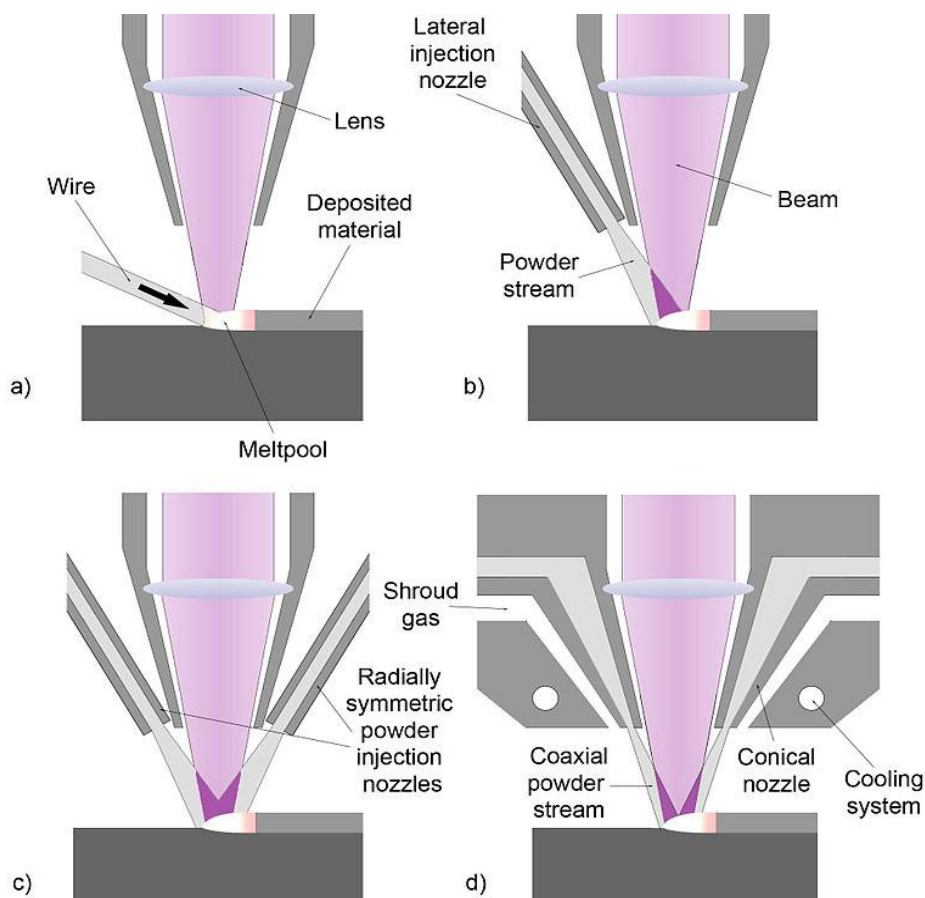


Figure 10: Different types of feeding systems regularly used in laser cladding. *Wikipedia contributors, "Cladding (metalworking)", Wikipedia.*

3 Experimental

3.1 Production of next generation of sensors

3.1.1 Thick film strain gauges

Ideally, the produced strain gauges should range from $100\ \Omega$ to $1000\ \Omega$, in order to permit the usage of inexpensive voltage measurement hardware in future Sentusys™ installations.

Strain gauges have been manufactured on flat square pieces of AISI 316 stainless steel (here referred to as coupons), tubes made of AISI 316 stainless steelstrips that have been welded together, and one tube of unknown carbon steel.

3.1.1.1 Coupons

The coupon sensors were produced by first coating the substrate's surface with three layers of materials. The coatings were made using atmospheric plasma spraying (APS). The first layer is a coating of "Ni alloy A" (Ni-A). The feedstock used in the APS process was Ni-A powder. The second layer is a dielectric coating of metal oxide (MeO). For this the feedstock was MeOpowder. The third and uppermost layer is a second coating of Ni-A, using the same feedstock as for the first layer. See figure 11 for illustration of the coatings. The purpose of the first coating of Ni-A is to give the MeOcoating a better surface to adhere to. Before any spray processing, the surface was given a light grit blast treatment in order to clean and roughen the surface.

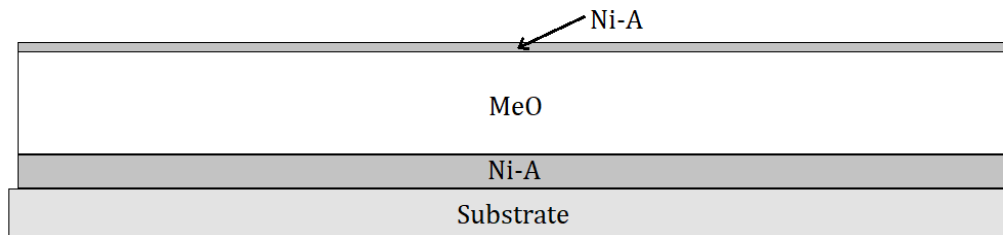


Figure 11: The layered coatings on the coupons.

The strain gauge's pattern was made in the uppermost Ni-A layer through laser ablation. The laser ablation was made with both nanosecond pulses and picosecond pulses, both with a wavelength of 1064 nm. Nanosecond pulse laser ablation were tested because it is in general both faster and cheaper than e.g. picosecond laser ablation. For different samples, the laser's focal position and the dimensions of the strain gauges were altered as production parameters to be investigated. A coupon with both picosecond pulse and nanosecond pulse ablated strain gauges is shown in figure 12.

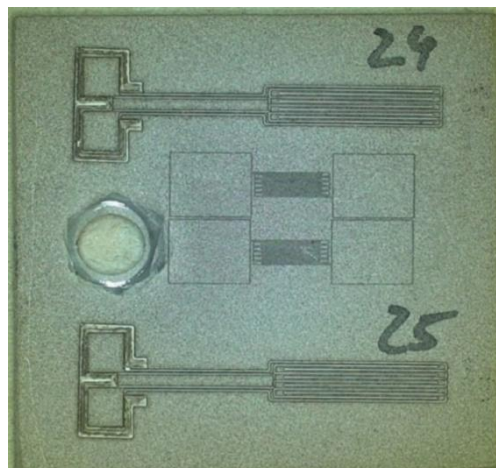


Figure 12: A coupon with strain gauges. The smaller sensors (center) are made with picosecond pulse laser ablation, the bigger ones with nanosecond pulse laser ablation.

3.1.1.2 Tubes

All the 316 steel tubes were coated in the same way as the coupons in section 3.1.1.1, with the exception that the feedstock used in the APS process had some variations. For some of the tubes, the Ni-A powder grain sizes was the same as for the coupons, for other tubes, a finer Ni-A powder was used. The MeO feedstock was the same as for the coupons.

The laser ablation on these APS tubes was made with the same nanosecond pulse laser as for the coupons, however with a slight variation in the laser set-up. For different samples, the laser's focal position and the dimensions of the strain gauges were altered as production parameters to be investigated. This was done in order to emulate for the lack of a 3D curvature compensation. A comparison between a strain gauge on one of the fine grained tubes and on one of the coarse grained tubes is shown figure 13.

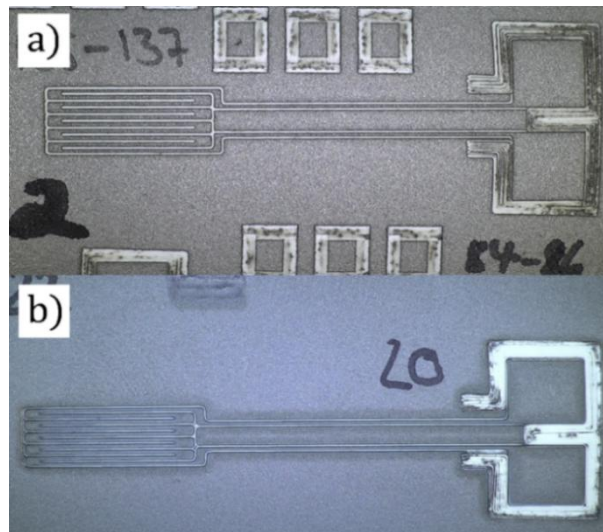


Figure 13: a) A strain gauge on a coarse powder tube. b) A strain gauge on a fine powder tube.

The carbon steel tube was coated by using flame spraying instead of plasma spraying. This tube was first coated with a layer of MeO using a flame spray gun (acetylene and oxygen). Then, an “advanced Ni alloy” (Ni-B) coating was dispensed onto the MeO layer using high-velocity oxygen-fuel (HVOF) spraying.

The ablation on this flame sprayed tube was made with both picosecond pulse laser (for the strain gauges) and nanosecond pulse laser (for everything else). Figure 14 shows the flame sprayed tube and figure 15 shows one of the picosecond pulse ablated strain gages. After the laser ablation, a black surface underneath the Ni-B layer can be seen. This indicates that the MeO layer was damaged due to excessive heat during the HVOF spraying process.

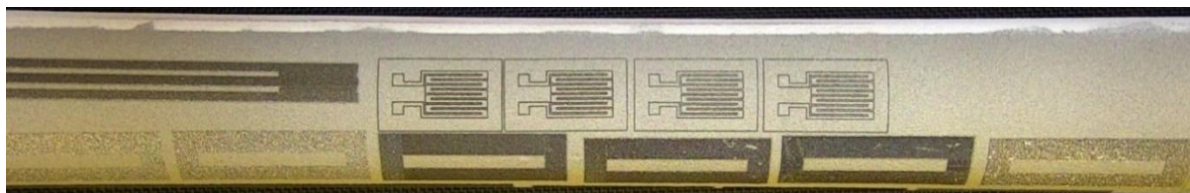


Figure 14: The flame sprayed tube.

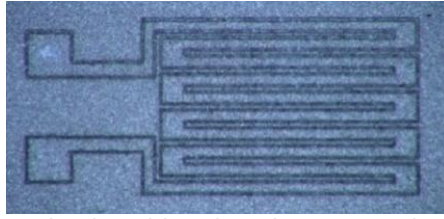


Figure 15: A picosecond pulse ablated strain gage on the flame sprayed tube.

Concerning all tubes; neither the nanosecond pulse nor the picosecond pulse laser setups were equipped with any kind of galvano-optical 3D correction to compensate for the curvature of the tubes.

3.1.2 Laser clad thermocouples

Thermocouples have been manufactured on one 316 stainless steel tube. The tube was coated using APS for the first two layers. The first layer is a coating of Ni-A, the feedstock used for this coating was Ni-A powder. The second layer is a coating of MeO. For this the feedstock was MeO powder.

Onto the coating of dielectric MeO, perpendicularly crossing tracks of Ni-A respectively Ni-C ("Ni alloy C"), forming the thermocouple junctions, were made using laser cladding.[16]The feedstock used was Ni-A powder and Ni-C powder respectively. Figure 16 shows one of the laser clad thermocouples.

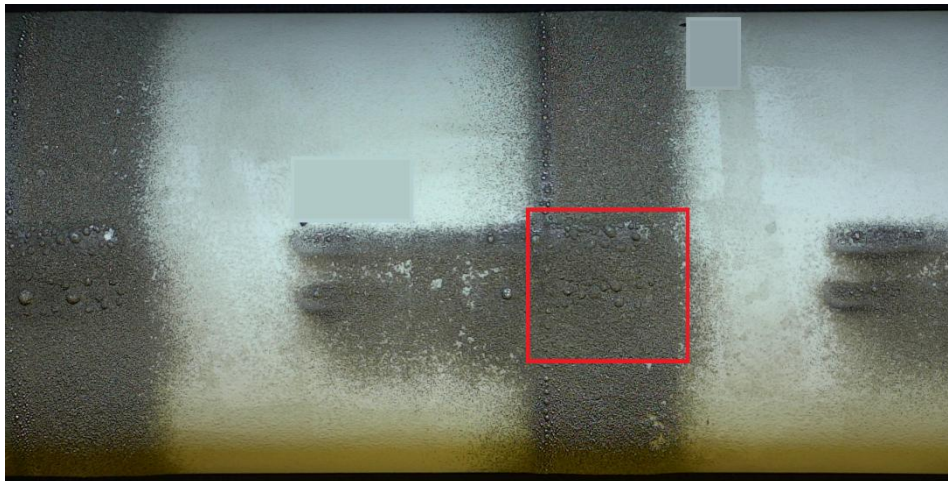


Figure 16: Laser clad thermocouple. The red square showing the thermocouple junction.

3.2 Evaluation of next generation of sensors

The electrical measurements, i.e. the strain and heat measurements, were made using a DEWESoft SIRIUS LV+ data acquisition (DAQ) system with the accompanied DEWESoft X2 software. For temperature measurements on thermocouples, an added thermocouple measurement module, the DEWETRON CPAD2-TH8 is connected to the SIRIUS over the CAN bus. See figure 17 for the DAQ system set-up.



Figure 17: Data acquisition system set-up.

For the resistance measurements, a simple quarter Wheatstone bridge configuration, together with four-terminal sensing was used. Thus, accurate resistance measurements, without influence from the leads and contacts, were possible. The SIRIUS system has a very high sensitivity and is therefore well suited for four-terminal sensing.

The contacting of the sensors was made by using temperature resistant, isolating and antistatic Kapton tape. This does not give a flawless connection, but it was assumed to suffice for testing purposes. To evaluate the connection made by Kapton tape, some tests were also made using an electrically conductive epoxy (EPO-TEK H20E), which should briefly withstand temperatures up to 300 degrees Celsius. In the future, sensor wires will be attached to sensor contact pads using micro laser welding.

3.2.1 Thick film strain gauges

For measurements on the strain gauges, it is the change in resistance as a function of e.g. strain or temperature that is wanted. Hence, it is the strain gauge's resistance that is to be measured.

3.2.1.1 Strain response

Strain response measurements were only conducted on the strain gages on the coupons; this was because no suitable way to induce strain on the tubes was found. The tubes were originally designed to be integrated in an industrial system for heated water vapor production, however, this could not be realized during this evaluation. For the strain response measurements on the coupons, one side of the coupon was clamped in a vice and weights (2.1 kg, 1.5 kg and 1.2 kg) were hung in a hole in the coupon on the opposite side, causing a mechanical load which resulted in an unknown but proportional strain. Figure 18 show the measurement set-up.



Figure 18: Strain (mechanical load) response measurement set-up for a strain gauge on a coupon. The red arrow points to a hook; on which the weighs were hanged.

This quite crude method gives a resistance to applied weight relationship (rather than a resistance to strain relationship), which however should be proportional to the resistance to strain relationship.

Strain response measurements were conducted both before and after the heat response measurements. This was done to investigate if the heating procedure of the strain gauge would cause a permanent change in the strain gauge's response to strain.

In addition to the coupon's strain gauges, the same tests were conducted on a few commercially printed strain gauges (with a similar Ni-based composition, Hastelloy) as a rough reference. See figure 19 for the test bars with strain gauges.

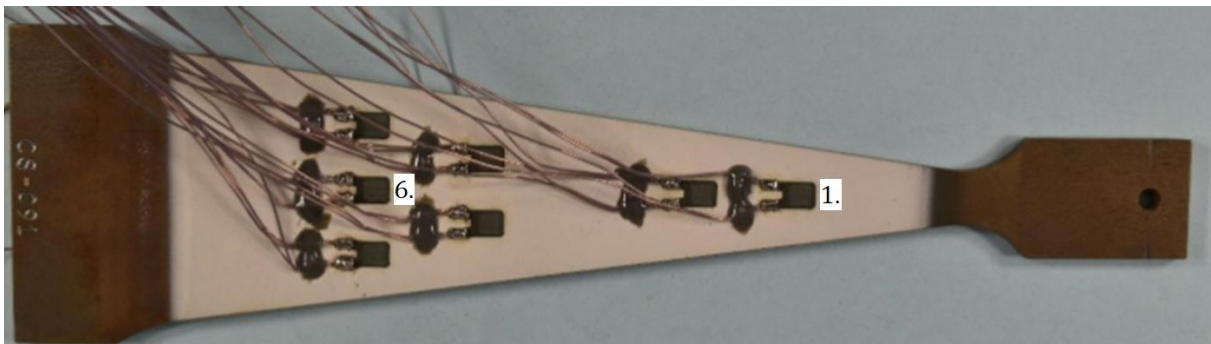


Figure 19: Test bar with commercially printed strain gauges. The sensor numbering goes from right to left, and from top to bottom.

3.2.1.2 Heat response

Heat response measurements were conducted on strain gauges on both the coupons and the tubes. For the heat response measurements, the junction of a reference K-type thermocouple (positive and negative legs twisted together), connected to the CAN bus, was fastened onto the coupon/tube with Kapton tape beside the strain gauge to be measured.

The sample (a coupon or a tube) was hung/rested on a stand, then heat was applied with a heating gun. See figure 20 for the measurement set-up.

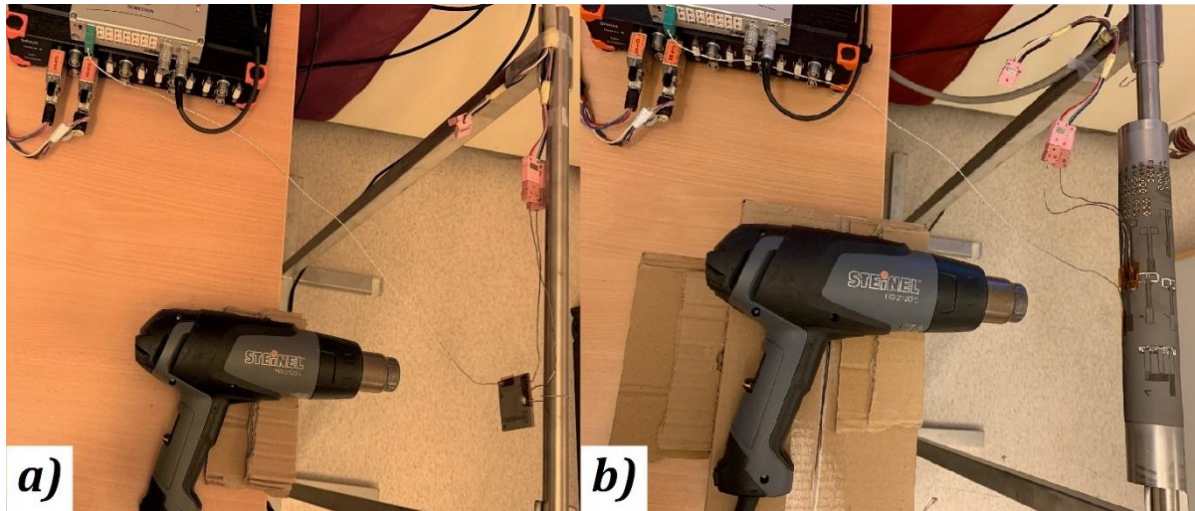


Figure 20: Heat response measurement set-up for a strain gauge on a) a coupon, b) a tube.

3.2.2 Laser clad thermocouples

For measurements on the laser clad thermocouples, it is the induced voltage by the thermocouple as a function of temperature that is desired. Hence, it is the potential difference between the two leads of the thermocouple that is to be measured.

For the heat response measurements on the laser clad thermocouples, the junction of a reference K-type thermocouple, connected to the CAN bus, was fastened onto the tube with Kapton tape beside the clad thermocouple junction of the thermocouple to be measured. Two different methods were used to connect the clad thermocouple to the CAN bus:

Since the clad, non-standard thermocouple is made out of two different nickel alloys (which could not be procured in wire form), and the K-type thermocouple wire has leads made out of Chromel (Ni90Cr10) and Alumel (Ni95Mn2Si2Al1), the clad thermocouple was contacted with K-type leads, which were seen as an potentially rough extension of the clad thermocouple. Then, in the measurement software, the clad thermocouple was defined as a K-type thermocouple (most similar type). The registered temperature from the clad “K-type” thermocouple was then compared to the registered temperature from the actual K-type thermocouple.

The other method was to use only Chromel leads for connecting the clad thermocouple. This method is eligible since, in theory, two leads of the same material and dimensions should produce equal voltage gradients as a result of the thermoelectric effect. Thus, if both Chromel leads experience the same temperature at the clad thermocouple, the leads should cancel each other out and not contribute to (distort) the measurements. Chromel leads was used because these have heat-resistant isolating covers, whilst e.g. the available copper leads had regular plastic covers, which could have melted during the measurements.

The tube was rested on a stand, in the same manner as for the strain gauge tubes in section 3.2.1.2, and heat was applied with a heating gun. See figure 21 for the measurement set-up.



Figure 21: Heat response measurement set-up for a thermocouple.

4 Results

4.1 Thick film strain gauges

4.1.1 Strain response

Since strain response measurements have been done on numerous samples of strain gauges on the coupons, complete strain response measurements are only displayed for one of the commercially printed reference strain gauges as an illustrative example in figure 22 (complete strain response measurements for all the evaluated strain gauges can be seen in Appendix 1). The strain response measurement results for all the evaluated strain gauges are summarized in tables 3 and 4, and figures 23 to 28. In tables 3 and 4, the strain response is expressed as a function of the amount of mechanical load applied. This function is a first-, second- or third-degree polynomial, chosen such that the coefficient of determination is at least 0.95.

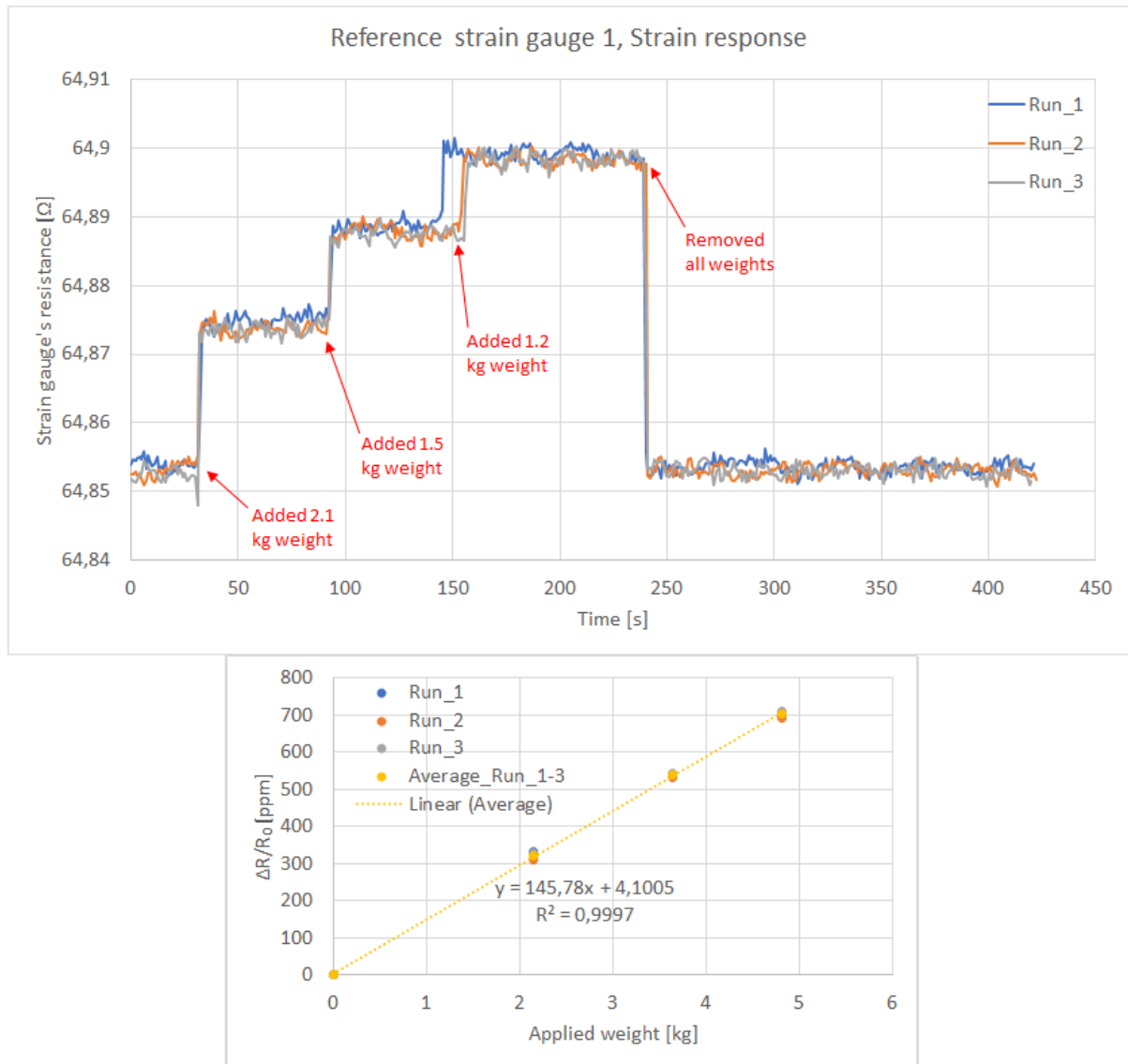


Figure 22: Strain response measurements on reference strain gauge 1. $\Delta R/R_0$ is the relative change of resistance in the strain gauge. Several identical runs were made for more accurate results.

| Strain gauge # | Focal position [mm] | Conductive path l/CSA [m/m ²] | $\Delta R/R_0 = P(\text{applied weight})$ [ppm] | Hysteresis ($\Delta R/R_0$) [ppm] |
|--------------------|---------------------|---|---|-------------------------------------|
| ref_1 | - | 21934758 | 146x | 3 |
| ref_5 | - | 21934758 | 150x | 7 |
| ref_6 | - | 21934758 | 151x | 68 |
| ref_7 | - | 21934758 | 155x | 40 |
| 20 | 0 | 20816777 | $11x^2 + 62x$ | 18 |
| 21 | 0 | 20816777 | $18x^2 + 27x$ | 28 |
| 22 | 0 | 20816777 | - | - |
| 24 | 0 | 20816777 | - | - |
| 26 | -1 | 20816777 | - | - |
| 31 | 0 | 15795645 | $9x^2 + 46x$ | 51 |
| 35 | -1 | 15795645 | $6x^2 + 36x$ | 18 |
| 36 | 1 | 15795645 | - | - |
| 38 | 1 | 15795645 | $20x^2 + 42x$ | 66 |
| 45 | 0 | 10816777 | $10x^2 + 54x$ | 21 |
| pico_3 | - | 38388406 | - | - |
| pico_5 | - | 38388406 | $20x^2 + 9x$ | 23 |
| pico_20-21 | - | 38388406 | $25x^2 + 24x$ | 101 |
| pico_24-25 | - | 38388406 | - | - |
| pico_24-25 (Glued) | - | 38388406 | - | - |

Table 3: Strain response measurement results (before heating measurements). The focal position is the height above/below the substrate surface. CSA stands for cross sectional area and l stands for length.

| Strain gauge # | Focal position [mm] | Conductive path l/CSA [m/m ²] | $\Delta R/R_0 = P(\text{applied weight})$ [ppm] | Hysteresis ($\Delta R/R_0$) [ppm] |
|----------------|---------------------|---|---|-------------------------------------|
| 20 | 0 | 20816777 | $10x^2 + 88x$ | 58 |
| 21 | 0 | 20816777 | $13x^2 + 14x$ | 33 |
| 31 | 0 | 15795645 | $7x^2 + 37x$ | 22 |
| 35 | -1 | 15795645 | $6x^3 - 27x^2 + 44x$ | 36 |
| 38 | 1 | 15795645 | $1x^3 + 25x^2 - 21x$ | 21 |
| 45 | 0 | 10816777 | $18x^2 + 10x$ | 49 |
| pico_5 | - | 38388406 | $18x^3 - 63x^2 + 95x$ | 159 |
| pico_5 (Glued) | - | 38388406 | $13x^3 - 76x^2 + 162x$ | 55 |

Table 4: Strain response measurement results (after heating measurements). The focal position is the height above the substrate surface. CSA stands for cross sectional area and l stands for length.

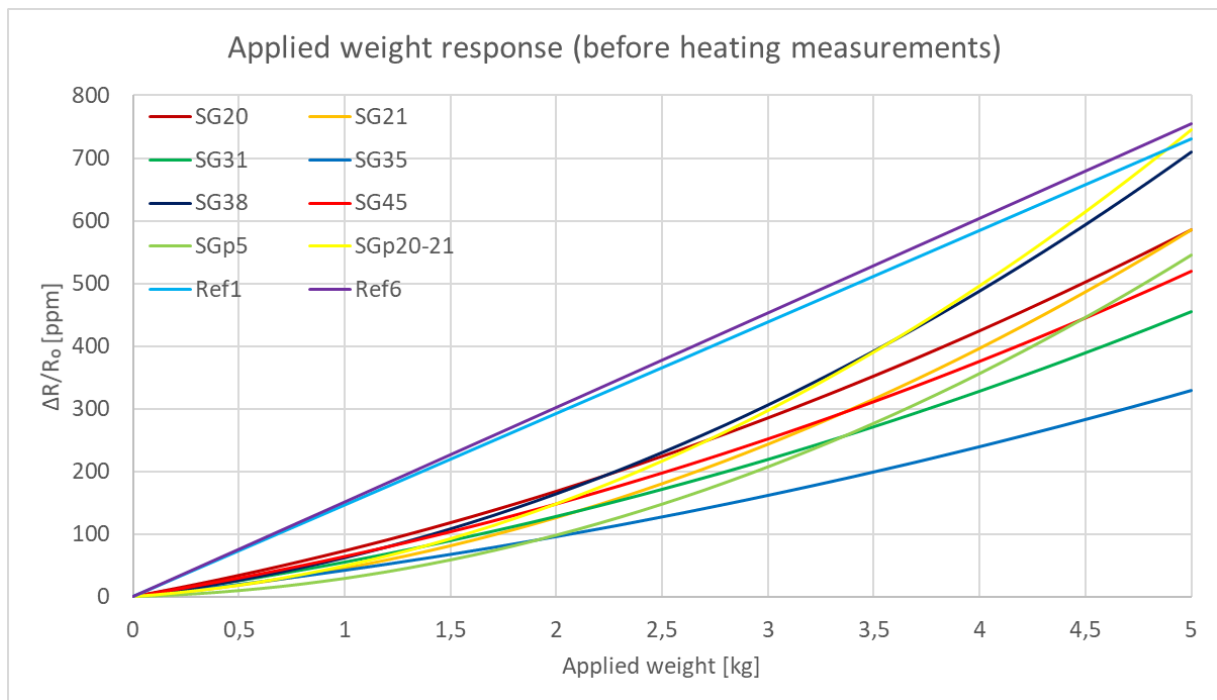


Figure 23: Comparison between the polynomial functions in table 3.

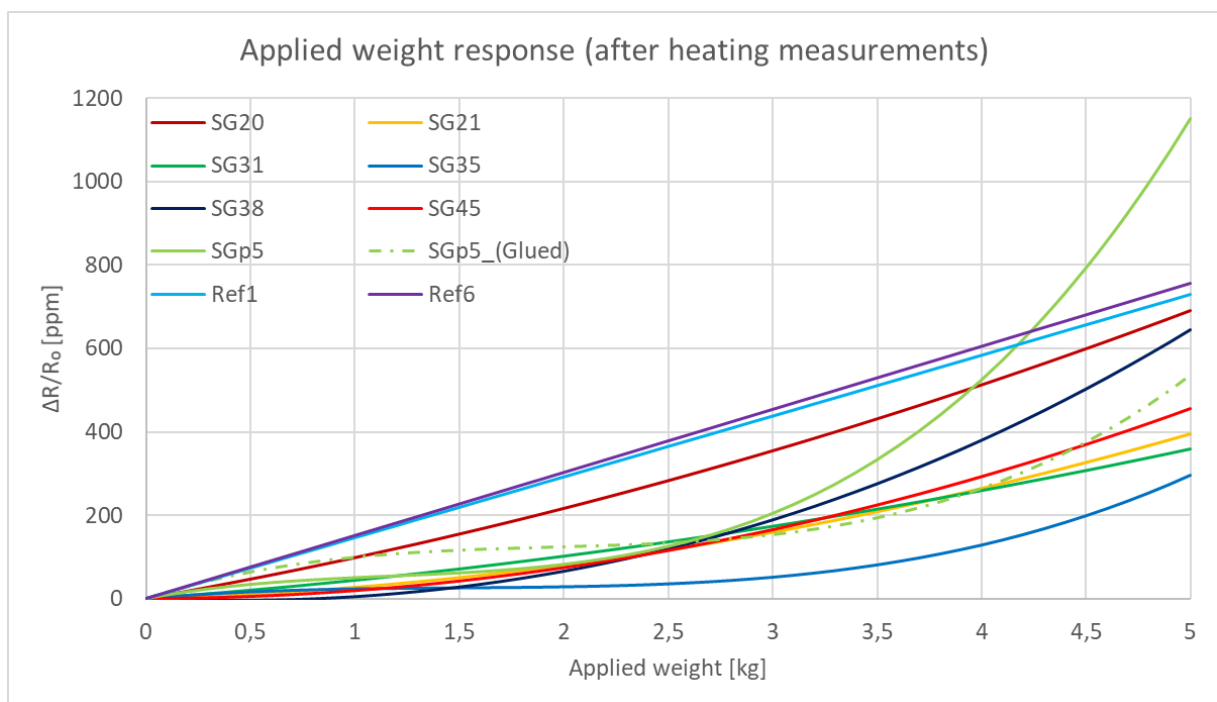


Figure 24: Comparison between the polynomial functions in table 4.

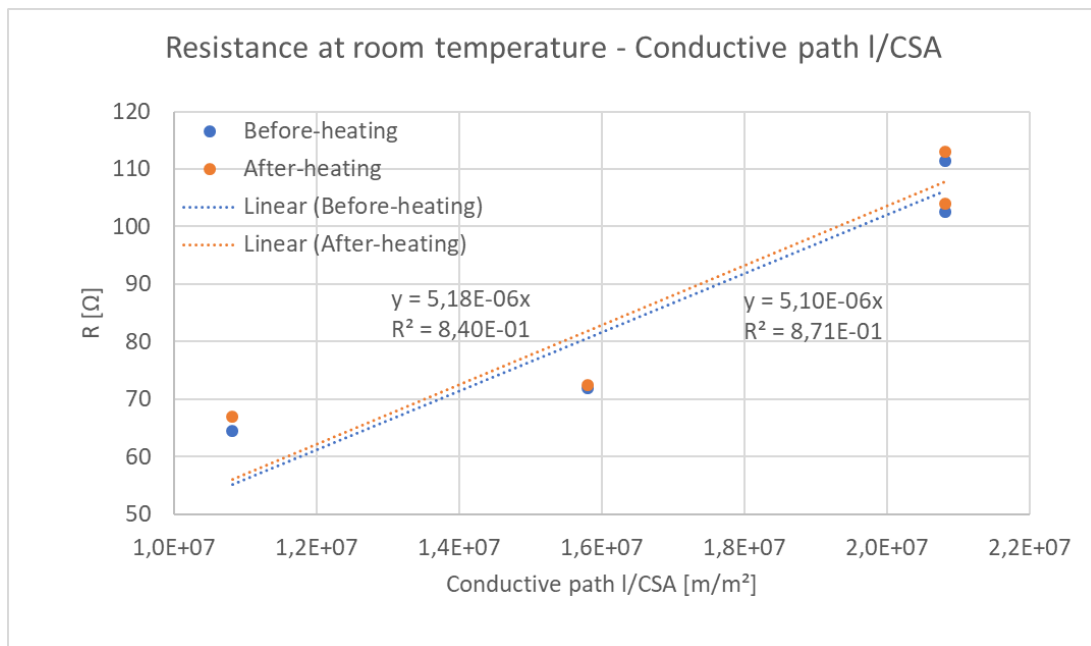


Figure 25: Dependence of the conductive path l/CSA , on the nanosecond ablated strain gauge's resistance at room temperature.

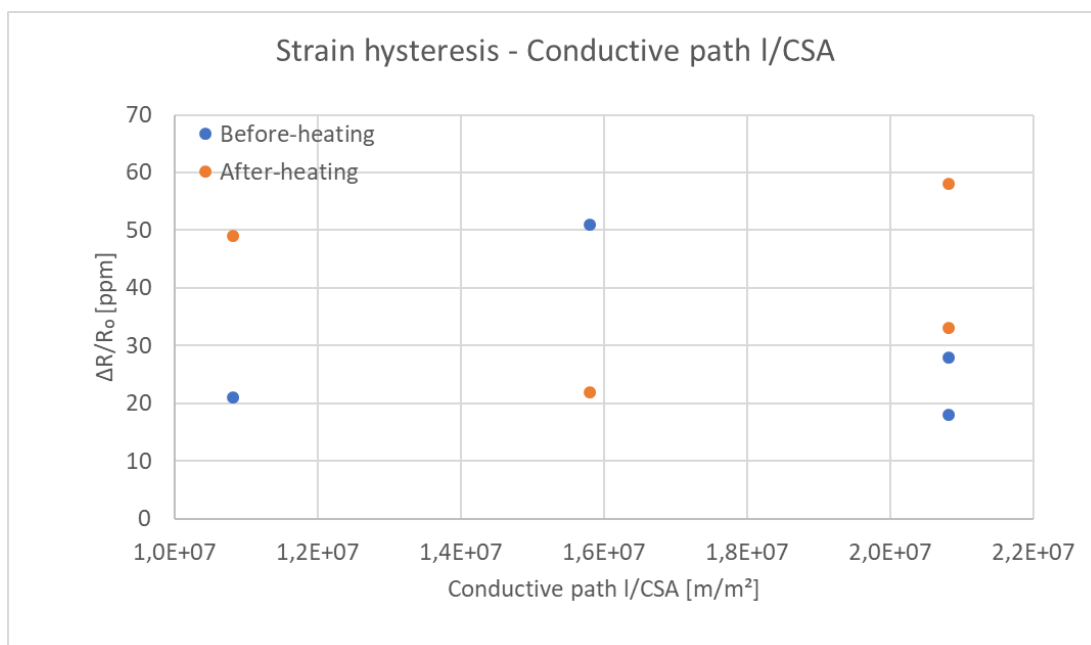


Figure 26: Dependence of the conductive path l/CSA , on the hysteresis on the nanosecond ablated strain gauges.

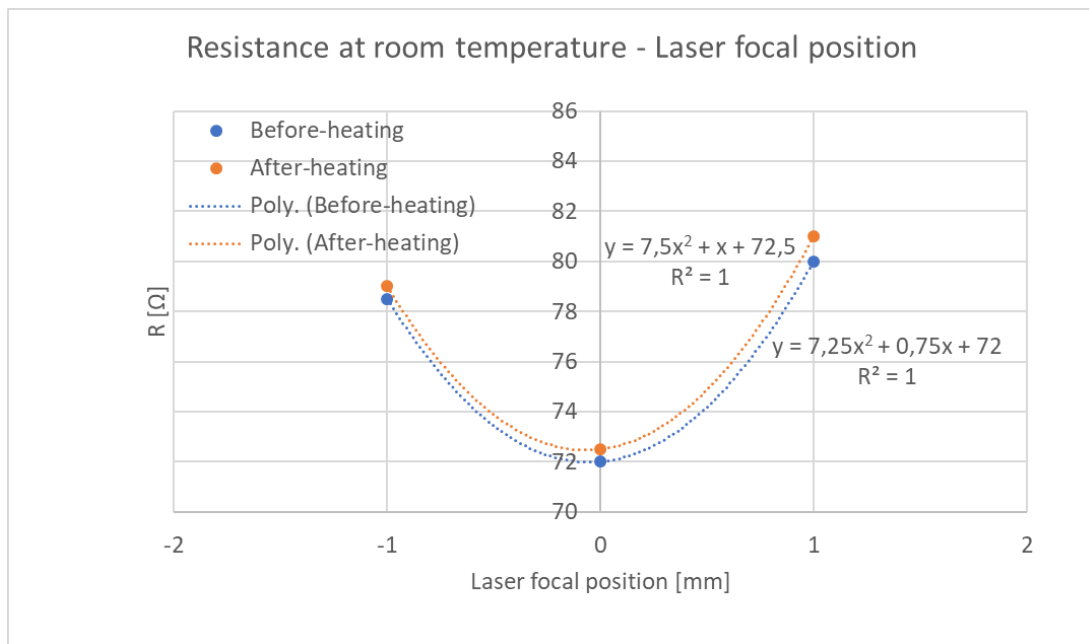


Figure 27: Dependence of the laser focal position on the strain gauge's resistance at room temperature on the nanosecond ablated strain gauges.

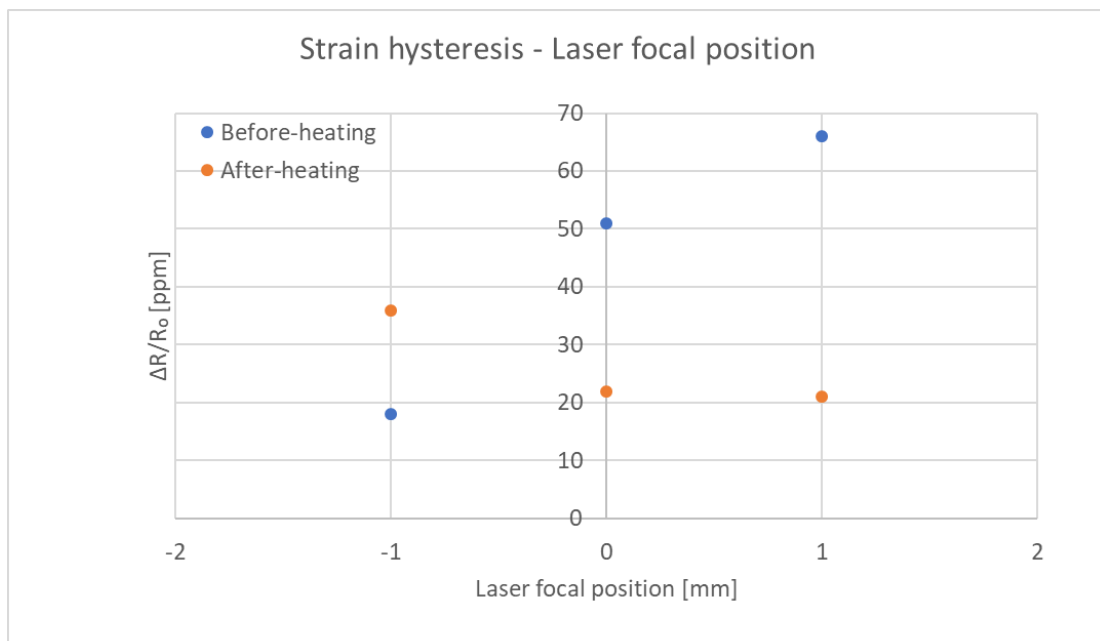


Figure 28: Dependence of the laser focal position on the hysteresis on the nanosecond ablated strain gauges.

4.1.2 Heat response

Since heat response measurements have been done on numerous samples of strain gauges, both on coupons and tubes, complete heat response measurements are only displayed for one strain gauge (coupon strain gauge 21) as an illustrative example in figure 29 (complete heat response measurements for all the evaluated strain gauges can be seen in Appendix 2). The heat response measurement results for all the evaluated strain gauges are summarized in tables 5 to 7, and figures 30 to 40.

4.1.2.1 Coupons

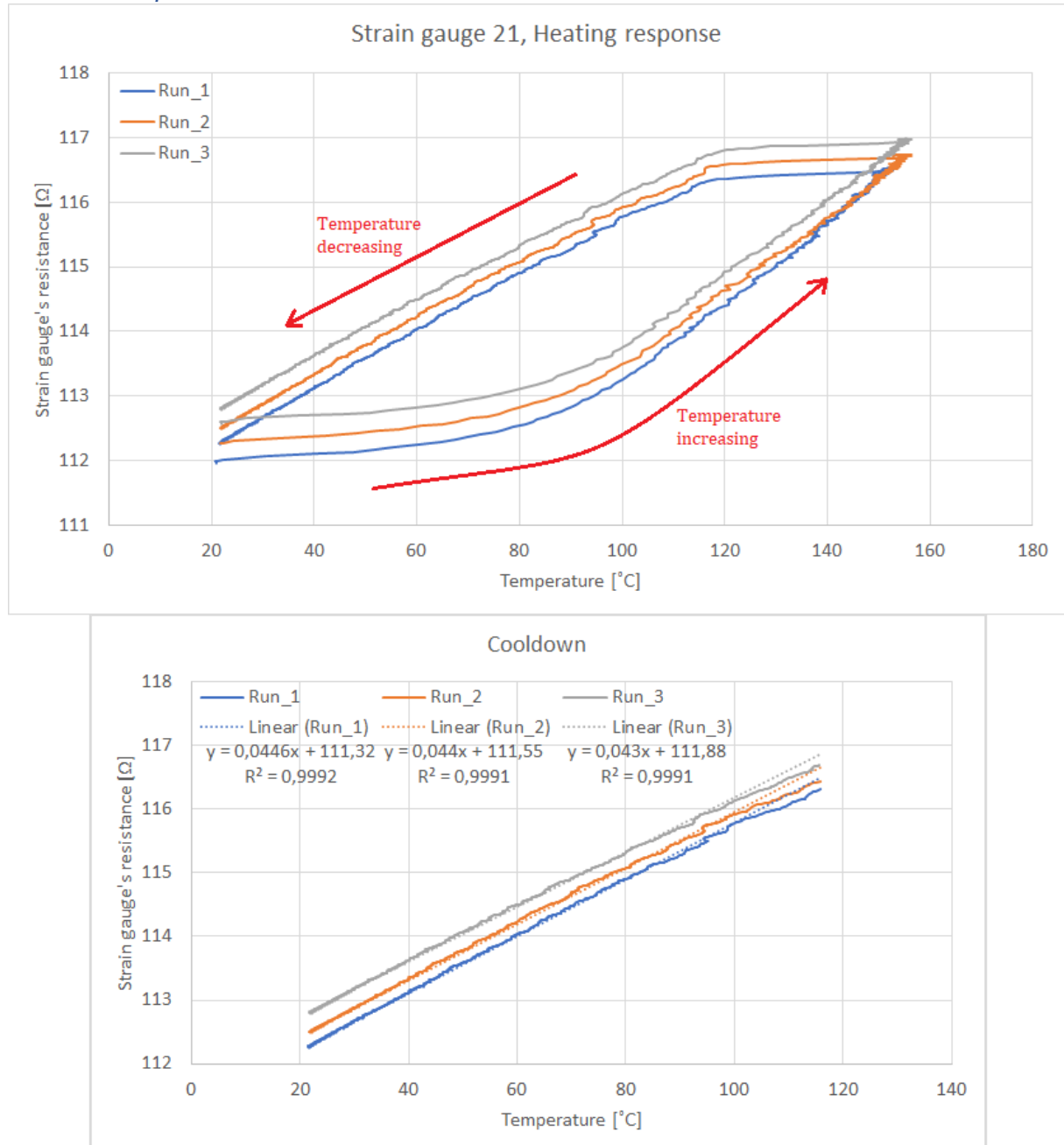


Figure 29: Heat response measurements on coupon strain gauge 21. Several identical runs were made for more accurate results.

| Strain gauge # | Focal position [mm] | Conductive path I/CSA [m/m ²] | Heat response $\Delta R/R_0$ [ppm/°C] | Thermal drift ($\Delta R/R_0$) [ppm] |
|----------------|---------------------|---|---------------------------------------|--|
| 20 | 0 | 20816777 | 472 | 1737 |
| 21 | 0 | 20816777 | 389 | 2350 |
| 31 | 0 | 15795645 | 447 | 1653 |
| 35 | -1 | 15795645 | 429 | 3236 |
| 38 | 1 | 15795645 | 422 | 5263 |
| 45 | 0 | 10816777 | 456 | 5829 |
| pico_5 | - | 38388406 | 440 | 3355 |
| pico_5 (Glued) | - | 38388406 | - | - |

Table 5: Heat response measurement results for coupon strain gauges. The focal position is the height above the substrate surface. CSA stands for cross sectional area and I stands for length.

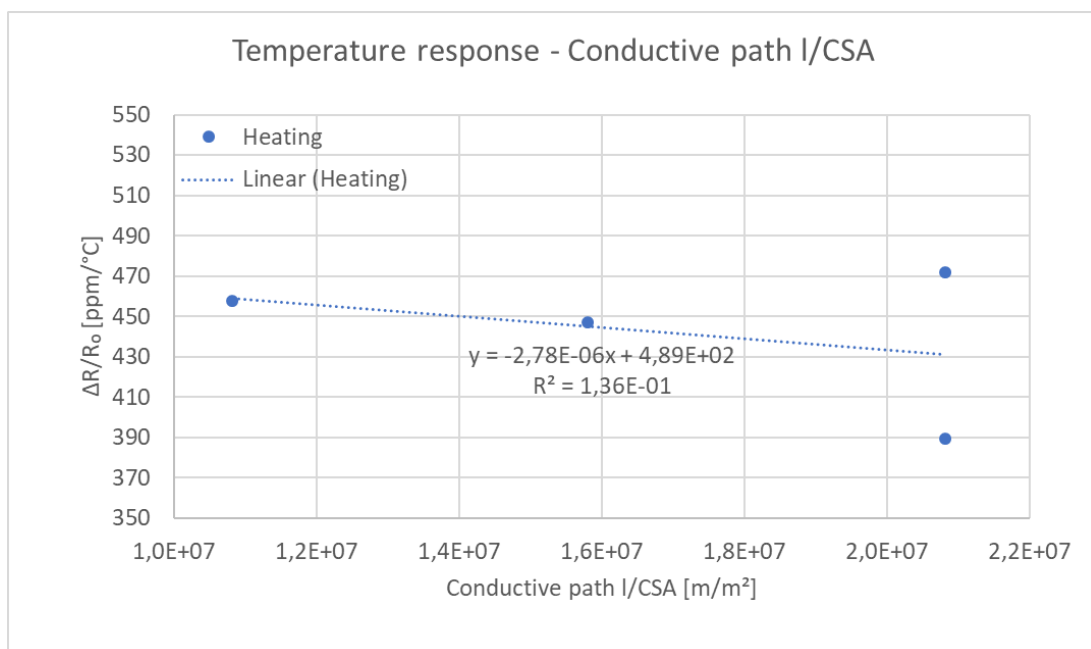


Figure 30: Dependence of the conductive path I/CSA, on the temperature response for the nanosecond ablated strain gauges on the coupons.

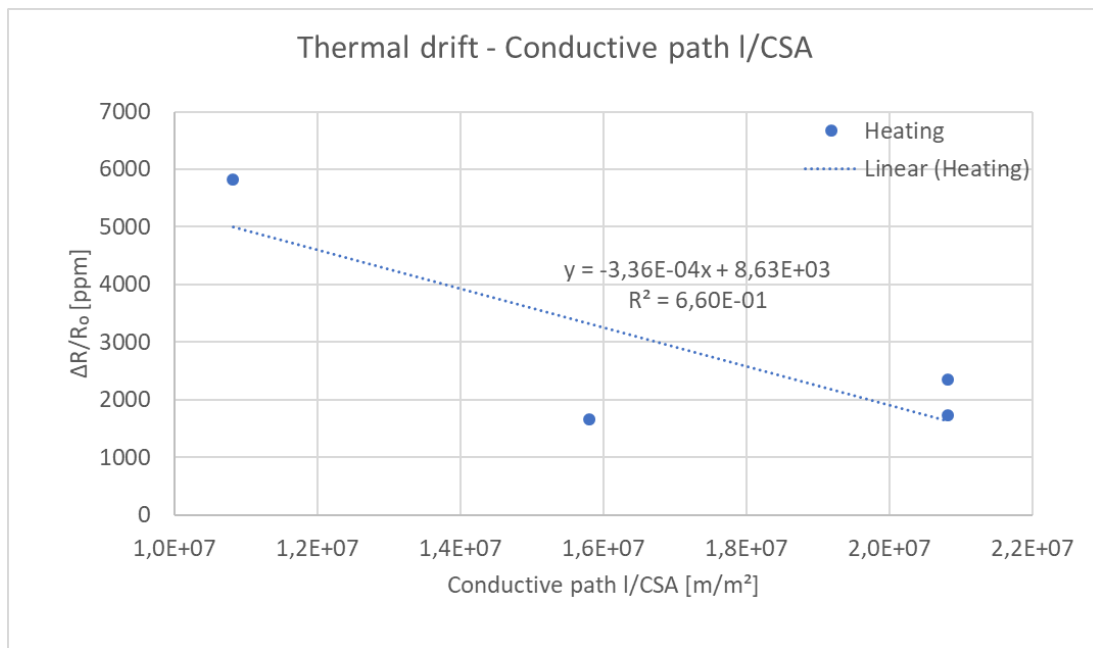


Figure 31: Dependence of the conductive path I/CSA, on the thermal drift for the nanosecond ablated strain gauges on the coupons.

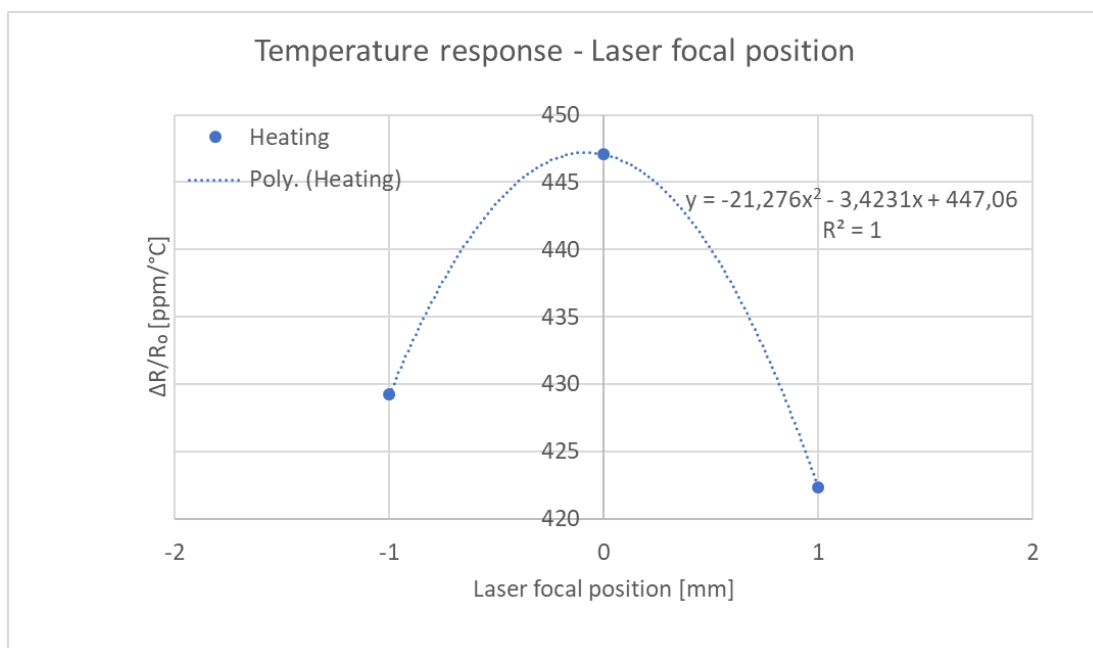


Figure 32: Dependence of the laser focal position on the temperature response for the nanosecond ablated strain gauges on the coupons.

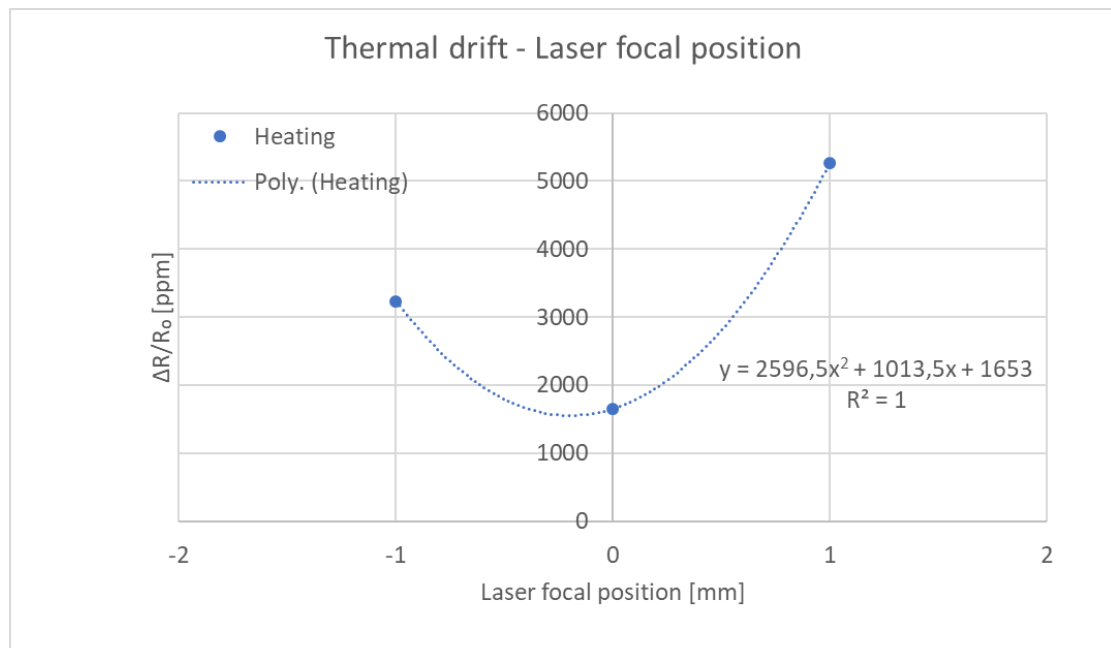


Figure 33: Dependence of the laser focal position on the thermal drift for the nanosecond ablated strain gauges on the coupons.

4.1.2.2 Tubes

| Strain gauge # | Focal position [mm] | Conductive path I/CSA [m/m²] | Heat response $\Delta R/R_0$ [ppm/°C] | Thermal drift ($\Delta R/R_0$) [ppm] |
|----------------|---------------------|------------------------------|---------------------------------------|--|
| Tube #1 - 1 | 0 | 8886054 | 429 | 6746 |
| Tube #1 - 2 | 0 | 14752381 | 396 | 5859 |
| Tube #1 - 3 | 0 | 16288118 | 327 | 4912 |
| Tube #1 - 4 | 0 | 17743414 | - | - |
| Tube #1 - 6 | 0 | 19935650 | 330 | 4688 |
| Tube #1 - 8 | 0 | 17743414 | 402 | 10718 |

Table 6: Heat response measurement results for coarse grained tube strain gauges. The focal position is the height above the substrate surface. CSA stands for cross sectional area and I stands for length.

| Strain gauge # | Focal position [mm] | Conductive path I/CSA [m/m²] | Heat response $\Delta R/R_0$ [ppm/°C] | Thermal drift ($\Delta R/R_0$) [ppm] |
|----------------|---------------------|------------------------------|---------------------------------------|--|
| Tube #2 - 13 | 0 | 10887491 | 1706 | 4313 |
| Tube #2 - 15* | 0 | 10887491 | 1758 | 5355 |
| Tube #2 - 16 | 0 | 12483974 | 1681 | 2222 |
| Tube #2 - 17 | 0 | 14112319 | 1767 | 5897 |
| Tube #2 - 27 | -1 | 9798177 | 1917 | 3448 |
| Tube #2 - 32 | -1 | 6493232 | 1721 | 3684 |

Table 7: Heat response measurement results for fine grained tube strain gauges. The focal position is the height above the substrate surface. CSA stands for cross sectional area and I stands for length.

*For the strain gauge denoted by *Tube #2 – 15*; argon gas with flow rate of 17 l/min was used as protective gas in the laser ablation process.

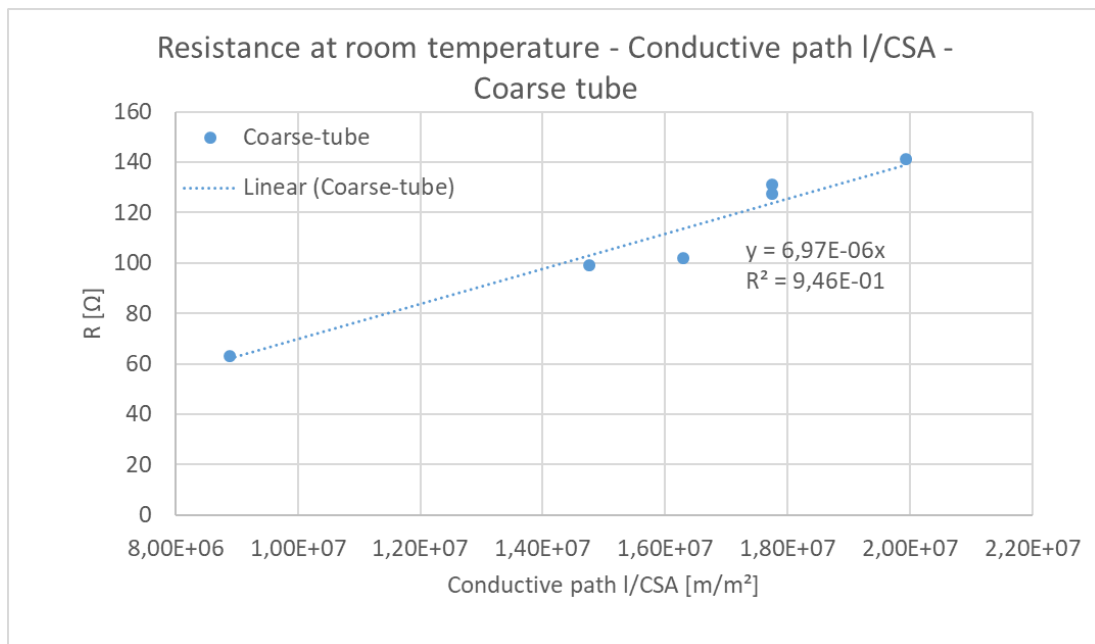


Figure 34: Dependence of the conductive path I/CSA, on the coarse grained tube strain gauge's resistance at room temperature.

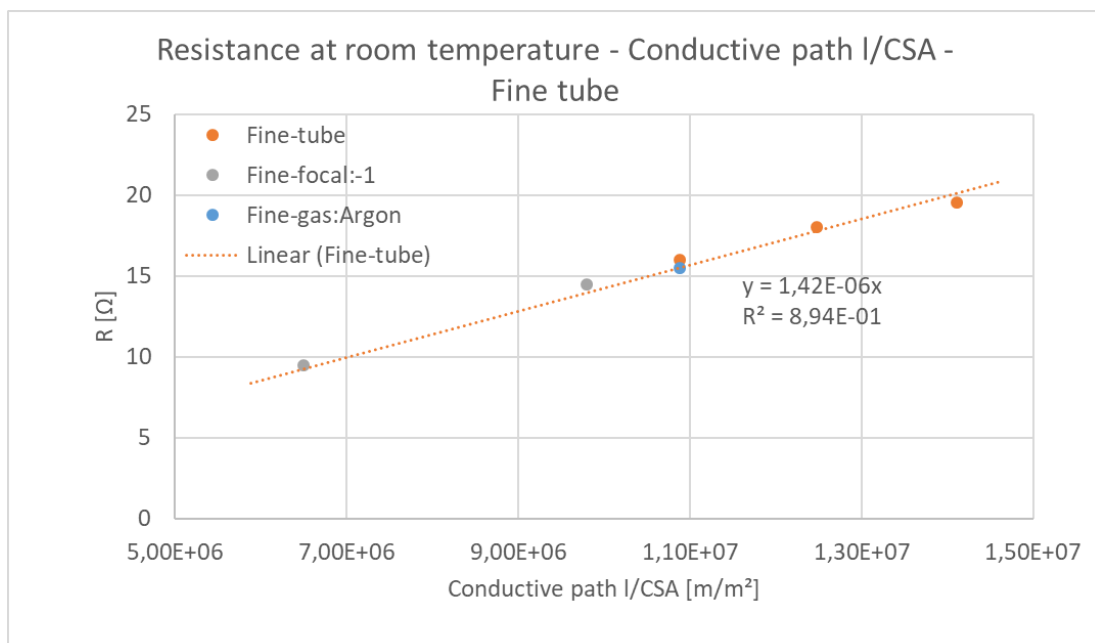


Figure 35: Dependence of the conductive path I/CSA, on the fine grained tube strain gauge's resistance at room temperature.

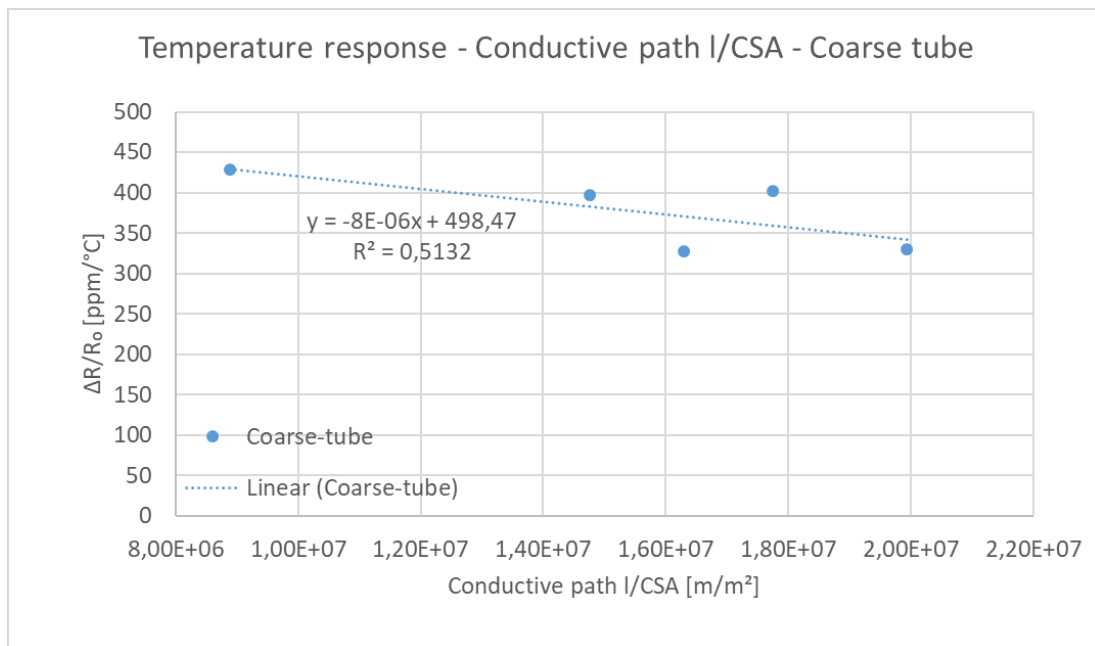


Figure 36: Dependence of the conductive path I/CSA, on the temperature response for the strain gauges on the coarse grained tubes.

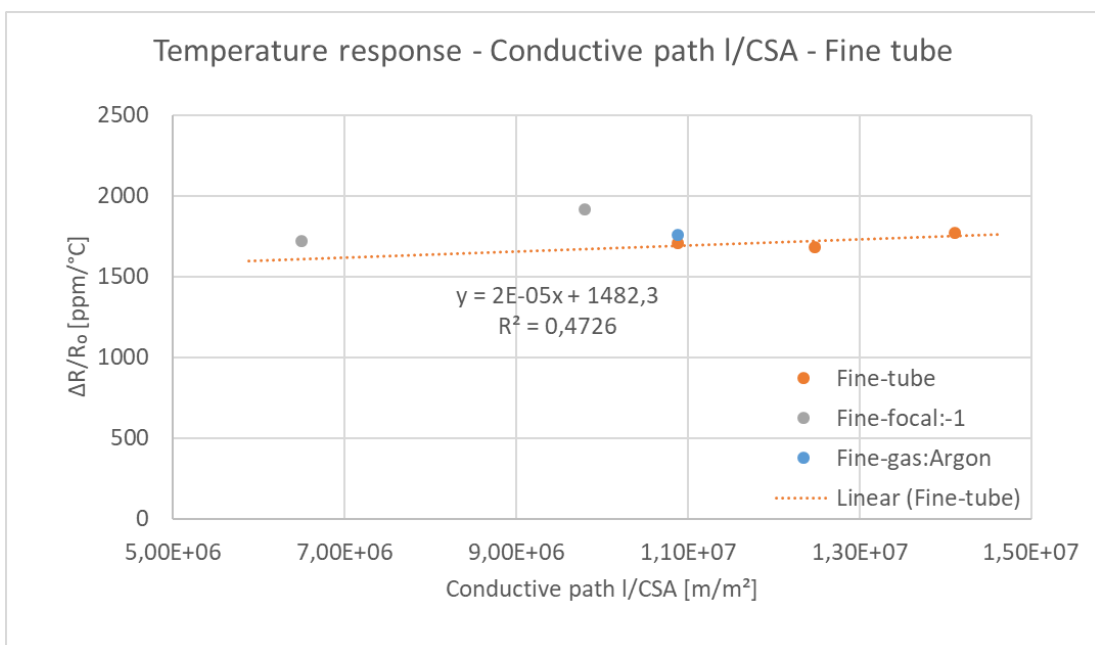


Figure 37: Dependence of the conductive path I/CSA, on the temperature response for the strain gauges on the fine grained tubes.

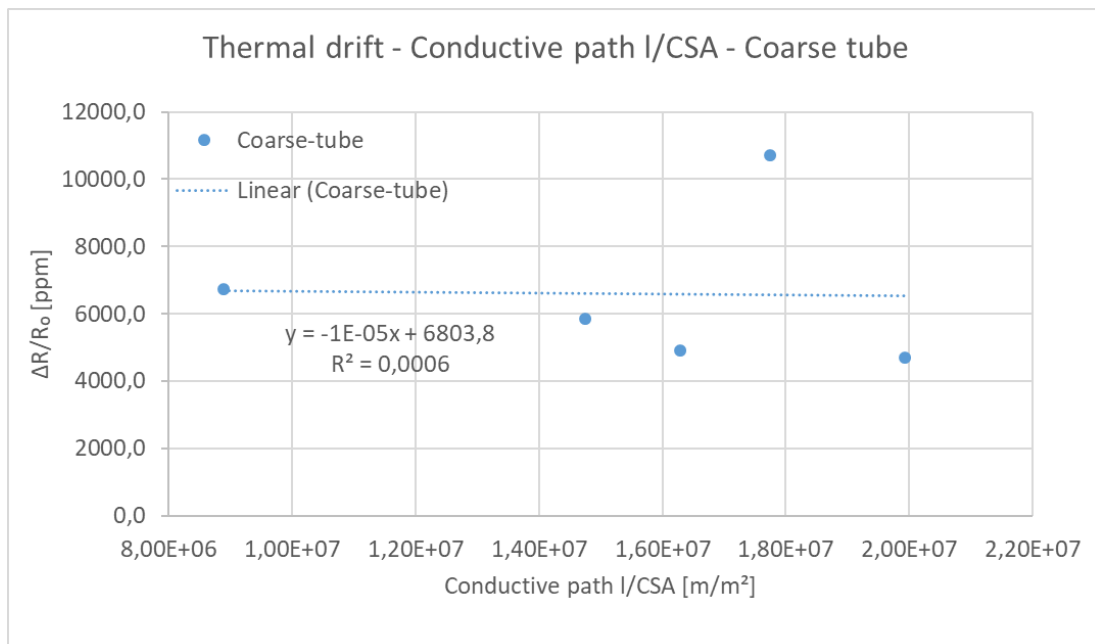


Figure 38: Dependence of the conductive path l/CSA, on the thermal drift for the strain gauges on the coarse grained tube.

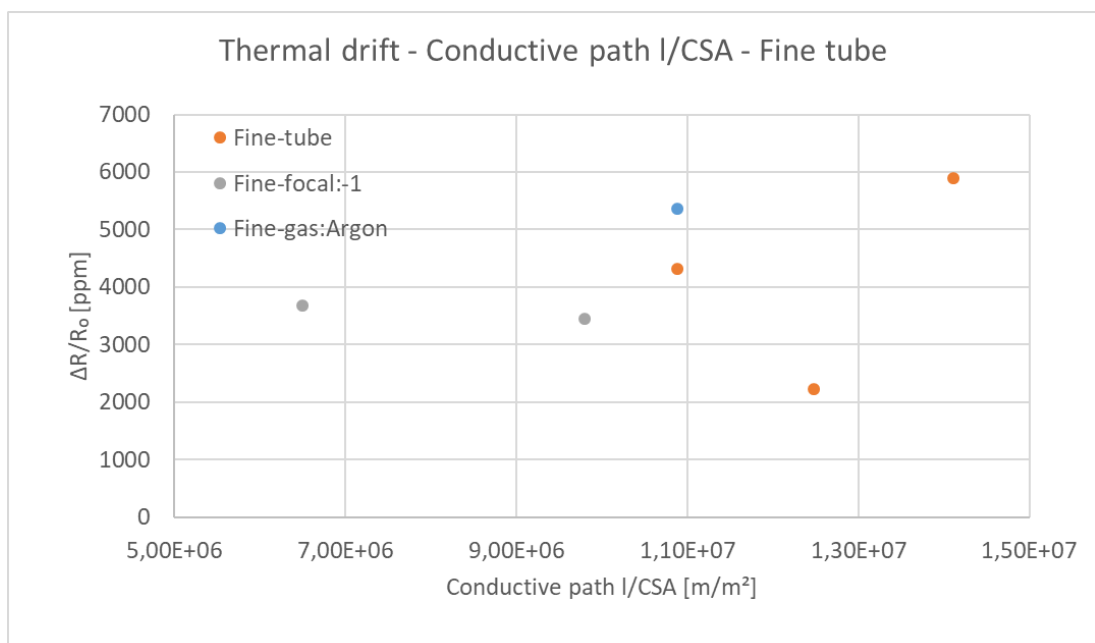


Figure 39: Dependence of the conductive path l/CSA, on the thermal drift for the strain gauges on the fine grained tube.



Figure 40: Heat response measurements on the strain gauge on the carbon steel tube.

4.2 Laser cladded thermocouples

The first measurements that were made was a comparison between the registered temperature of a reference K-type thermocouple and one of the cladded thermocouples (defined in the software as a K-type thermocouple), connected with Chromel and Alumel leads. This comparison can be seen in figure 41. Next, the same comparison was made when the cladded thermocouple was connected with only Chromel leads. This comparison can be seen in figure 42. To verify the theory that says that the Chromel leads should cancel each other out, a third comparison was made. This comparison, which can be seen in figure 43, was between the reference K-type thermocouple and the Chromel leads entwined at one end forming a junction.

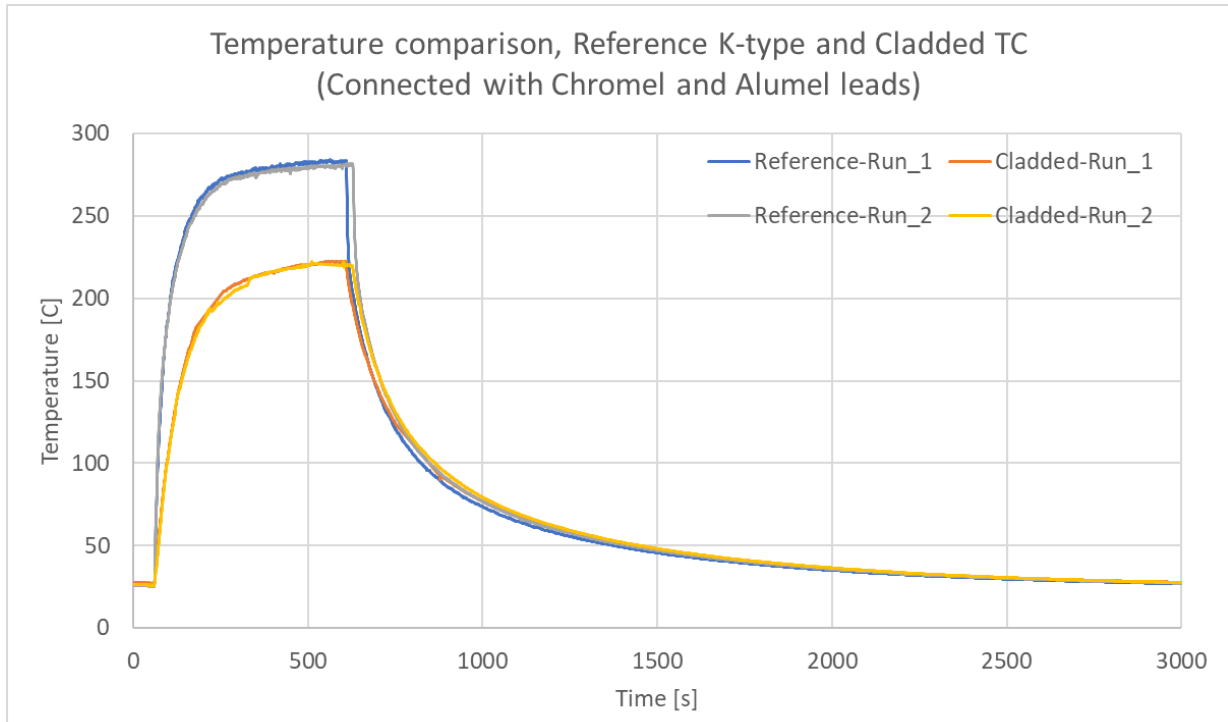


Figure 41: Comparison of the registered temperature of a K-type thermocouple and a cladded thermocouple, set as K-type in the measuring software, connected with Chromel and Alumel leads.

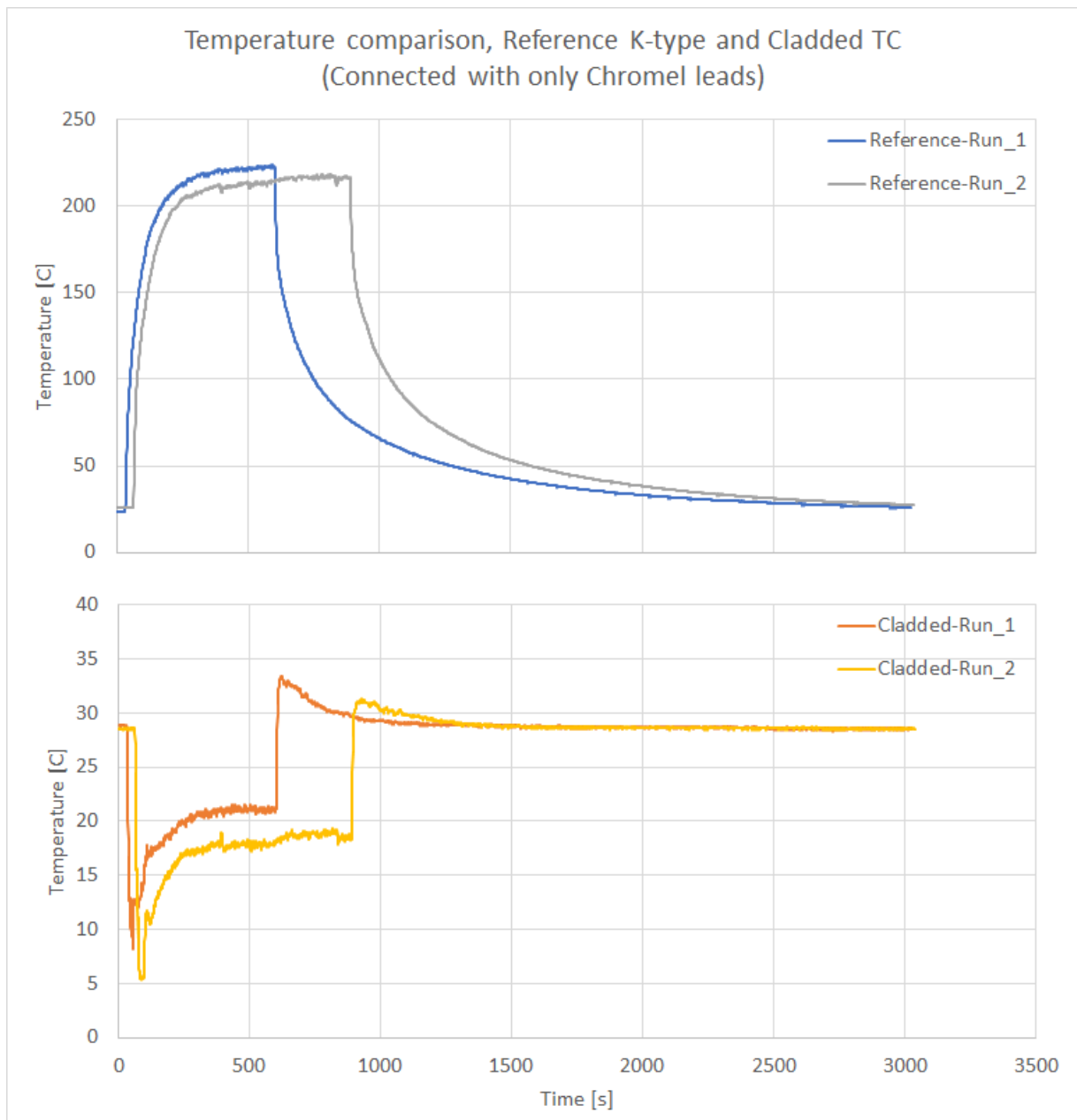


Figure 42: Comparison of the registered temperature of a K-type thermocouple and a cladded thermocouple, set as K-type in the measuring software, connected with only Chromel leads.

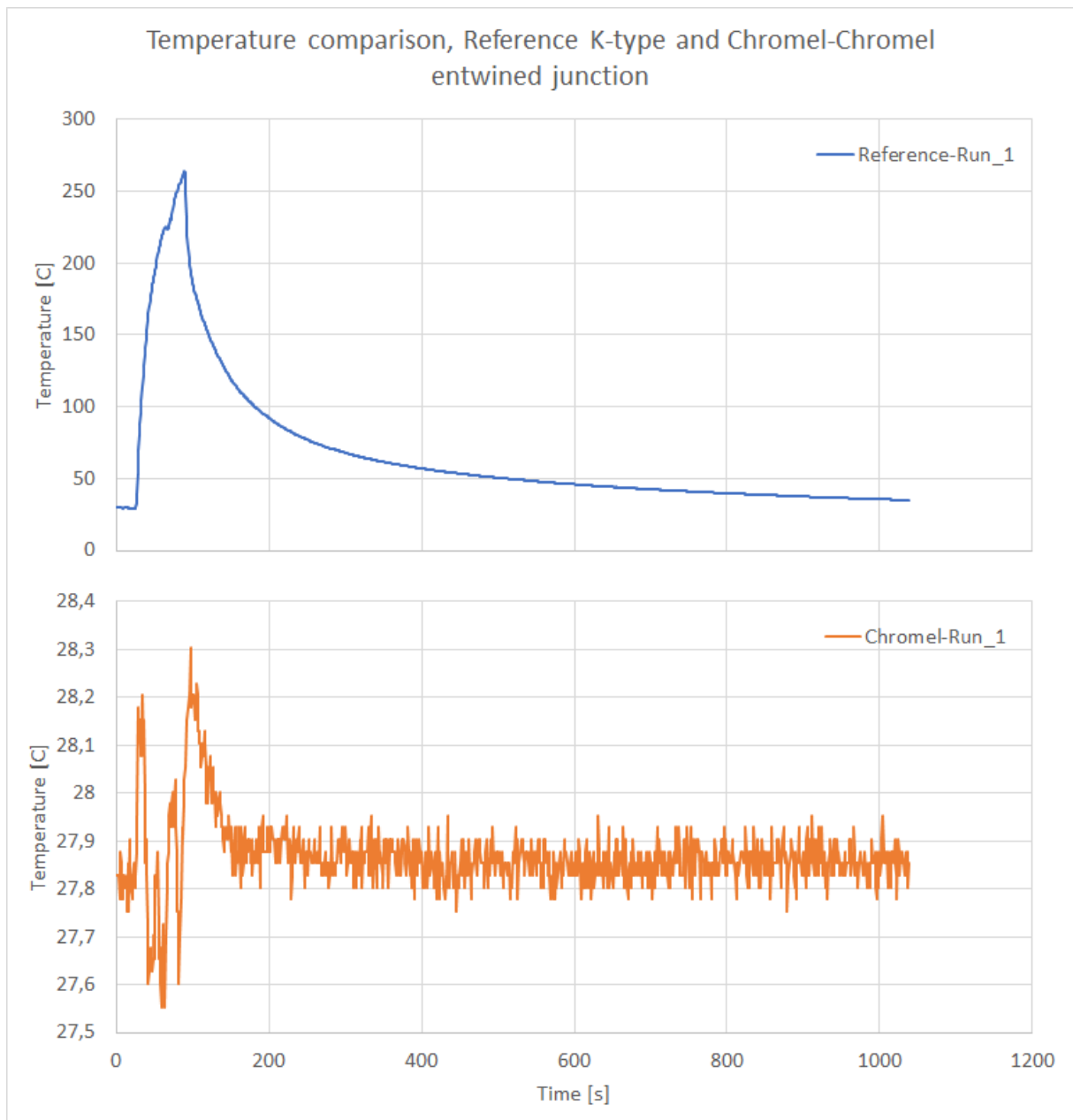


Figure 43: Comparison of the registered temperature of a K-type thermocouple and two Chromel leads entwined at one end, set as K-type in the measuring software.

5 Discussion

5.1 Thick film strain gauges

5.1.1 Strain response

In figure 25, the strain gauge's resistance as a function of the conductive path l/CSA can be seen. From equation 1 in section 2.1, it can be said that the slope of the linear approximation, roughly $5 \cdot 10^{-6} \Omega m$, is the resistivity of the conductive paths for strain gauges on the coupons.

In figure 27, the resistance as a function of the laser focal position can be seen. The resistance seems to increase when the laser focal position is not on the surface, i.e. when the focal position is either below or above the surface. The increase of resistance for focal position 1 mm above the surface is approximately the same as for 1 mm below the surface, approximately 10%. This may be reasonable since the laser spot area on the surface should become bigger when the laser is not focused onto the surface, whether the focal position is above or below the surface as the focusing lens gives the laser an hourglass-shaped appearance. Thus, the laser spot area should be the same both 1 mm above and 1 mm below the focal point. A larger laser spot area should remove slightly more material, resulting in slightly narrower conductive paths, which should result in a higher resistance.

In figures 23 and 24, the strain response before and after the heating measurements can be seen. It can be seen that the commercial reference strain gauges have an almost perfect linear strain response, which is desired with respect to the theory in section 2.5.1. The thick film strain gauges have a less linear strain response, which indicates that there are other influences on the resistance change than just the strain. Perhaps e.g. microstructural changes in the measurement grid and a result of potential micro-cracks caused by the laser ablation. However, the samples with the most linear behavior were 20, 31, 35 and 45 before the heating measurements (in figure 23), and samples 20 and 31 after the heating measurements (in figure 24). Overall, the strain gauges 20 and 31 are thus the most linear and stable samples. However, there is no clear explanation for this. For instance, sample 20 and 21 should be identical in the means of production. However, sample 20 have a much more linear response but is also less sensitive (which possibly could be explained by smaller influence from e.g. microstructural changes and micro-cracks). It appears as the most significant production parameter, with respect to the strain response, in this evaluation could be random differences in the APS process (e.g. coating thickness and/or microstructural differences) and/or the laser ablation process (e.g. random damages to the remaining material such as micro-cracks).

In tables 3 and 4, the strain hysteresis before and after the heating measurements can be seen. We can see that the hysteresis for the thick film strain gauges was (42 ± 24) ppm (with the addition of an outlier on 101 ppm) before the heating measurements, and between (39.5 ± 18.5) ppm (with the addition of an outlier on 159 ppm) after the heating measurements. This can be compared with the commercial reference sample that had a hysteresis between (35.5 ± 32.5) ppm. This shows that the thick film strain gauges have slightly larger, but comparable, hysteresis as to the reference strain gauges. It should be mentioned that the reference samples (unlike the thick film samples) have been prestressed (deflected in both tension and compression for 1002 cycles and heat treated prior to measurements), which possibly could have increased these samples' stability.

The strain hysteresis got larger after the heating measurements for all samples except for samples 31 and 38. However, since the compared change in hysteresis is an average of a few individual measurements, and since the variation in hysteresis is larger between individual measurements than the average hysteresis between before and after the heating measurements, and since two out of six samples actually got a smaller average hysteresis after the heating measurements, no clear correlation can be seen.

In table 3, it can also be seen that there is no clear difference in hysteresis between nanosecond ablated and picosecond ablated strain gauges. For nanosecond ablated samples, the hysteresis was (42 ± 24) ppm, whilst for the only two available (fully functioning) picosecond ablated samples, the hysteresis was 23 ppm and 101 ppm. Yet, the hysteresis of 101 ppm is notably larger than for the other samples. However, as one of the two picosecond ablated samples has a hysteresis as low as 23 ppm, no correlation between laser pulse duration and strain hysteresis is made.

In figures 26 and 28, it can also be seen that the hysteresis does not seem to be affected by the conductive path I/CSA , nor by the laser focal position.

In table 4, it can be seen that the hysteresis on sample pico_5 decreased from 159 ppm to 55 ppm when glue was used instead of tape for connecting the strain gauge. Therefore, it seems that glued contacts are a better choice than taped contacts. However, in table 3, no improvement of the strain performance of strain gauge pico_24-25 when using glued contacts was seen. Furthermore, the glued contacts did not perform well at all during the heating measurements. Thus, for better heating performance and for less effort and mess, taped contacts were the better option in these evaluation measurements.

5.1.2 Heat response

5.1.2.1 Coupons

In figure 29, it can be seen that there is a major difference in the correlation between the strain gauge's resistance and the temperature during the increase of the temperature compared to the decrease of the temperature. This is probably because of that during the heating process, the reference thermocouple junction is surrounded by the heated tube on one side and by the considerably warmer air from the heat gun on the other side, whilst the tube is surrounded by the hot air on one side and by the colder ambient air on the other side. This, understandably, causes the thermocouple to have (and register) a higher temperature than what the tube has. Hence, the most correct correlation between the strain gauge's resistance and the temperature is obtained during the cooldown, when the temperature of the thermocouple junction and the tube reasonably should be much more comparable.

In table 5, the heat response for the tested strain gauges can be seen. The heat response was in the interval (430.5 ± 41.5) ppm/°C. The samples with the smallest heat response were 21, 35 and 38, whilst sample 20, 31 and 45 had the largest heat response. Here, it seems to be a correlation between a larger heat response and a more linear strain response.

In figure 30, a small declining temperature response for increasing conductive path I/CSA can be seen. However, since this is a very small decline, and based on only four samples, no clear correlation between the heat response and the conductive path I/CSA can be concluded.

In figure 32, it can be seen that the heat response is clearly affected by the laser focal position. For a defocused laser, the heat response gets lower than for the sample with the laser focal position on the surface. The decrease in heat response for a 1 mm defocus was approximately 5%.

In table 5, the thermal drift for the tested strain gauges can be seen. The thermal drift was in the interval (3741 ± 2088) ppm, thus, it is much more varying than the heat response.

In figure 31, the thermal drift seems to decrease with increasing conductive path I/CSA . However, if the data point with noticeably large thermal drift would be disregarded, the correlation would instead be the opposite, i.e. increasing thermal drift with increasing

conductive path l/CSA . Thus, when considering that the correlation is based on only four samples, and that one outlier could distort the correlation quite much, not much can be said at this point.

In figure 33 on the other hand, it is clear that the thermal drift seems to depend on the laser focal position. For the samples made with a defocused laser, the thermal drift is higher than for the sample with the laser focal position on the surface. Furthermore, in contrast to earlier correlations regarding the focal position, in this case, the thermal drift also seems to depend on whether the focal position is 1 mm above or 1 mm below the surface. The increase in thermal drift is approximately 220% for 1 mm above the surface and approximately 100% for 1 mm below the surface. Whether the difference in increased thermal drift is caused by the positive or negative defocusing, or by other uncontrolled factors, cannot be said with certainty. However, it is quite clear that the thermal drift gets higher for a defocused laser.

5.1.2.2 Tubes

In figure 34, the resistance of strain gauges on the coarse grained tube as a function of the conductive path l/CSA can be seen. The slope of the linear approximation, roughly $7 \cdot 10^{-6} \Omega m$, is the resistivity of the conductive paths for strain gauges on the coarse grained tubes. In figure 35, the same can be seen for the fine grained tube. The slope of the linear approximation, roughly $1.5 \cdot 10^{-6} \Omega m$, is the resistivity of the conductive paths for strain gauges on the fine grained tubes.

In figure 35, it can also be seen that the resistance of a strain gauge that was ablated when using argon (17 l/min) as protective gas, is nearly the same as for an identical strain gauge that was ablated without protective gas. Thus, the protective gas seems to have no large impact on the produced strain gauge's resistance.

Another thing to notice in figure 35 is that two of the data points belong to strain gauges that were made with a laser focal position 1 mm below the surface. These points follow the linear approximation, fitted to the samples made with laser focal position on the surface, quite well. However, as also concluded in section 5.1.1, the resistance of the samples made with a defocused laser is slightly larger than what the linear approximation gives at the given conductive path l/CSA . However, the resistance for the coupon samples made with a defocused laser was about 10% larger compared to the samples made with the focal position on the surface, whilst the resistance for the fine grained tube samples made with a defocused laser was only about 5% larger compared to linear approximation. This could be explained by the fact that the curvature of the tube makes the laser defocused at the sides of the measurement grids in the tube's tangential direction for every sample. Thus, no sample on the tubes is completely in focus. Hence, when the focal position is 1 mm below the uppermost surface, this will decrease (or in the best case; eliminate) the defocus on the sides of the measurement grids in the tube's tangential direction caused by the tube's curvature.

In tables 6 and 7, the heat response for the evaluated strain gauges on the coarse and fine grained tubes can be seen respectively. The heat response for samples on the coarse grained tube was $(378 \pm 51) \text{ ppm}/^\circ\text{C}$, whilst for samples on the fine grained tube, the heat response was $(1799 \pm 118) \text{ ppm}/^\circ\text{C}$.

In figures 36 and 37, it can be seen that the heat response for strain gauges on both the coarse and fine grained tubes does not seem to be dependent on the conductive path l/CSA , just as for the samples on the coupons. In addition, the sample that was ablated when using argon protective gas has almost the same heat response as the sample ablated without protective gas. The samples made with a defocused laser show a heat response in the same region as the rest of the samples.

In tables 6 and 7, the thermal drift for the evaluated strain gauges on the coarse and fine grained tubes can be seen respectively. The thermal drift for samples on the coarse grained tube was (7703 ± 3015) ppm, whilst for samples on the fine grained tube, the thermal drift was (3789 ± 1566) ppm.

In figures 38 and 39, it can be seen that the thermal drift for strain gauges on both the coarse and fine grained tubes does not seem to be dependent on the conductive path l/CSA , just as for the coupon samples. Furthermore, the sample that was ablated when using argon protective gas has slightly larger thermal drift than the sample ablated without protective gas. However, the amount of thermal drift seems to be a bit random for all the samples. Thus, the difference between the samples with and without protective gas could just be a random difference (caused by uncontrolled factors). The samples made with a defocused laser have a thermal drift in the same region as the rest of the samples.

In figure 40, the heating measurements on the strain gauge on the flame sprayed carbon steel tube can be seen. On this tube, glue was used for the contacts since the contact pads were too small to be able to affix the tape and get sufficient connection. Hence, the measurements are unreliable since the glue did not perform well at all during heating measurements. However, a roughly linear heat response during the end of the cooldown can be seen. Though unreliable, this would give a heat response on approximately $75 \text{ ppm}/^{\circ}\text{C}$, which is much lower (which is desirable of a strain gauge) than for all of the other samples, both on coupons and on the other tubes. In figure 40, a linear approximation can also be seen. This approximation has the same slope as the average slope of the linear part of the heat response during the end of the cooldown. This line intersects the relatively stable part of the measurement at the maximum temperature (approximately 160 degrees Celsius). Thus, indicating that the linear part of the cooldown can in fact be the actual heat response of the strain gauge.

5.2 Laser cladded thermocouples

In figure 41, it can be seen that the cladded thermocouple, connected with chromel and alumel, rise in temperature slower and to a lower maximum level than the reference K-type thermocouple. However, after the heat gun has been turned off, the registered temperature of the reference thermocouple immediately drops to the same level as for the cladded thermocouple. Then, both the reference and the cladded thermocouple have the same cooldown temperature curvature. Because both the reference and the cladded thermocouple have roughly the same cooldown temperature curvature, it was suspected that the cladded thermocouple did not really show up in the measurement. This could be since the temperature was most likely the same along the entire cladded thermocouple, thus not resulting in any thermoelectric effect in the cladded part. What is seen in figure 41 is probably only the K-type leads, connected to the cladded thermocouple, where the cladded part just served as a conductor connecting the two leads, hence the same cooldown curvatures. The difference in registered maximum temperature and the rise time could be explained by the factors affecting the actual temperature of the two thermocouples. For the reference thermocouple, only a very small junction of two leads had to be heated. For the leads connected to the cladded thermocouple, a large part of the tube had to be heated in order to heat the leads, hence, the cold ambient air affected the cladded thermocouple's temperature more than for the reference.

In figure 43, it can be seen that when both conductors are made of the same material, there is virtually no change in the registered temperature when heated, thus, there is virtually no induced voltage. Thus, when contacting the cladded thermocouple with leads of the same material, and if it is true that there is no induced voltage in the cladded thermocouple because of a uniform temperature throughout the entire cladded part, the registered temperature should remain constant when heated. In figure 42, this is almost the case.

In figure 42, it can be seen that the registered temperature decreases a small amount when being heated, and then almost immediately rises to the initial reading when the heat gun was turned off. Since the small decrease in registered temperature disappeared almost instantly after the heating gun was turned off, it is believed that change in registered temperature from the initial value is caused by different amounts of hot air reaching the two leads, thus giving the two leads slightly different temperature gradients. Hence, when the flow of hot air is turned off, the leads (because of their small size) quickly gets the same temperature as the tube and the registered temperature returns to its initial value.

6 Conclusions

6.1 Thick film strain gauges

The resistance of the strain gauges depends on the conductive path l/CSA . The resistivity of the conductive paths of the strain gauges has been determined to approximately $5\ \mu\Omega m$ for the strain gauges on the coupons, $7\ \mu\Omega m$ for the strain gauges on the coarse grained tube and $1.4\ \mu\Omega m$ for the strain gauges on the fine grained tube. The resistance also seems to depend on the laser focal position, where a defocused laser results in a higher resistance. It has also been seen that the resistance does not seem to be affected whether a protective gas (in this case argon) is used or not during the laser ablation.

The strain response could only be evaluated for the strain gauges on the coupons. These samples did not have a linear strain response. This indicates that the resistivity also changes during strains, which indicates e.g. microstructural changes during strains and that there perhaps are micro-cracks (possibly caused by the laser ablation) present in the measuring grid of the strain gauge. Some samples have a more linear strain response than others. However, this cannot be explained by the investigated production parameters, rather, it seems to be caused by random and uncontrolled differences in the APS and/or laser ablation processes. It has been seen that the strain hysteresis does not seem to be affected whether the laser ablation was made with nano- or picosecond laser pulses. It has also been seen that the hysteresis does not seem to be affected by the conductive path l/CSA , nor by the laser focal position. Thus, the differences in hysteresis cannot be explained by the investigated production parameters either.

Concerning the heat response, samples that have a more linear strain response also seems to have a larger heat response. It is clear that the heat response depends on the laser focal position, where a defocused laser results in a slightly smaller heat response. When comparing the coarse and fine grained tubes, the heat response is in general found to be about five times larger for samples on the fine grained tube, and the thermal drift is in general found to be about two times larger for samples on the coarse grained tube. It has been seen that the thermal drift seems to be dependent on the laser focal position, where a defocused laser results in a larger thermal drift.

Not much can be concluded about the strain gauge on the flame sprayed carbon steel tube because of an unreliable connection, probably caused by the glued contacts. However, whilst unreliable, the heat response on this sample is approximately only $75\ \text{ppm}/^\circ\text{C}$, which is much smaller than for any other evaluated sample.

6.2 Laser clad thermocouples

Not much can be concluded about the clad thermocouples since no suitable way of heating only the junction was found, which led to that the clad thermocouple could not be seen in the measurements. However, it can be concluded that two different alloys can be clad in an overlapping manner and be electrically conductive.

6.3 Future work

Much research and development remain on the thick-film sensors. There are currently some ideas for improvement and further development. However, these cannot be shared in this report due to confidentiality.

7 References

- [1] Sandvik Materials Technology, "Sentusys™ – Sandvik intelligent tube system," Sandvik AB, [Online]. Available: <https://www.materials.sandvik/en/products/services/digital-monitoring/intelligent-tube-system/>. [Accessed 01 10 2020].
- [2] Sandvik Materials Technology, "Master thesis: Optimization of high-temperature sensors," Sandvik AB, [Online]. Available: <https://www.home.sandvik/se/karriar/student/examensarbete/thesis-projects/optimization-of-high-temperature-sensors/>. [Använd 01 10 2020].
- [3] Wikipedia contributors, "Electrical resistivity and conductivity," 13 10 2020. [Online]. Available: https://en.wikipedia.org/w/index.php?title=Electrical_resistivity_and_conductivity&oldid=983381007. [Använd 16 10 2020].
- [4] K. Hoffmann, An Introduction to Stress Analysis and Transducer Design using Strain Gauges - The definitive work on strain gauge measurement, HBM.
- [5] Wikipedia contributors, "Four-terminal sensing," 13 12 2019. [Online]. Available: https://en.wikipedia.org/w/index.php?title=Four-terminal_sensing&oldid=930589147. [Använd 04 11 2020].
- [6] Wikipedia contributors, "Thermocouple," 25 10 2020. [Online]. Available: <https://en.wikipedia.org/w/index.php?title=Thermocouple&oldid=985285767>. [Använd 28 10 2020].
- [7] Concept Alloys, "Type K Chromel Alumel Thermocouple Wire," [Online]. Available: <https://conceptalloys.com/products-type-k/>. [Använd 06 11 2020].
- [8] Wikipedia contributors, "Thermal spraying," 16 10 2020. [Online]. Available: https://en.wikipedia.org/w/index.php?title=Thermal_spraying&oldid=983781500. [Använd 28 10 2020].
- [9] Metallisation Limited, "Introduction to Thermal Spray and Engineering Applications," 2020. [Online]. Available: <https://www.metallisation.com/applications/thermal-spray-engineering-applications/>. [Använd 28 10 2020].
- [10] Metallisation Limited, "Plasma Spray," 2020. [Online]. Available: <https://www.metallisation.com/product-category/plasma-spray/>. [Använd 29 10 2020].
- [11] Metallisation Limited, "Flame Spray Equipment," 2020. [Online]. Available: <https://www.metallisation.com/product-category/flame-spray/>. [Använd 29 10 2020].
- [12] K. Weman, Welding Processes Handbook, Second Edition, Woodhead Publishing Limited, 2012.
- [13] Wikipedia contributors, "Laser ablation," 28 10 2020. [Online]. Available: https://en.wikipedia.org/w/index.php?title=Laser_ablation&oldid=985818413. [Använd 29 10 2020].
- [14] E. Lundin, "Small-scale laser cutting for stent, tube fabrication," The Tube & Pipe Journal, 27 10 2015. [Online]. Available: <https://www.thefabricator.com/tubepipejournal/article/lasercutting/small-scale-laser-cutting-for-stent-tube-fabrication>. [Använd 29 10 2020].
- [15] Wikipedia contributors, "Cladding (metalworking)," 15 10 2020. [Online]. Available: [https://en.wikipedia.org/w/index.php?title=Cladding_\(metalworking\)&oldid=983574609](https://en.wikipedia.org/w/index.php?title=Cladding_(metalworking)&oldid=983574609). [Använd 29 10 2020].
- [16] Y. e. a. Zhang, "Laser Cladding of Embedded Sensors for Thermal Barrier Coating Applications," Vol. %1 av %2Coatings 2018, 8, 176, 2018.

Appendix 1 - Strain response measurements for the coupons

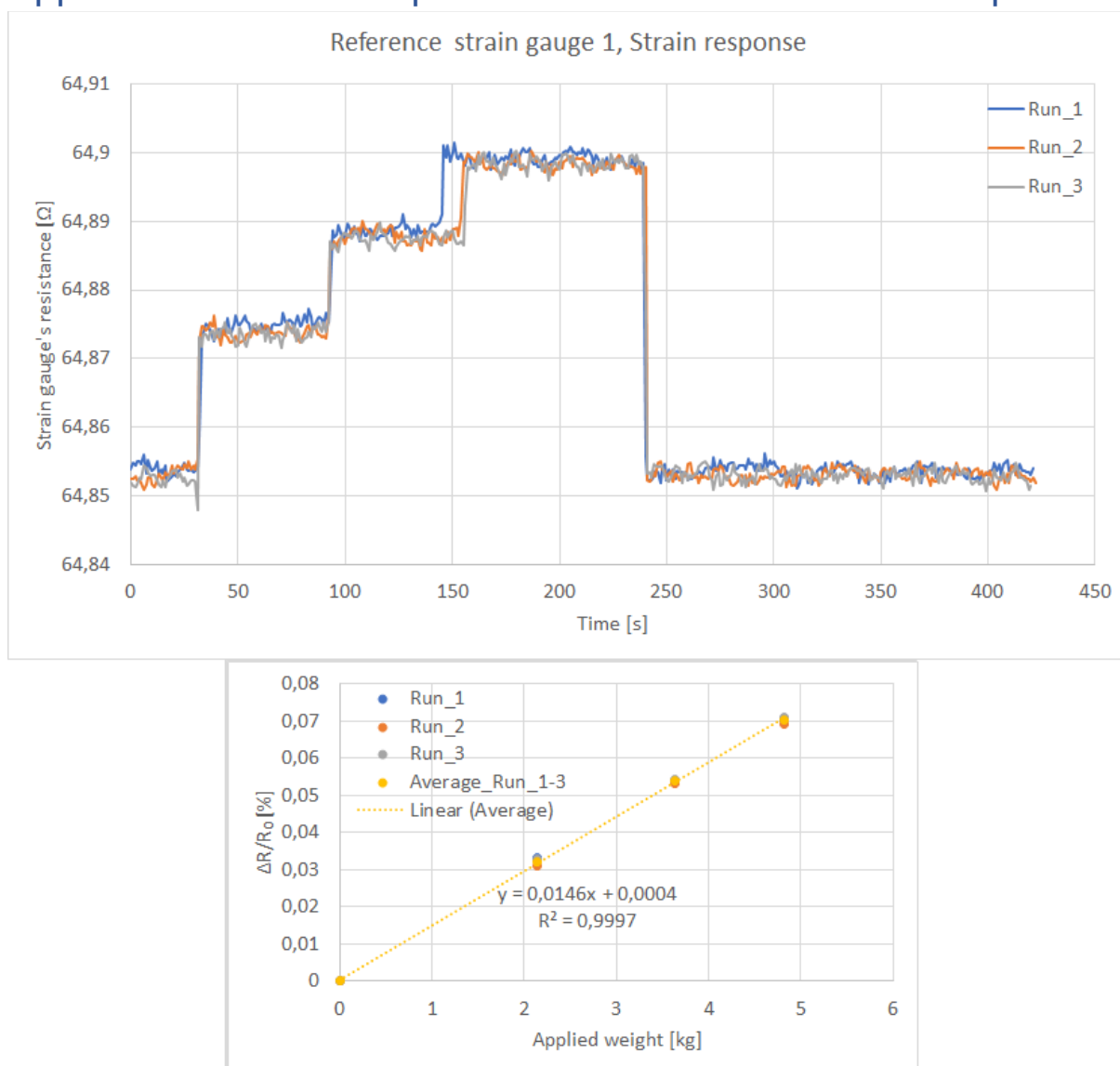


Figure A2-1: Strain response measurements on reference strain gauge 1. $\Delta R/R_0$ is the relative change of resistance in the strain gauge.

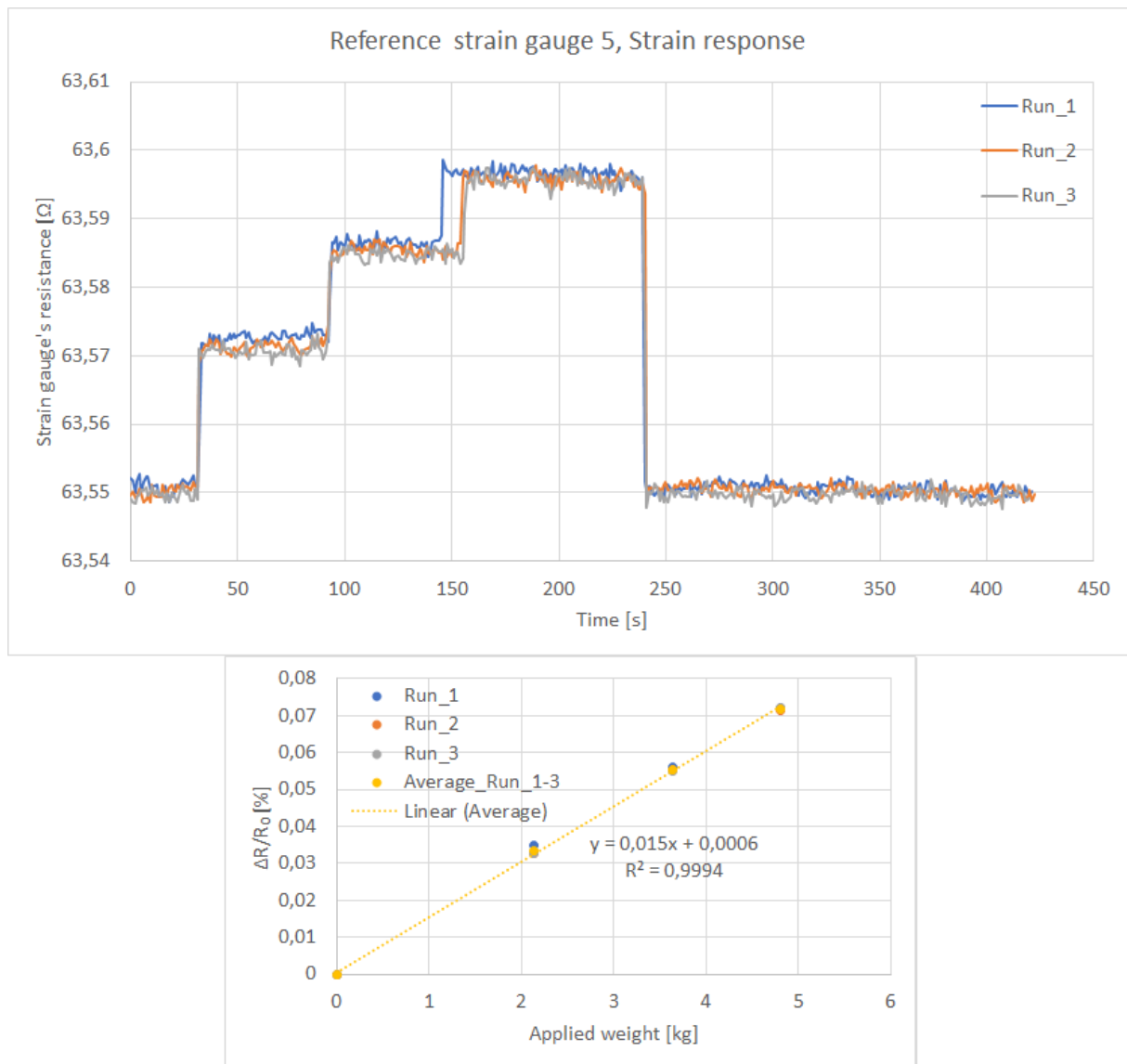


Figure A2-2: Strain response measurements on reference strain gauge 5. $\Delta R/R_0$ is the relative change of resistance in the strain gauge.

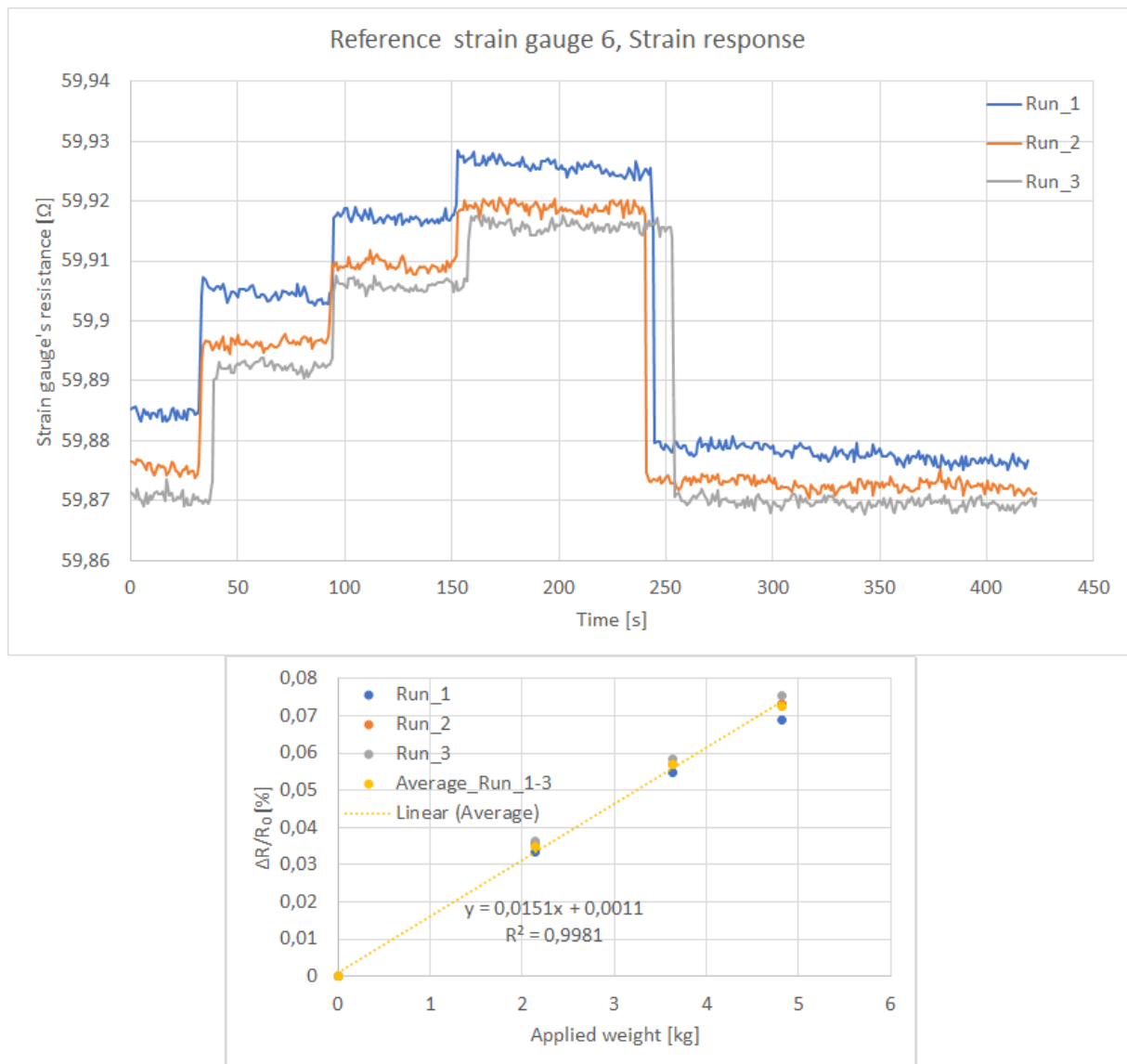


Figure A2-3: Strain response measurements on reference strain gauge 6. $\Delta R/R_0$ is the relative change of resistance in the strain gauge.

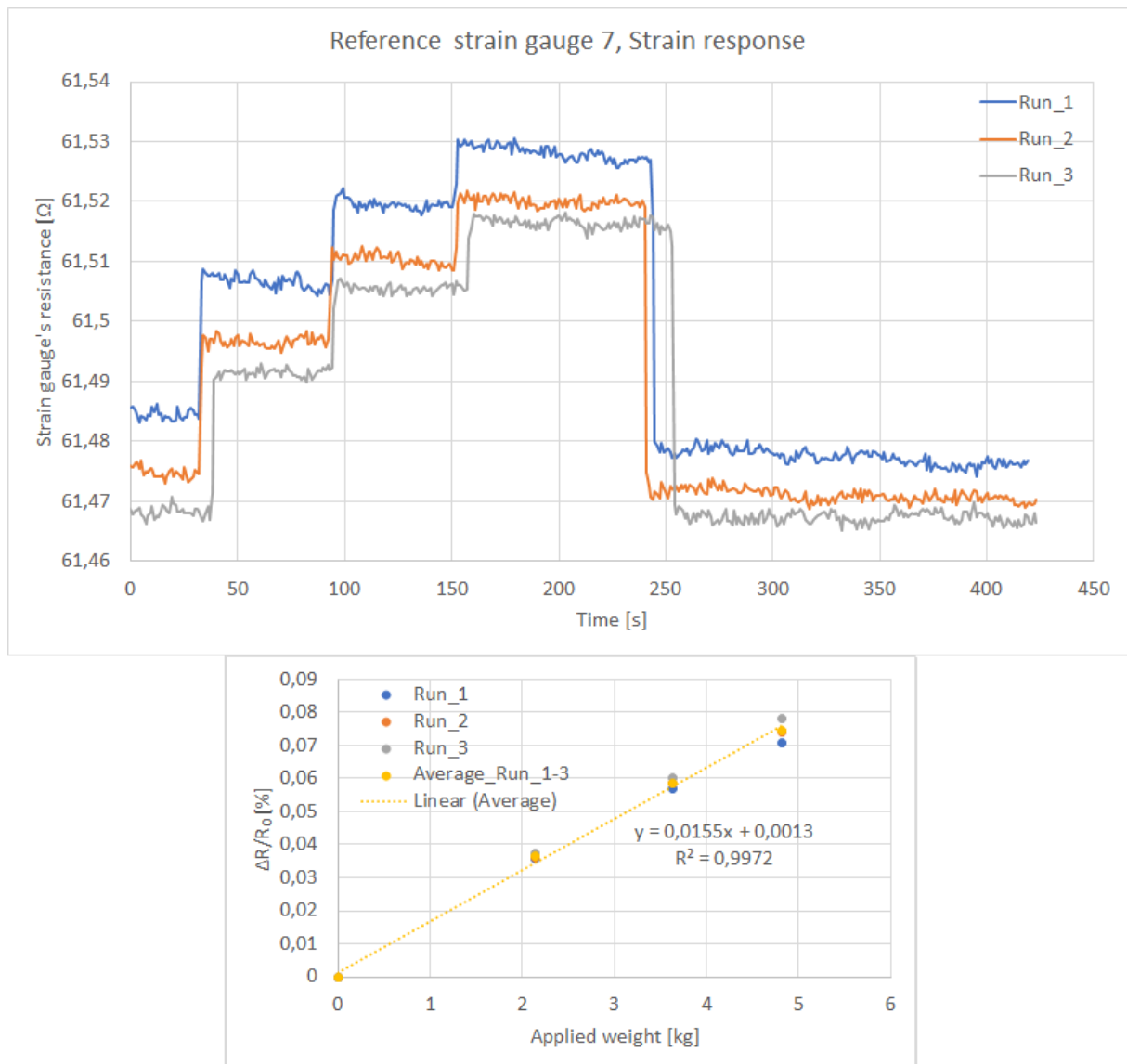


Figure A2-4: Strain response measurements on reference strain gauge 7. $\Delta R/R_0$ is the relative change of resistance in the strain gauge.



Figure A2-5: Strain response measurements on strain gauge 20 before heating measurements. $\Delta R/R_0$ is the relative change of resistance in the strain gauge.

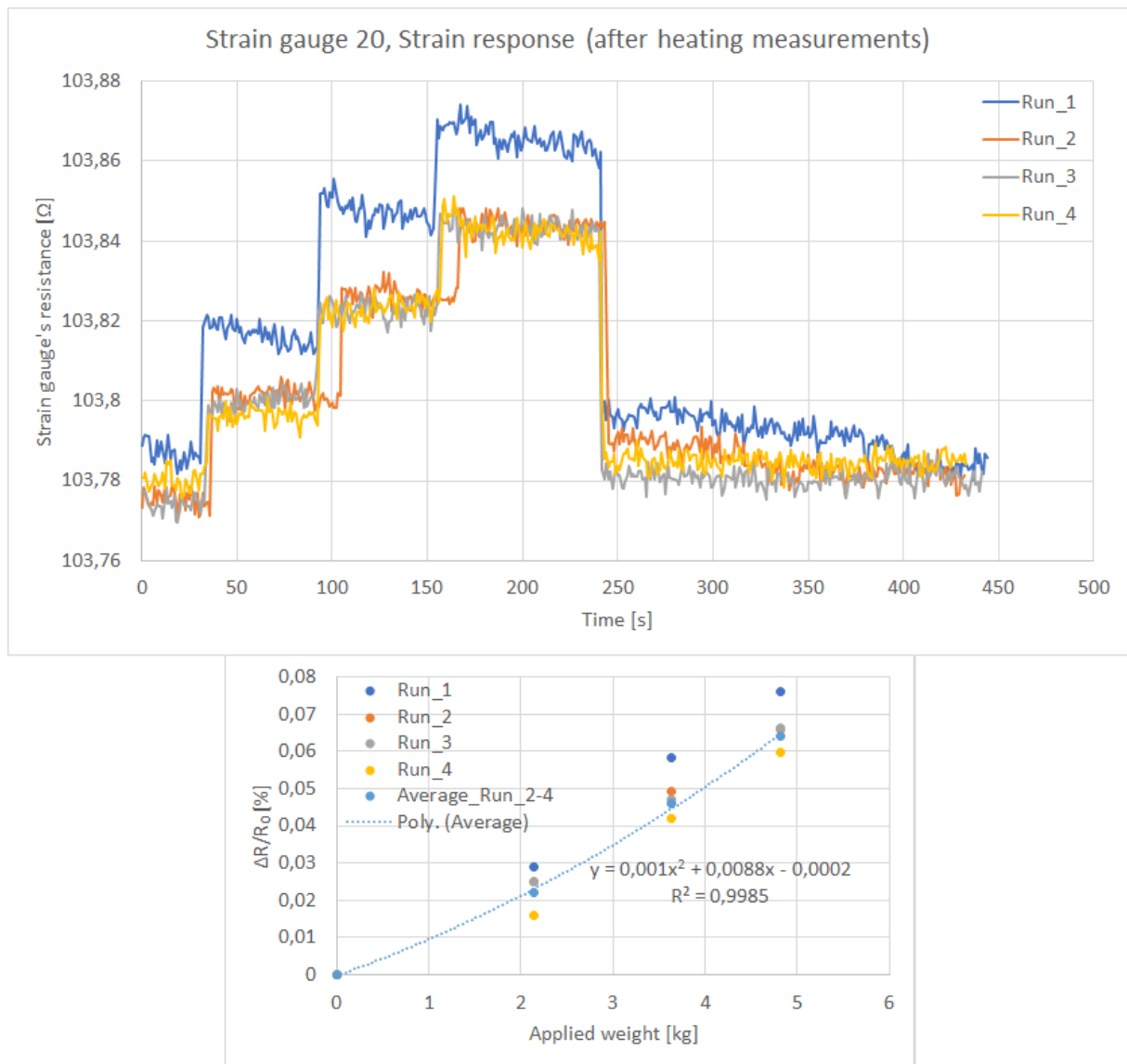


Figure A2-6: Strain response measurements on strain gauge 20 after heating measurements. $\Delta R/R_0$ is the relative change of resistance in the strain gauge.

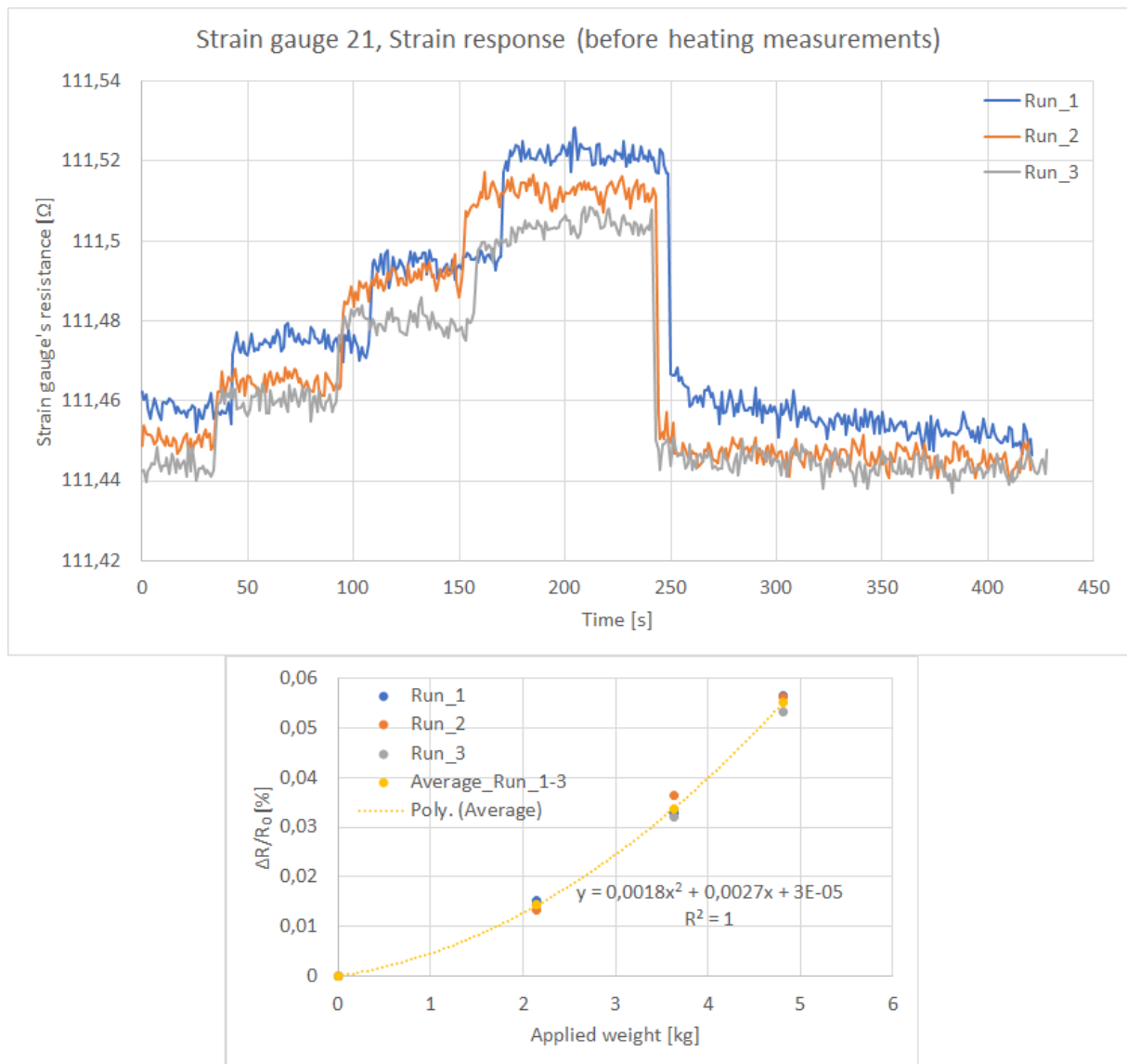


Figure A2-7: Strain response measurements on strain gauge 21 before heating measurements. $\Delta R/R_0$ is the relative change of resistance in the strain gauge.



Figure A2-8: Strain response measurements on strain gauge 21 after heating measurements. $\Delta R/R_0$ is the relative change of resistance in the strain gauge.

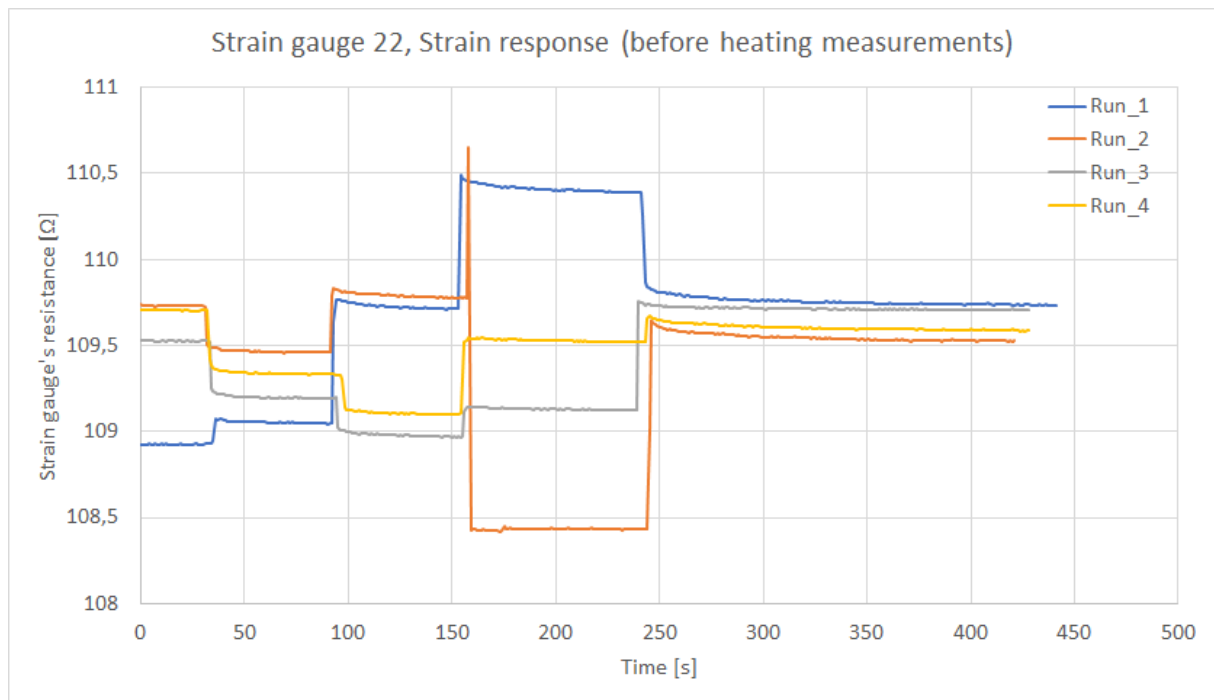


Figure A2-9: Strain response measurements on strain gauge 22 before heating measurements.

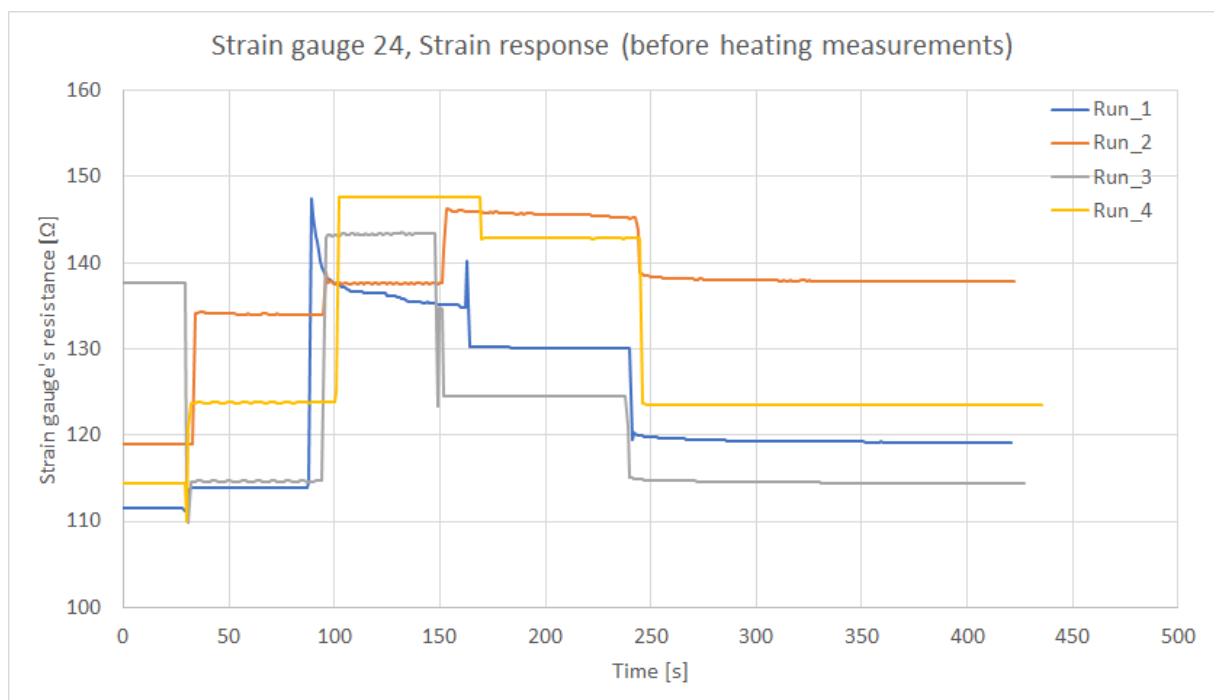


Figure A2-10: Strain response measurements on strain gauge 24 before heating measurements.

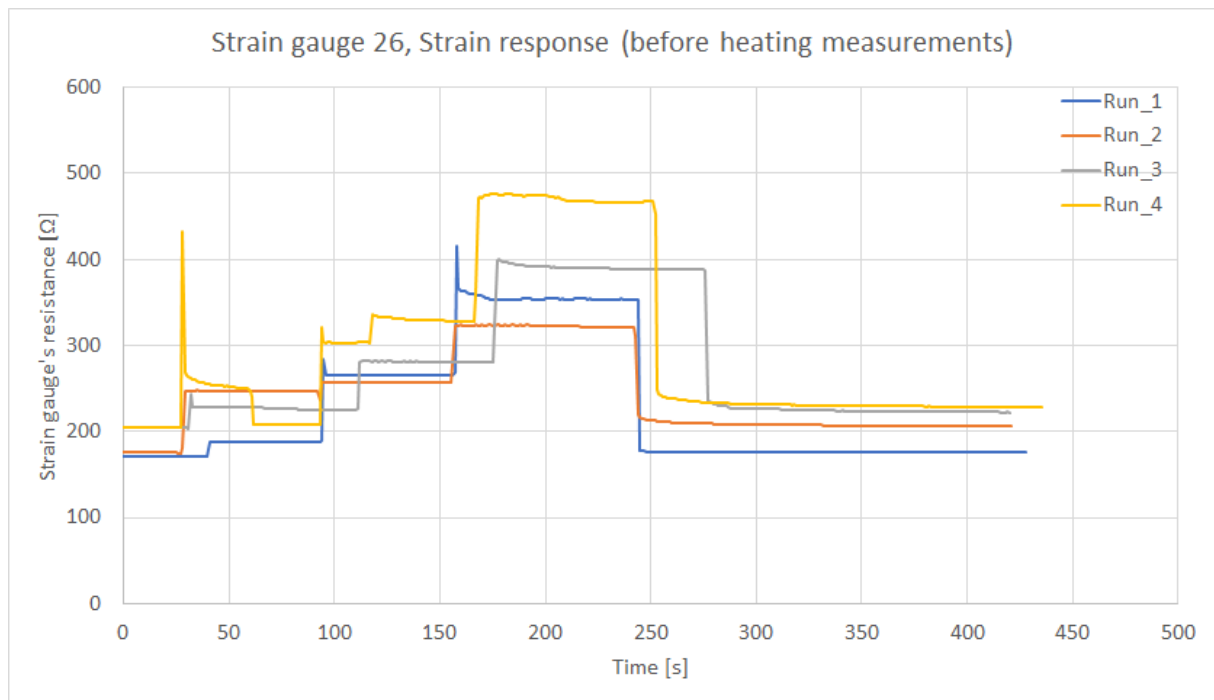


Figure A2-11: Strain response measurements on strain gauge 26 before heating measurements.



Figure A2-12: Strain response measurements on strain gauge 31 before heating measurements. $\Delta R/R_0$ is the relative change of resistance in the strain gauge.

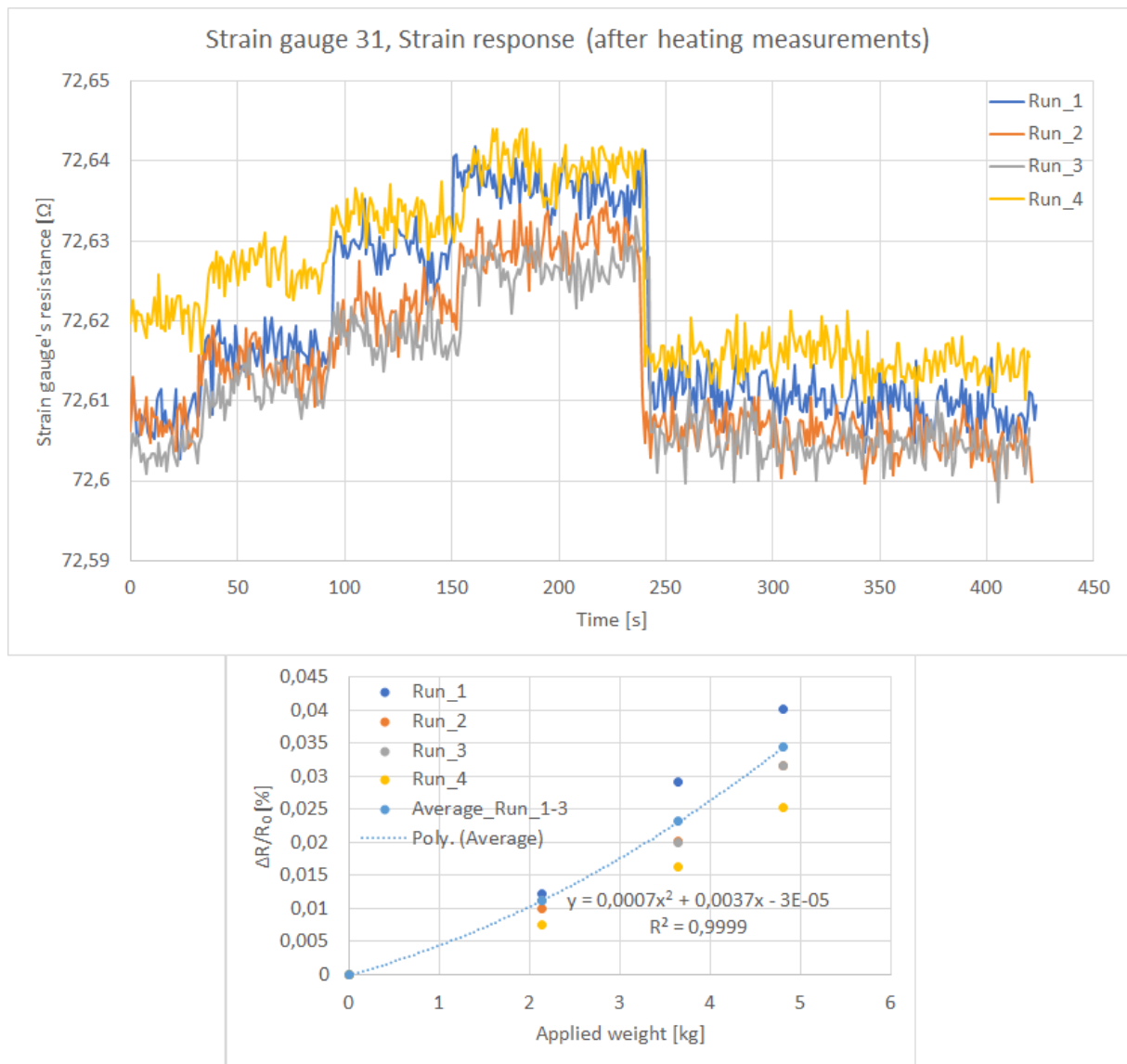


Figure A2-13: Strain response measurements on strain gauge 31 after heating measurements. $\Delta R/R_0$ is the relative change of resistance in the strain gauge.



Figure A2-14: Strain response measurements on strain gauge 35 before heating measurements. $\Delta R/R_0$ is the relative change of resistance in the strain gauge.

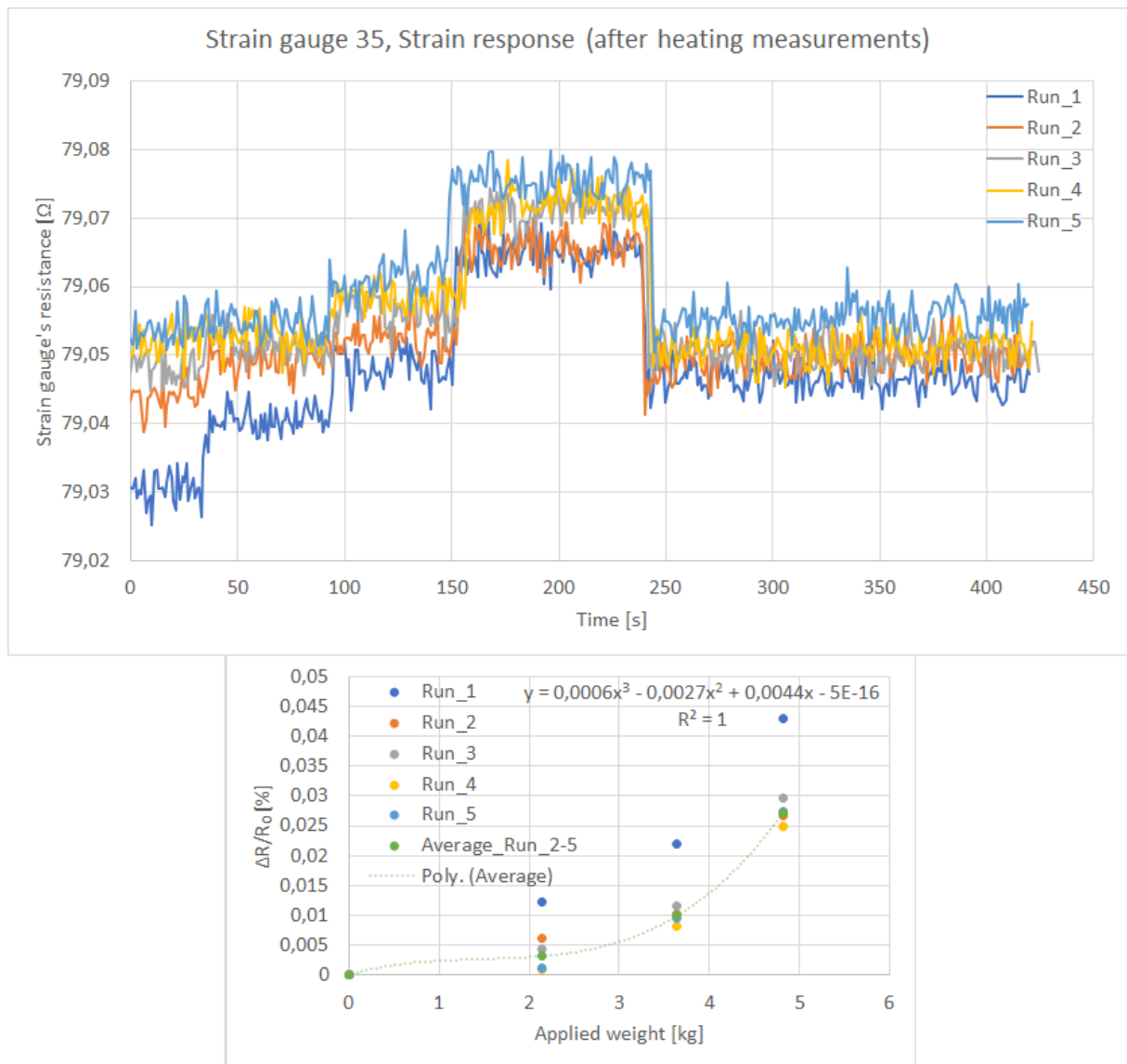


Figure A2-15: Strain response measurements on strain gauge 35 after heating measurements. $\Delta R/R_0$ is the relative change of resistance in the strain gauge.

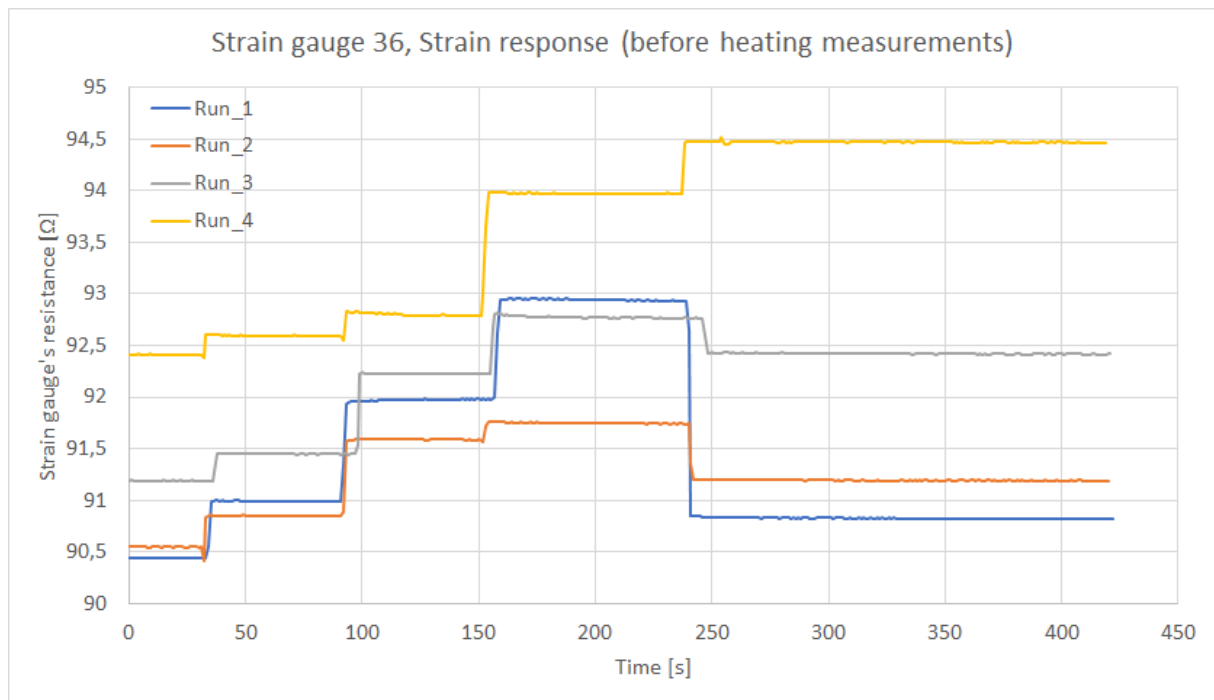


Figure A2-16: Strain response measurements on strain gauge 36 before heating measurements.

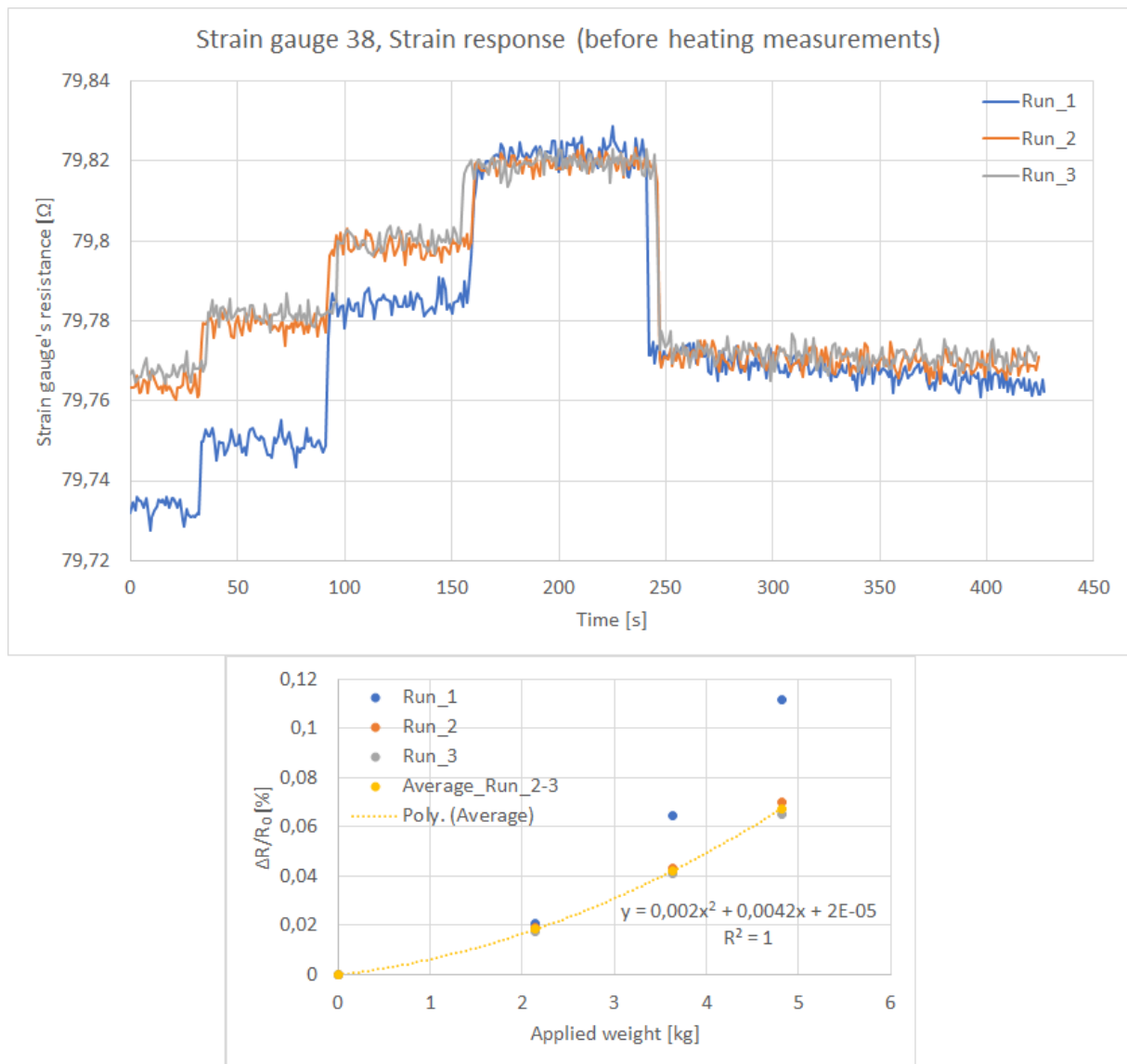


Figure A2-17: Strain response measurements on strain gauge 38 before heating measurements. $\Delta R/R_0$ is the relative change of resistance in the strain gauge.



Figure A2-18: Strain response measurements on strain gauge 38 after heating measurements. $\Delta R/R_0$ is the relative change of resistance in the strain gauge.

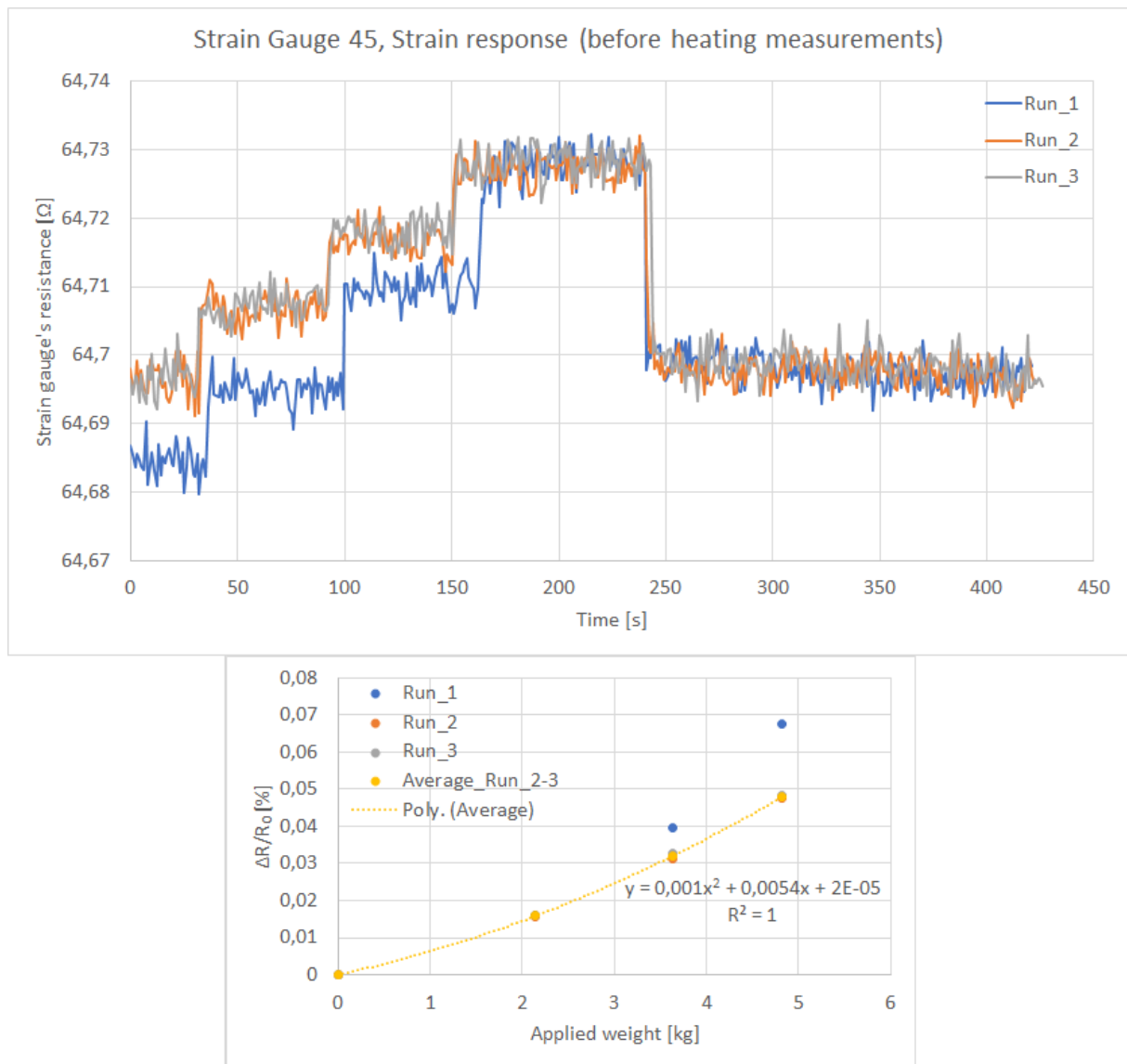


Figure A2-19: Strain response measurements on strain gauge 45 before heating measurements. $\Delta R/R_0$ is the relative change of resistance in the strain gauge.



Figure A2-20: Strain response measurements on strain gauge 45 after heating measurements. $\Delta R/R_0$ is the relative change of resistance in the strain gauge.

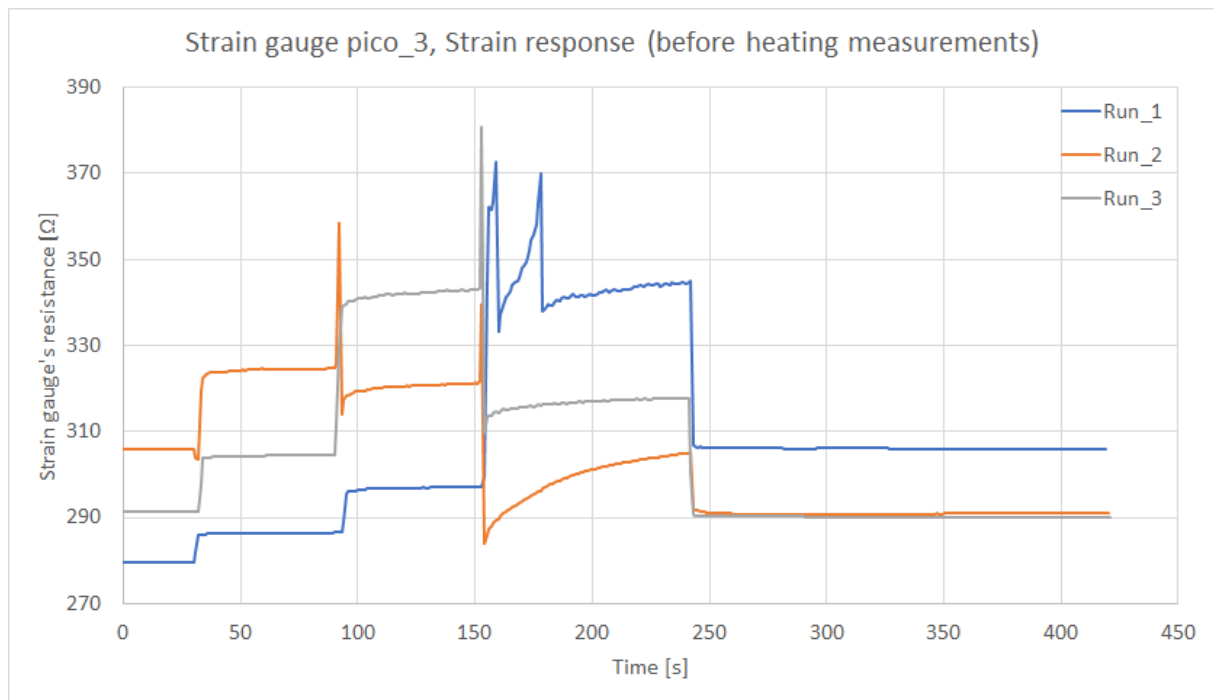


Figure A2-21: Strain response measurements on strain gauge pico_3 before heating measurements.

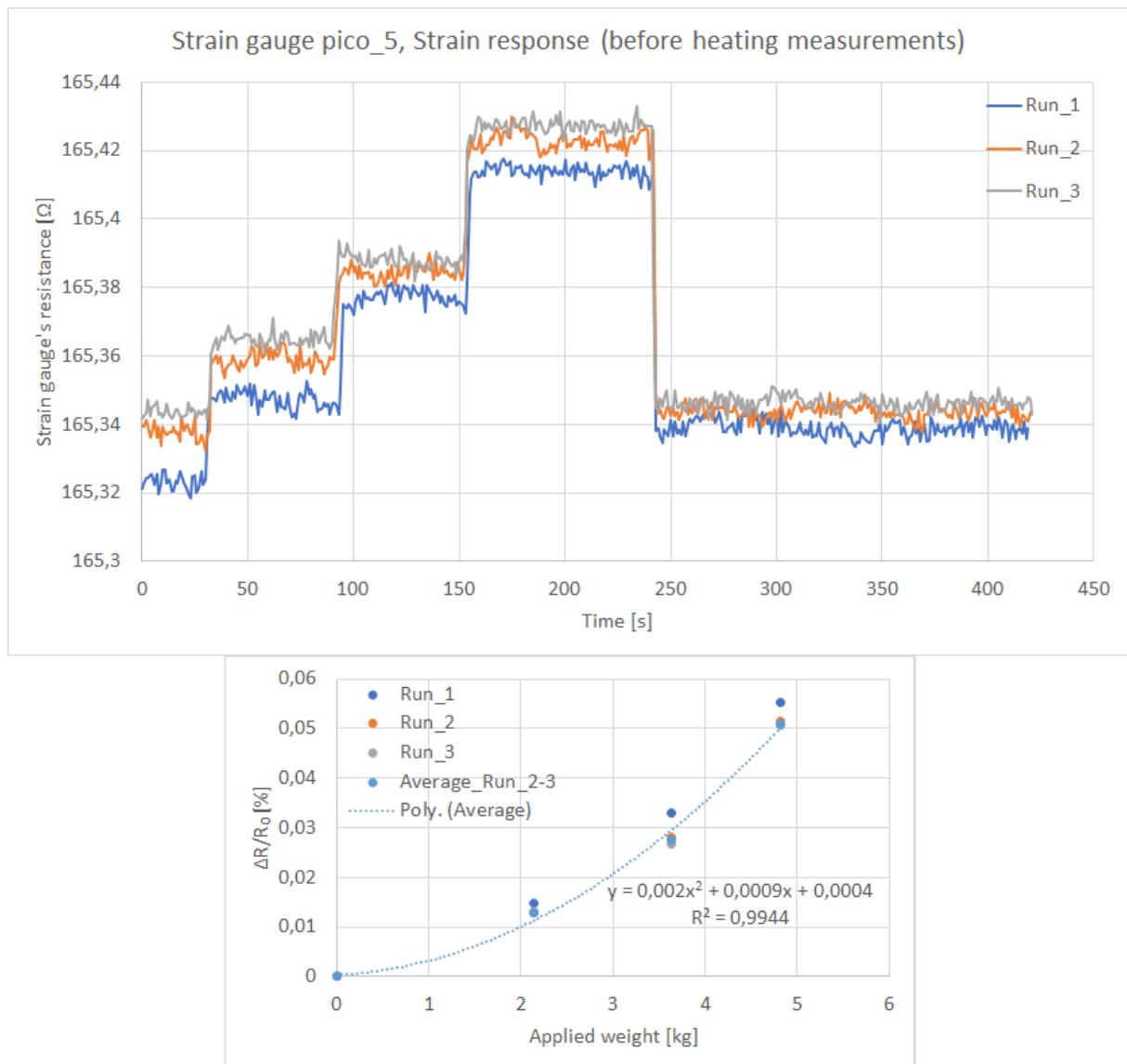


Figure A2-22: Strain response measurements on strain gauge pico_5 before heating measurements. $\Delta R/R_0$ is the relative change of resistance in the strain gauge.

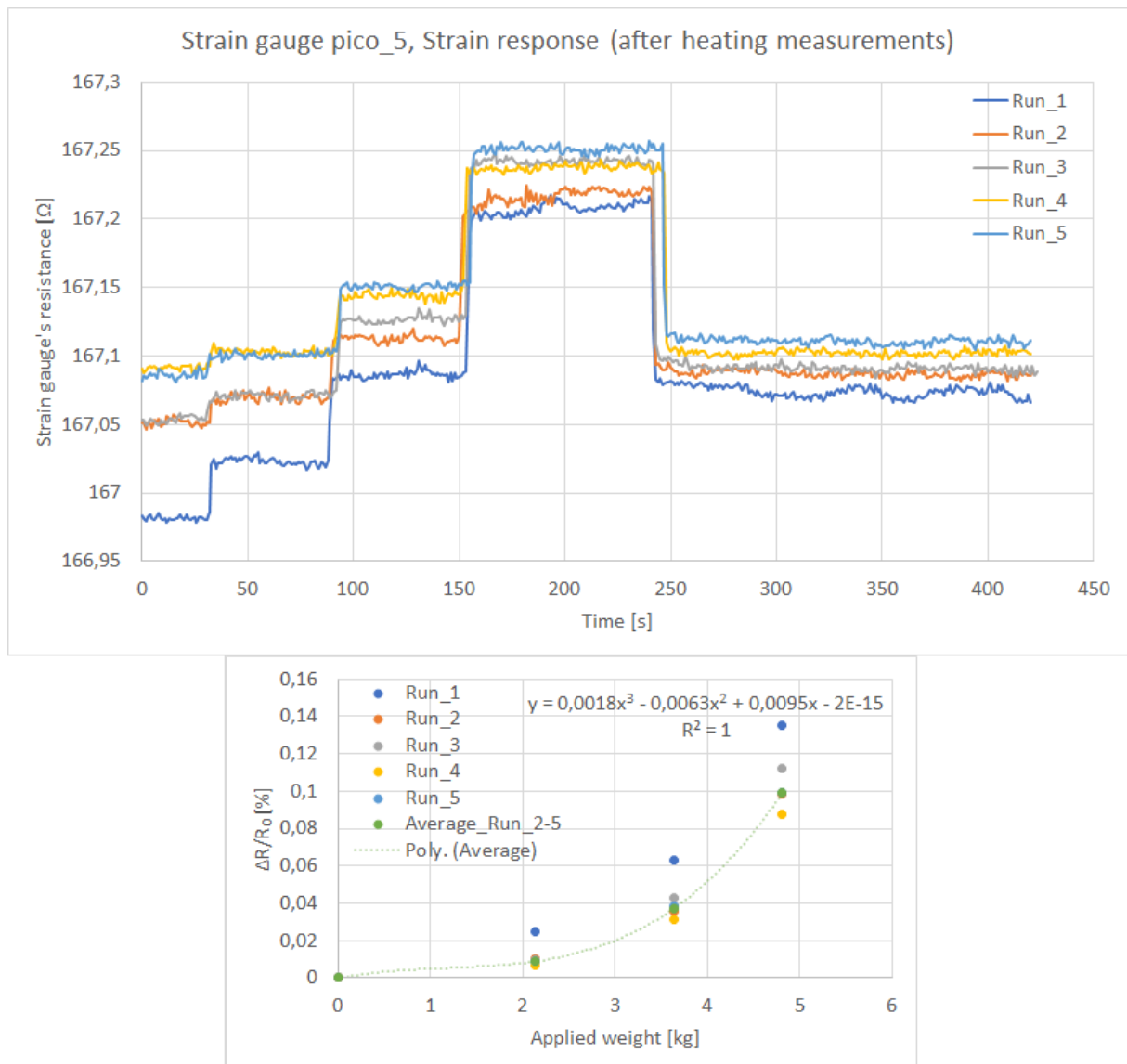


Figure A2-23: Strain response measurements on strain gauge pico_5 after heating measurements. $\Delta R/R_0$ is the relative change of resistance in the strain gauge.

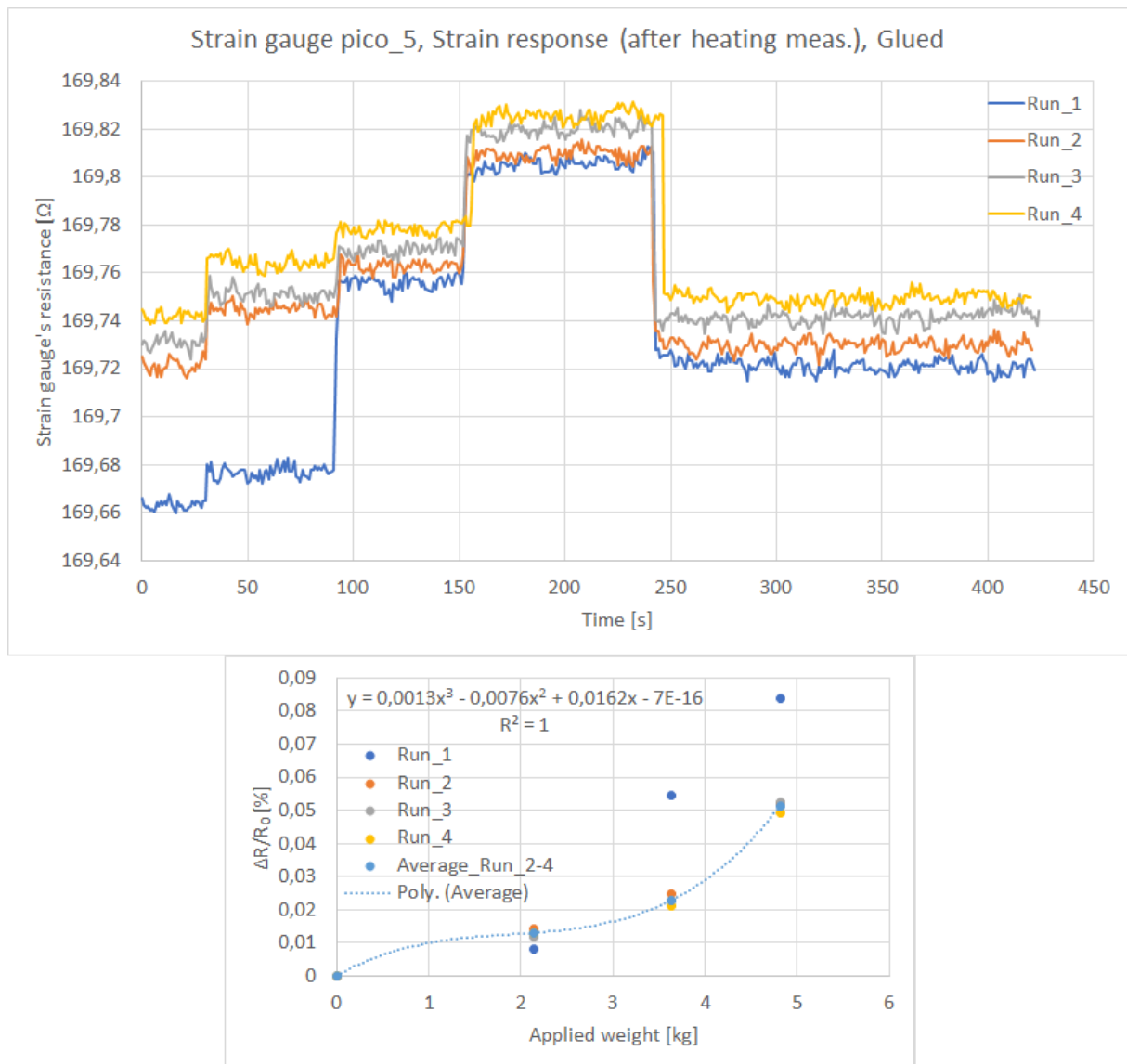


Figure A2-24: Strain response measurements on strain gauge pico_5, with glued contacts, after heating measurements. $\Delta R/R_0$ is the relative change of resistance in the strain gauge.

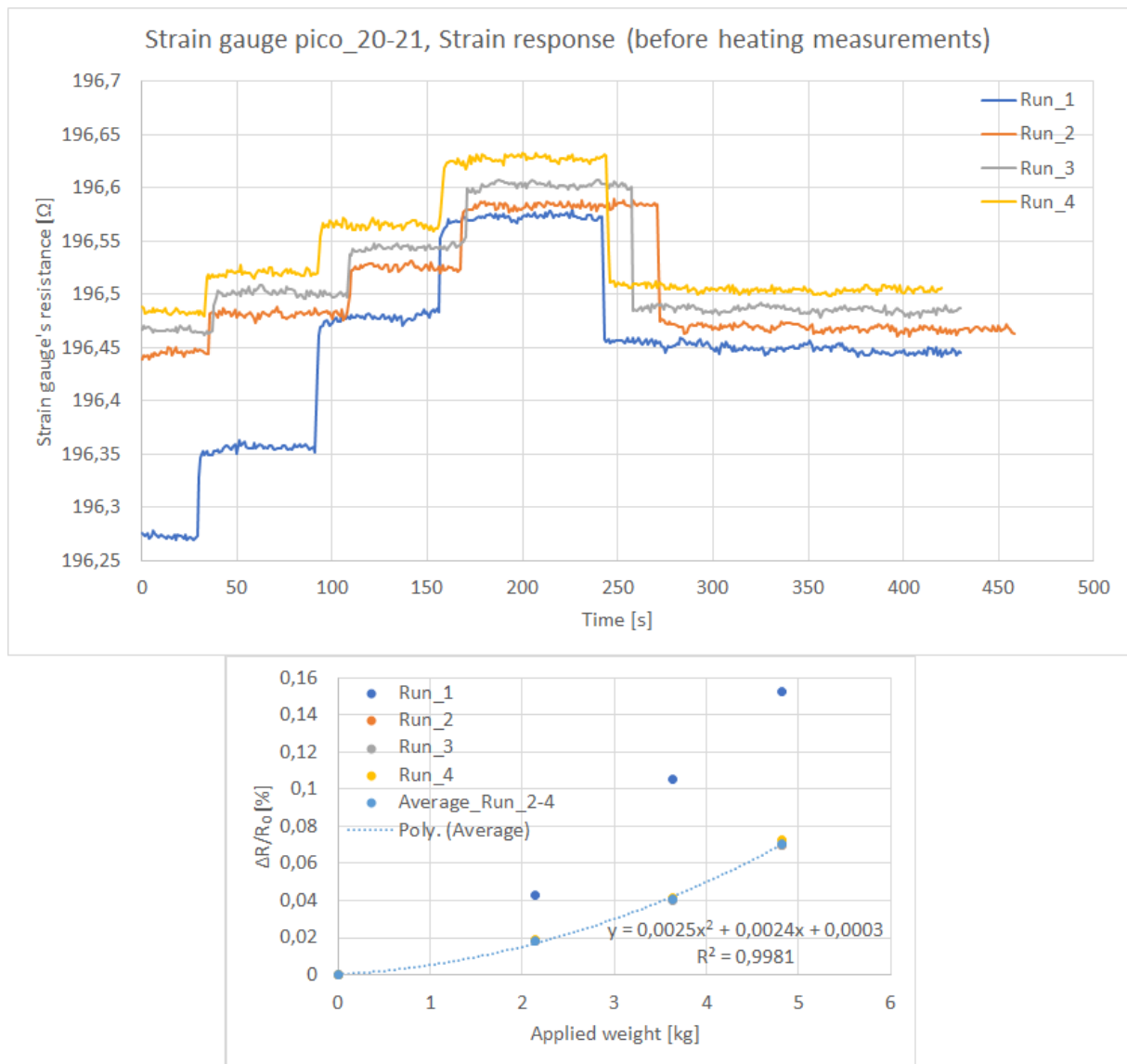


Figure A2-25: Strain response measurements on strain gauge pico_20-21 before heating measurements. $\Delta R/R_0$ is the relative change of resistance in the strain gauge.

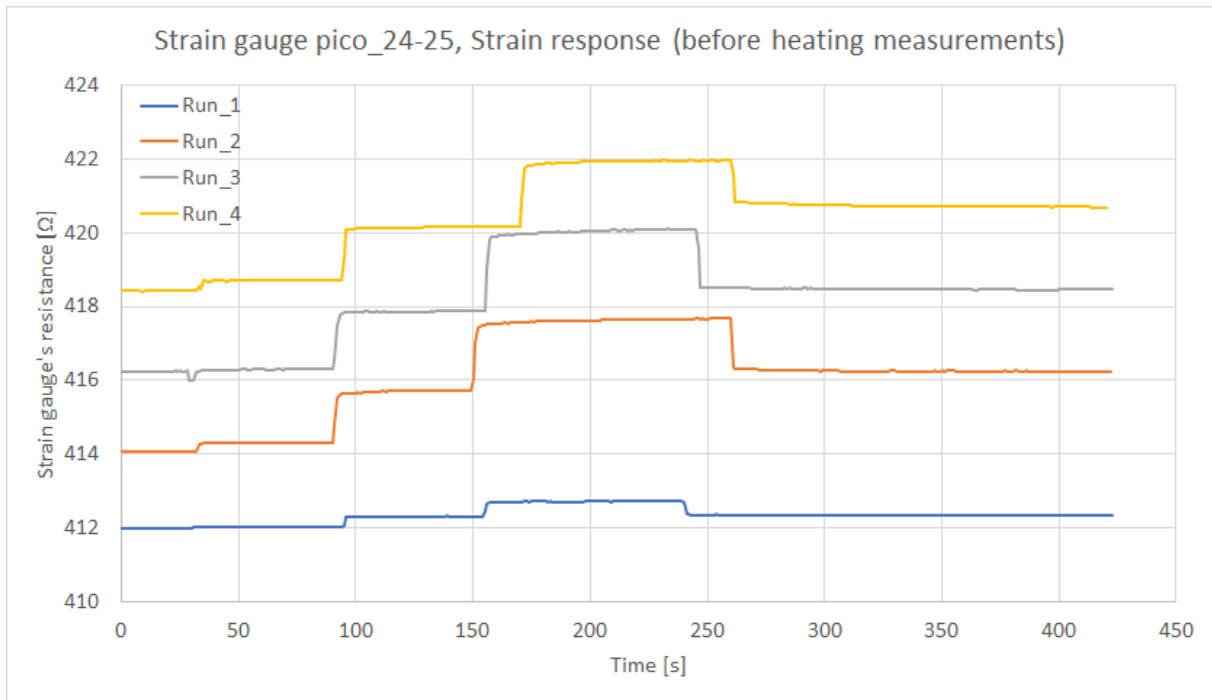


Figure A2-26: Strain response measurements on strain gauge pico_24-25 before heating measurements.

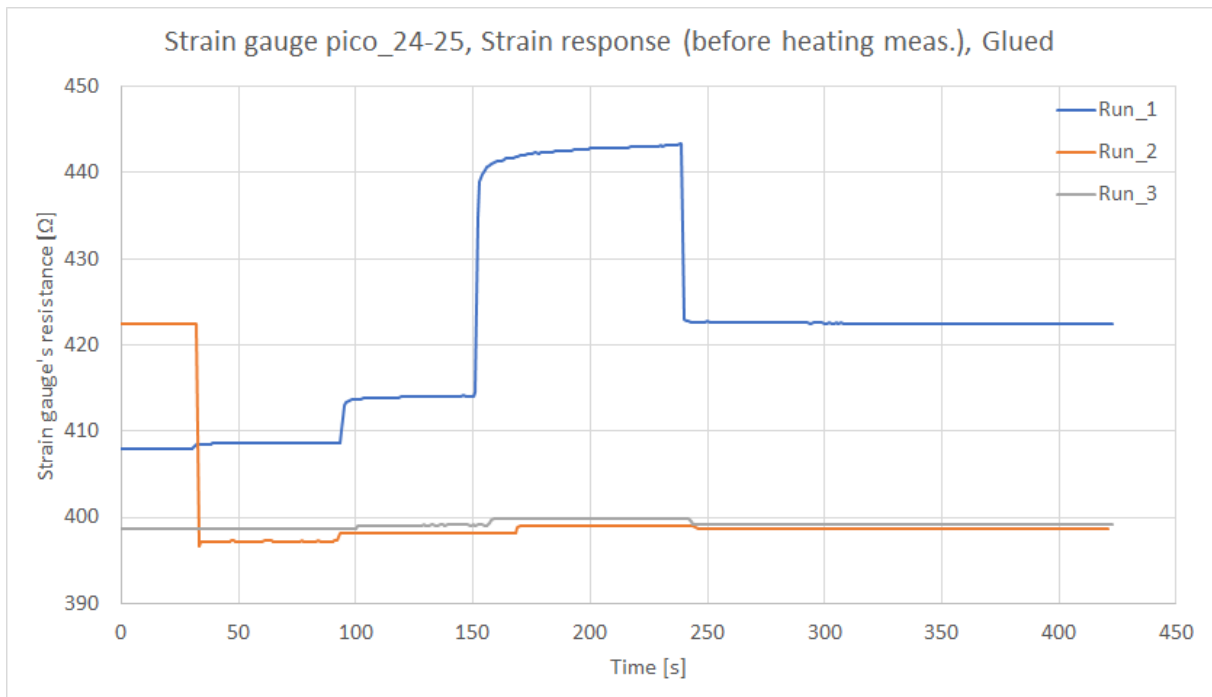


Figure A2-27: Strain response measurements on strain gauge pico_24-25, with glued contacts, before heating measurements.

Appendix 2 - Heat response measurements

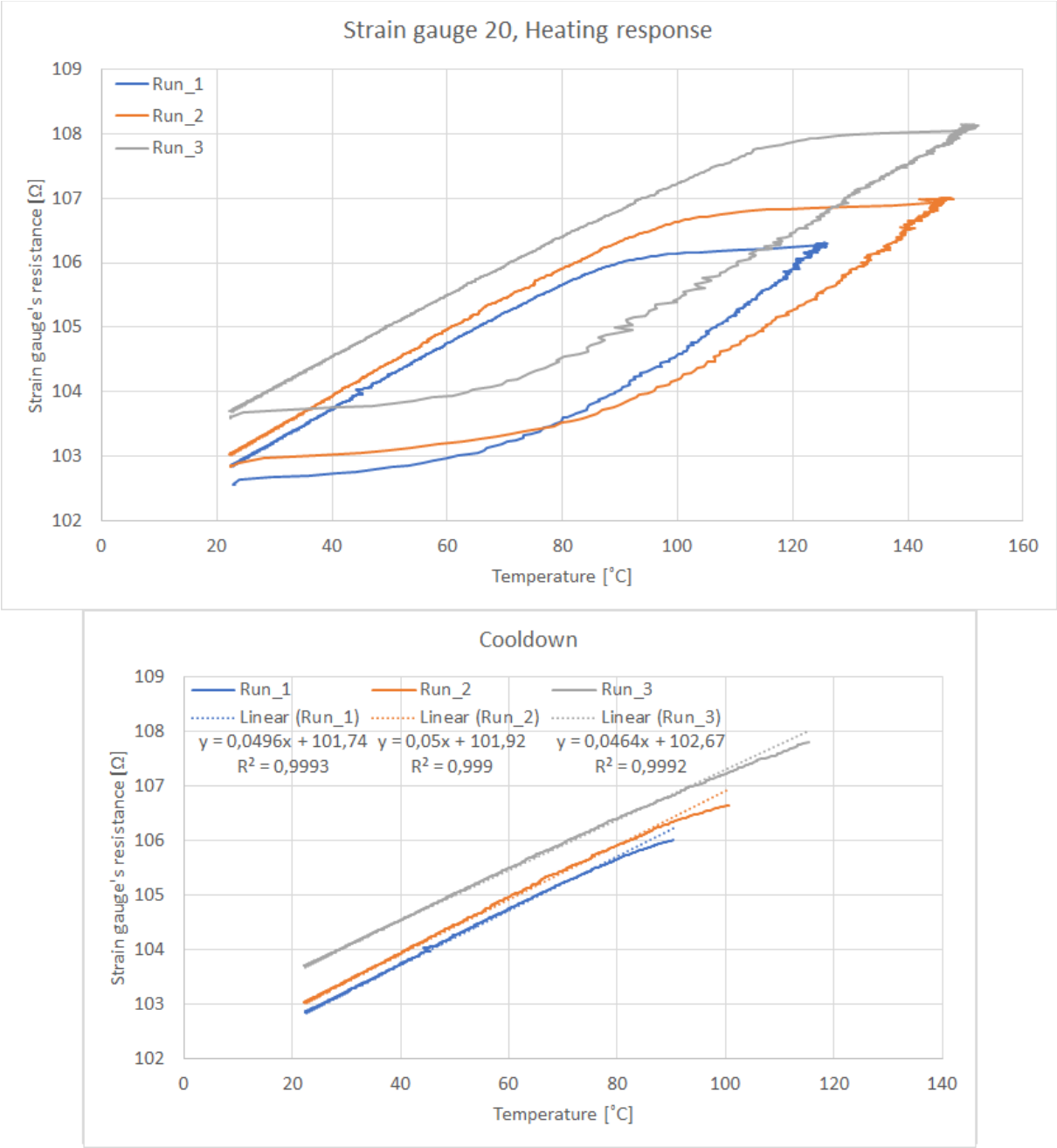


Figure A3-1: Heat response measurements on coupon strain gauge 20.

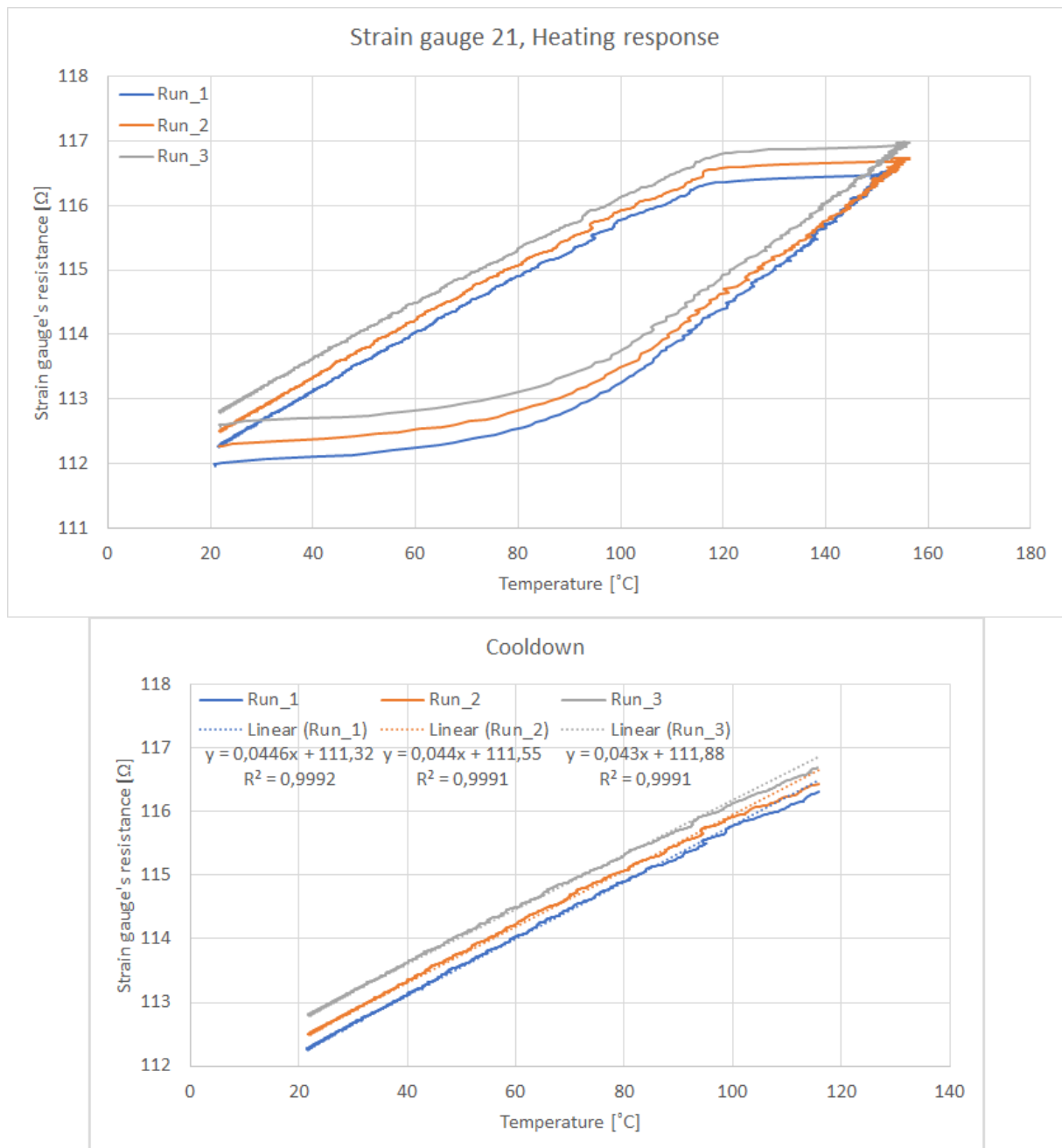


Figure A3-2: Heat response measurements on coupon strain gauge 21.

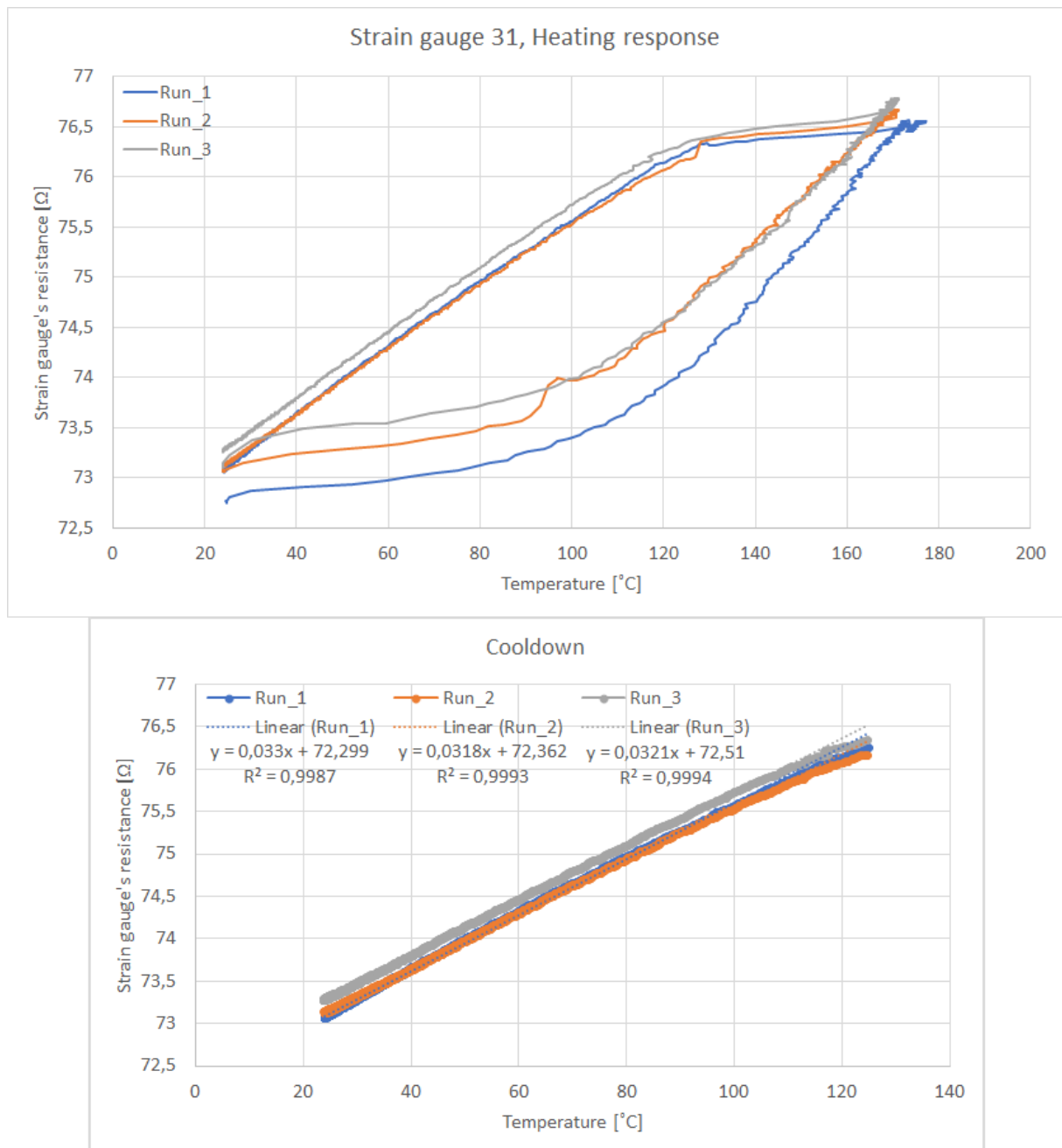


Figure A3-3: Heat response measurements on coupon strain gauge 31.

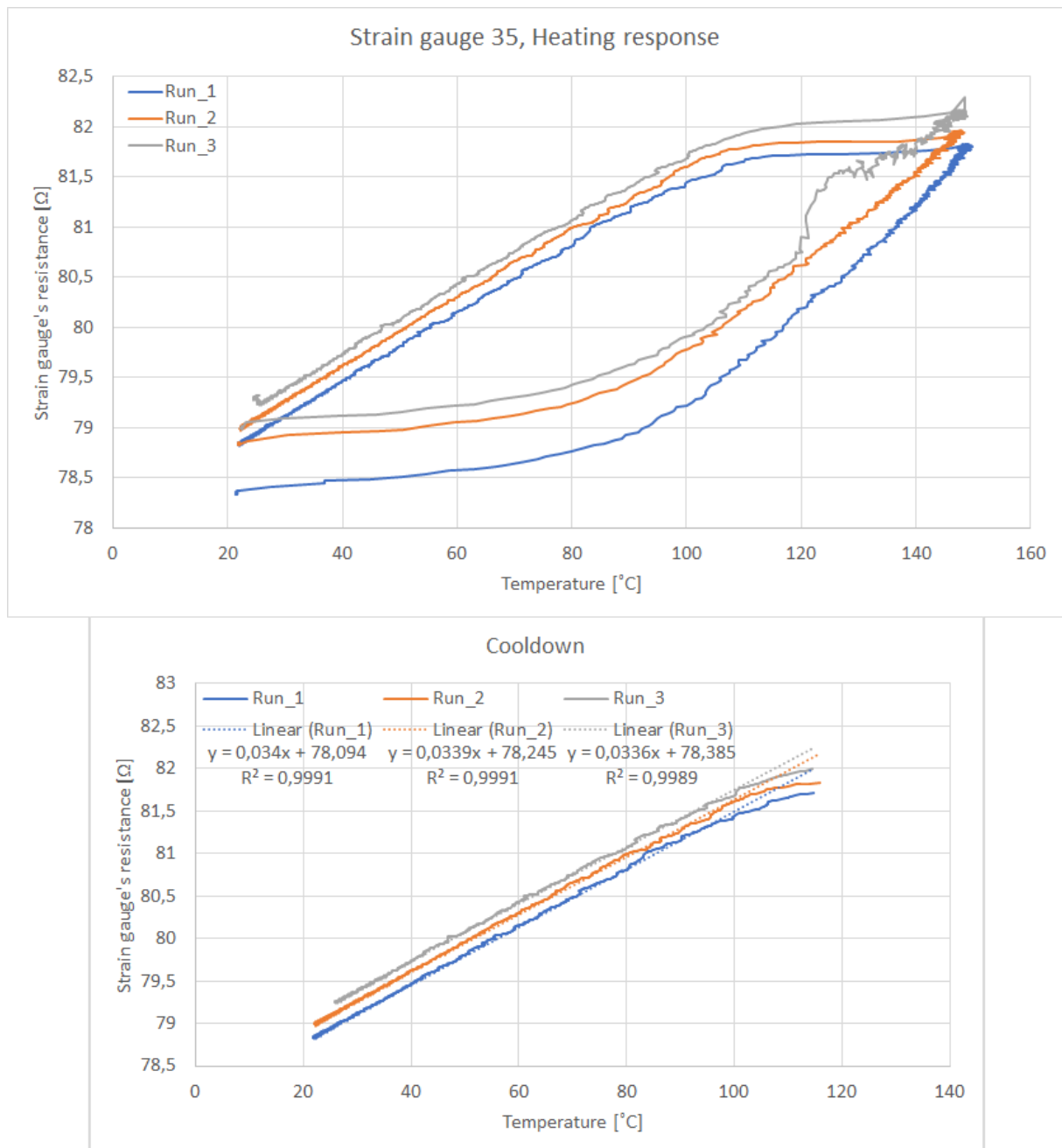


Figure A3-4: Heat response measurements on coupon strain gauge 35.

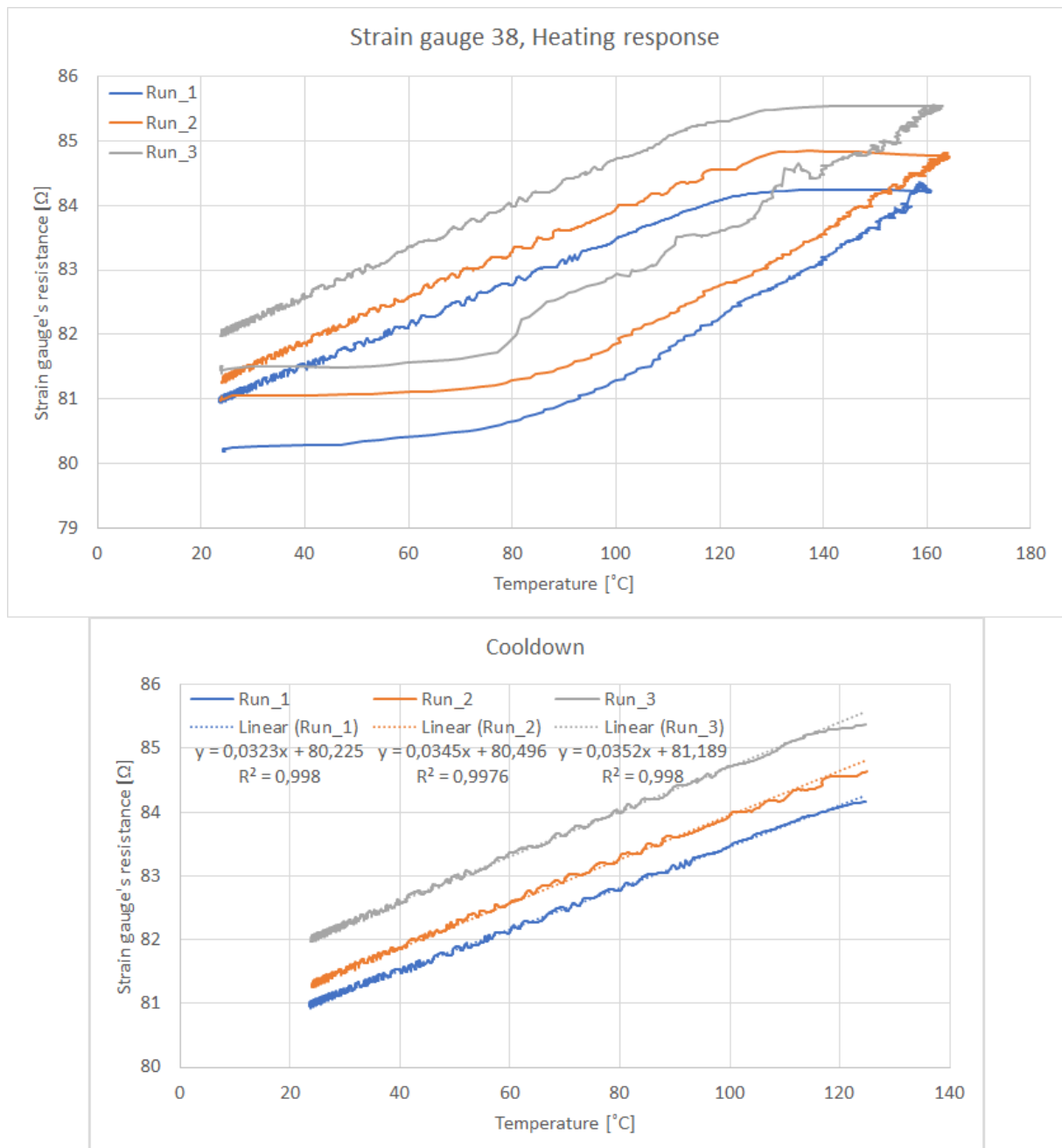


Figure A3-5: Heat response measurements on coupon strain gauge 38.

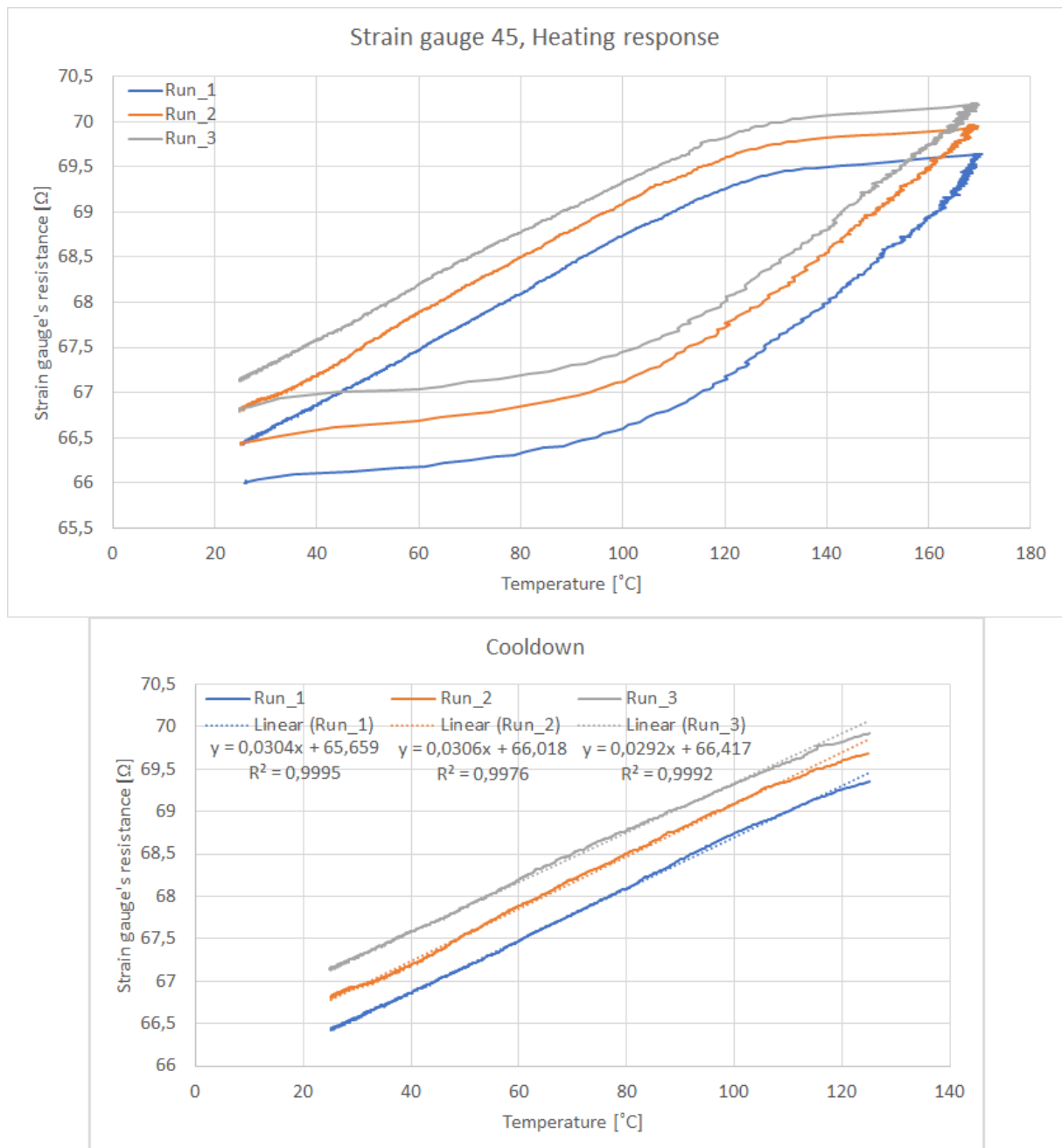


Figure A3-6: Heat response measurements on coupon strain gauge 45.

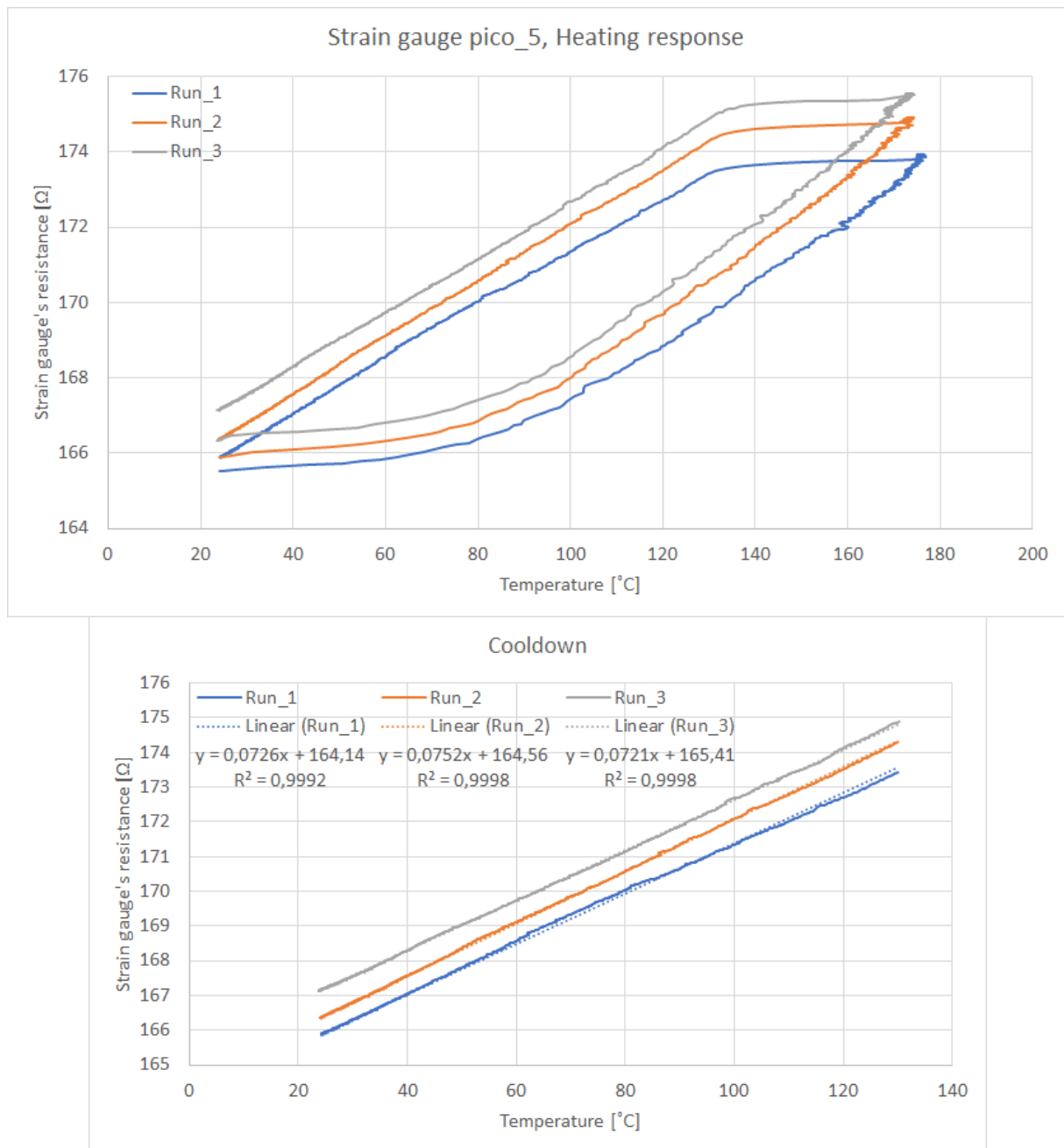


Figure A3-7: Heat response measurements on coupon strain gauge pico_5.

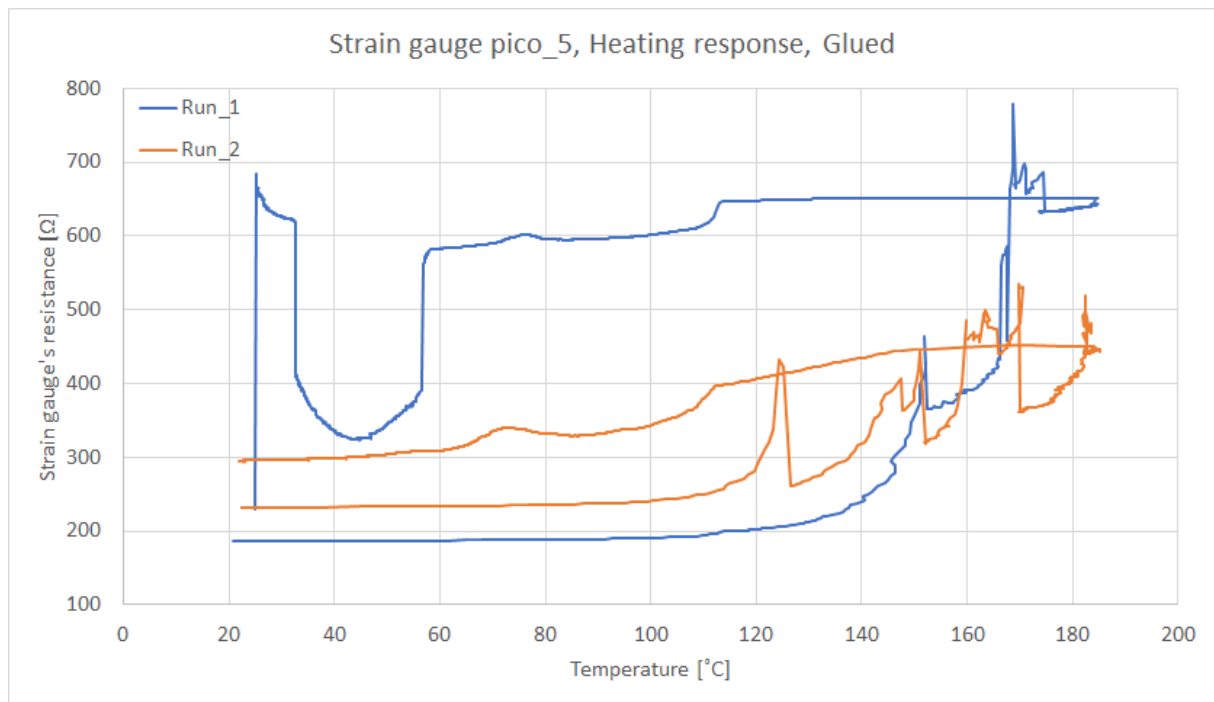


Figure A3-8: Heat response measurements on coupon strain gauge pico_5, with glued contacts.

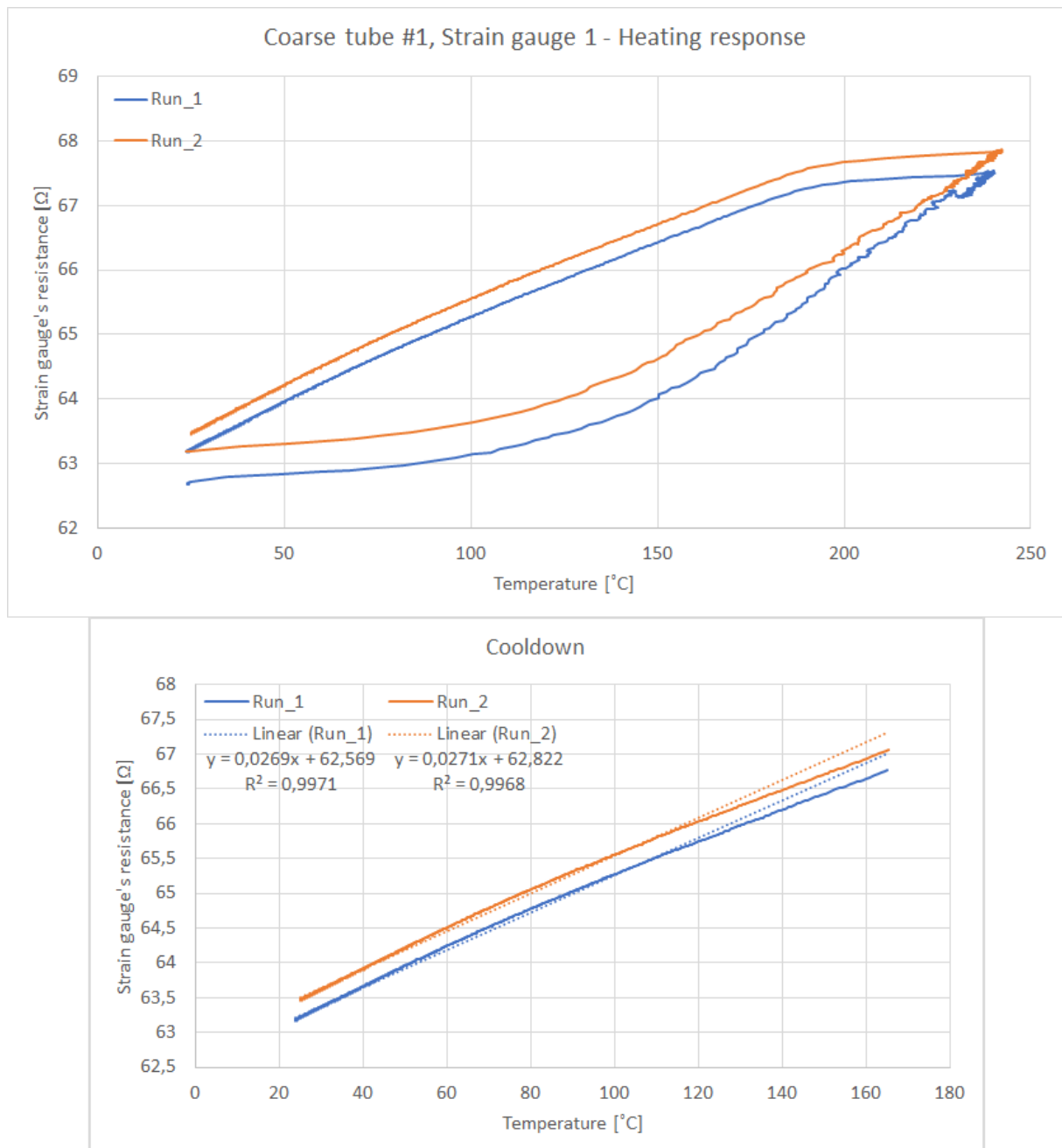


Figure A3-9: Heat response measurements on coarse tube #1 strain gauge 1.

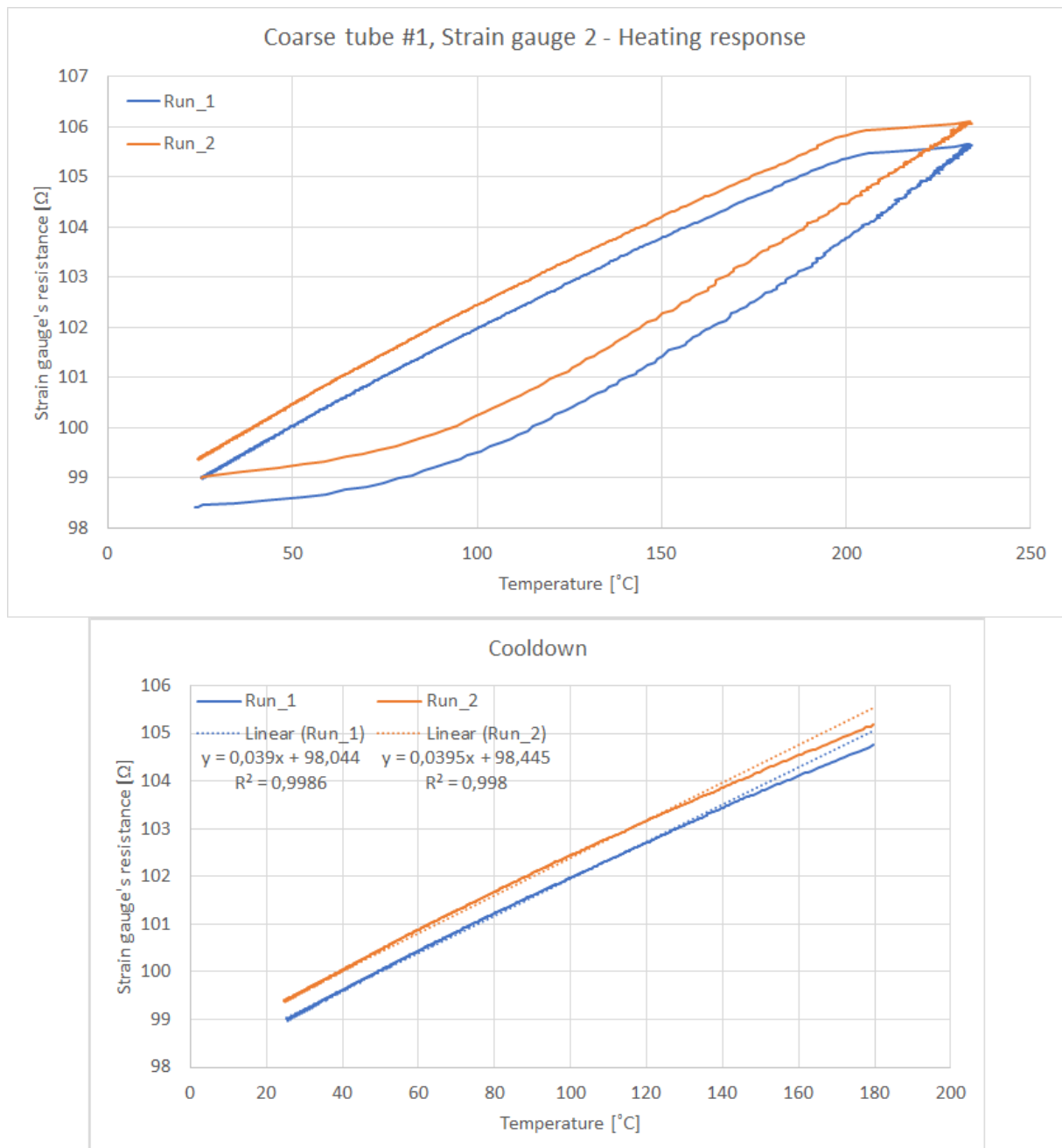


Figure A3-10: Heat response measurements on coarse tube #1 strain gauge 2.

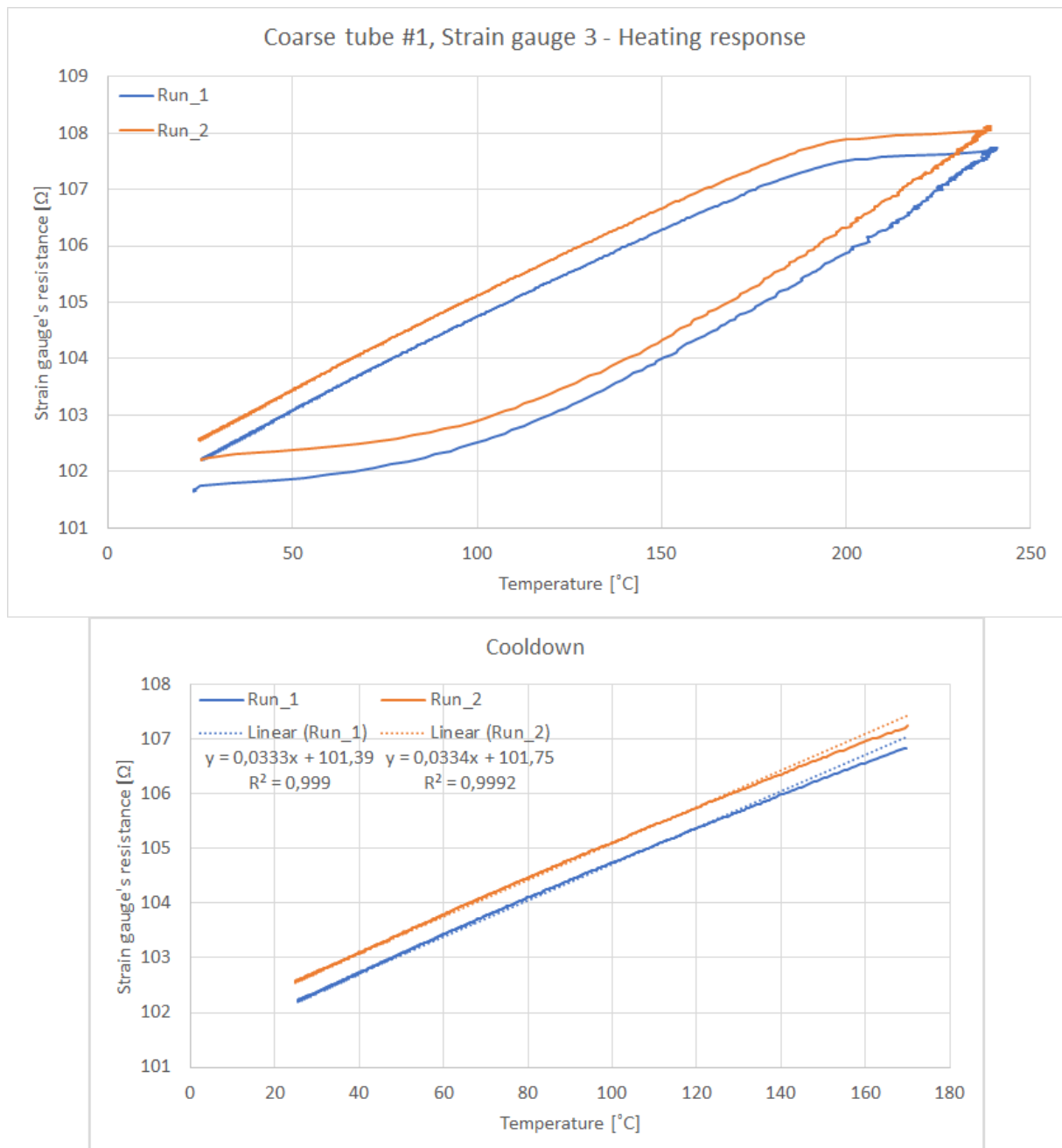


Figure A3-11: Heat response measurements on coarse tube #1 strain gauge 3.

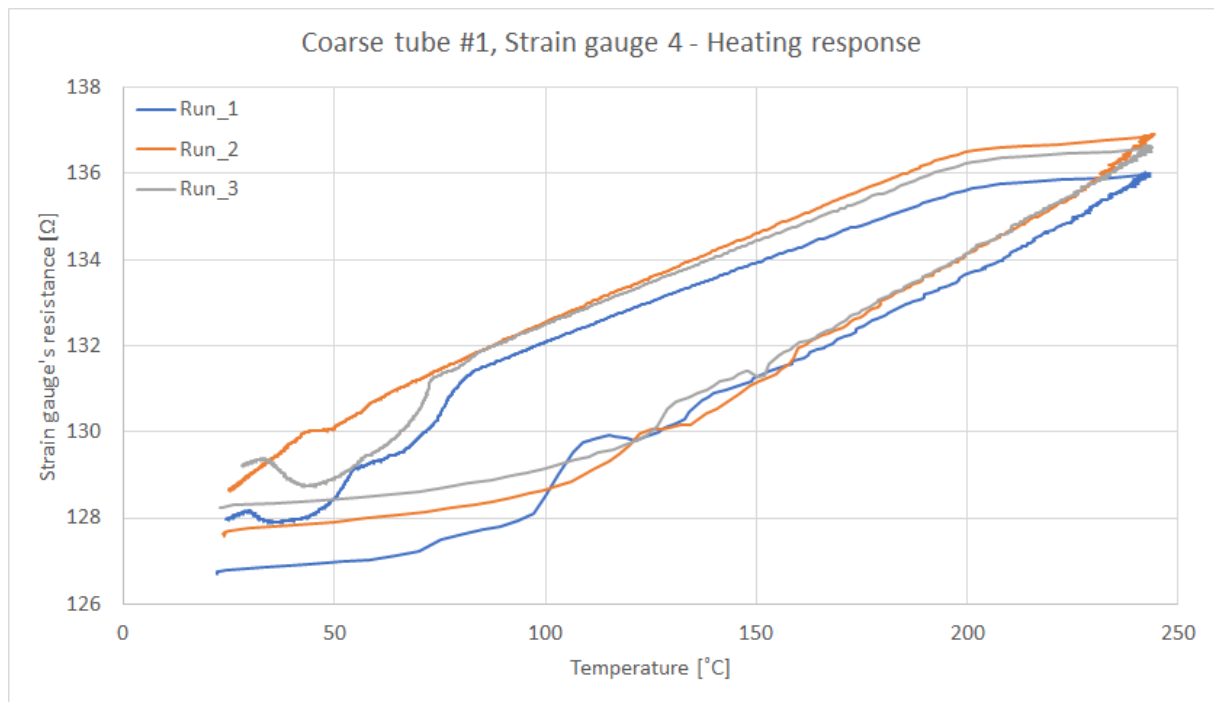


Figure A3-12: Heat response measurements on coarse tube #1 strain gauge 4.

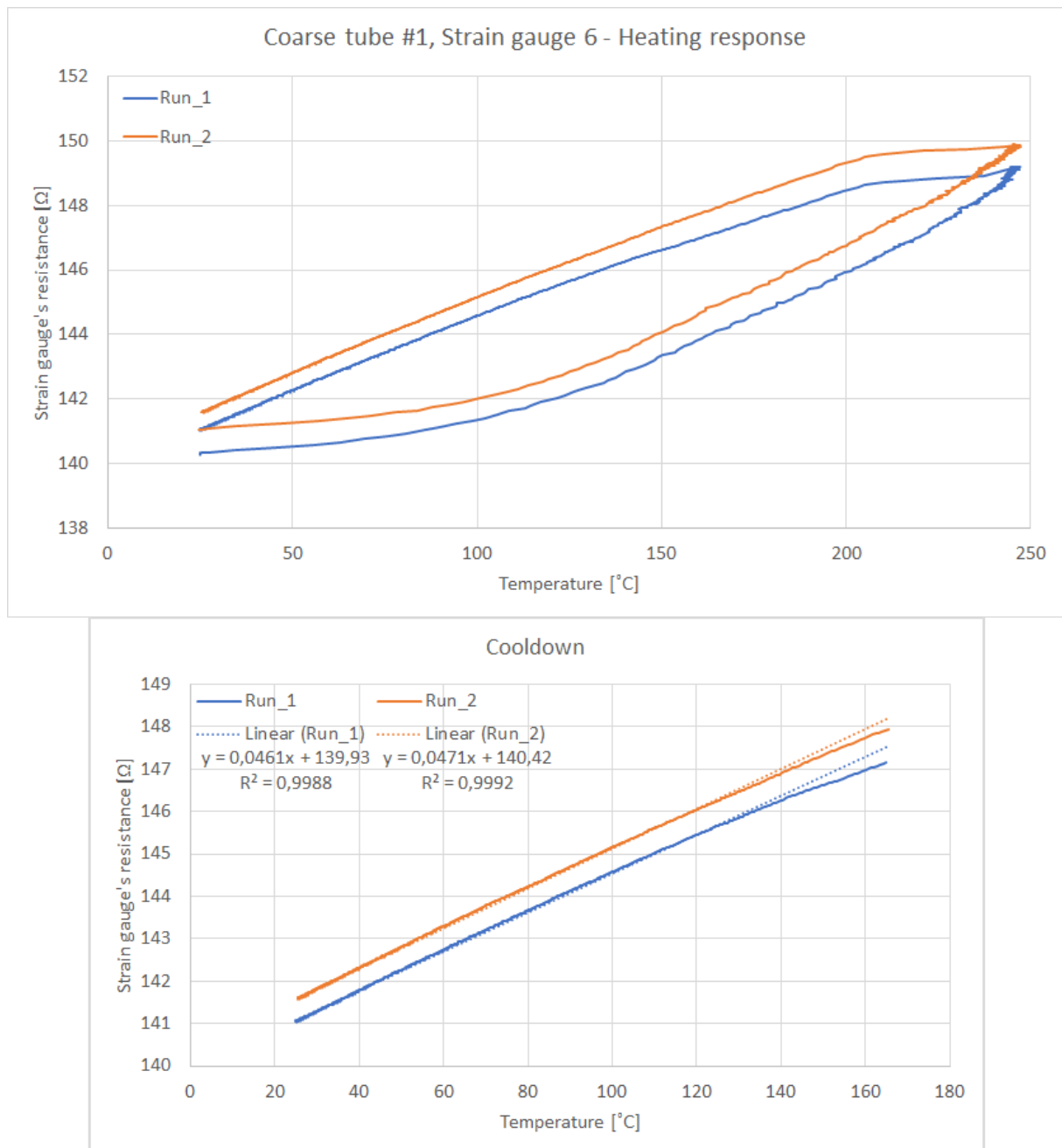


Figure A3-13: Heat response measurements on coarse tube #1 strain gauge 6.

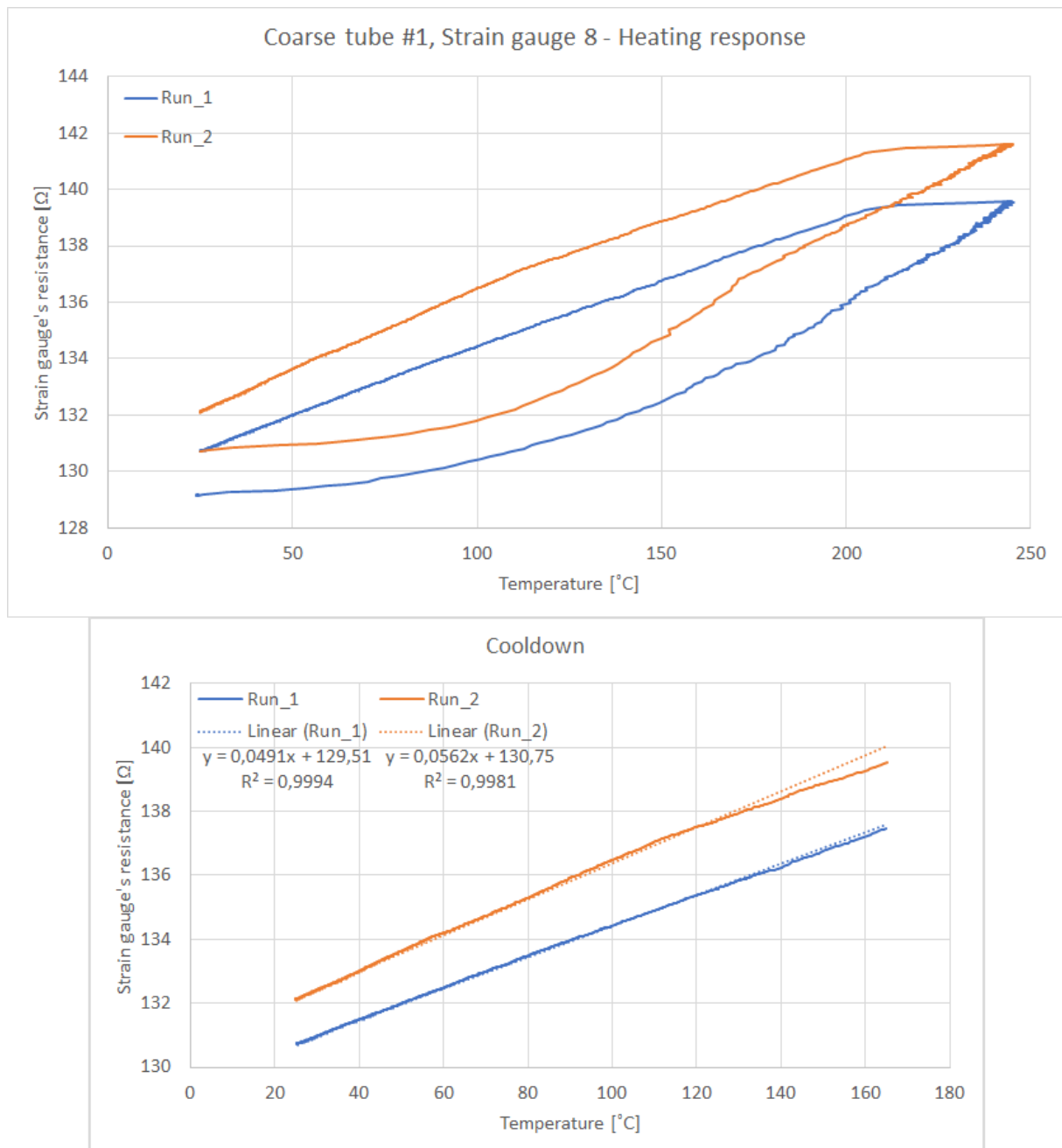


Figure A3-14: Heat response measurements on coarse tube #1 strain gauge 8.

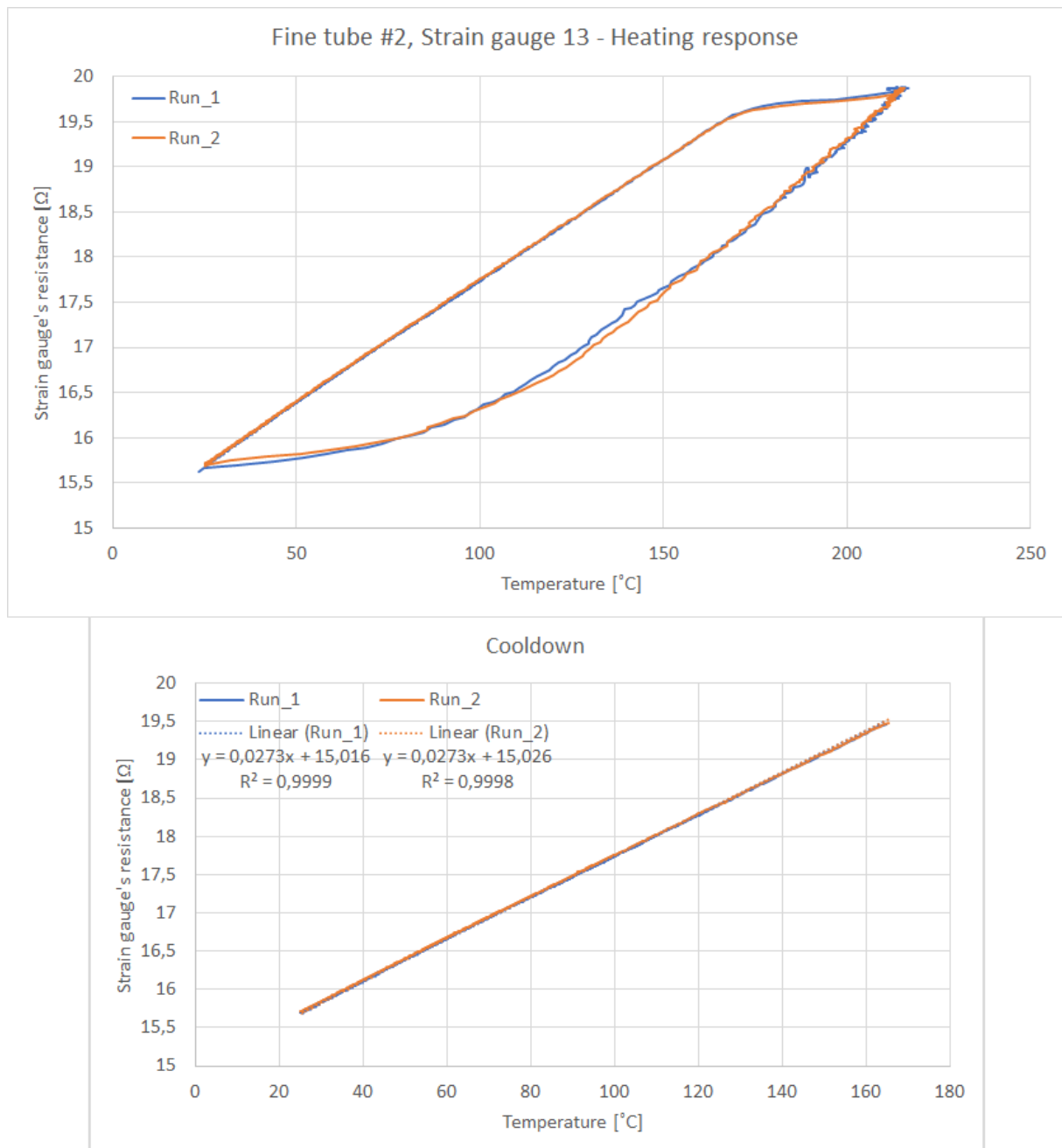


Figure A3-15: Heat response measurements on finegrained tube #2 strain gauge 13.

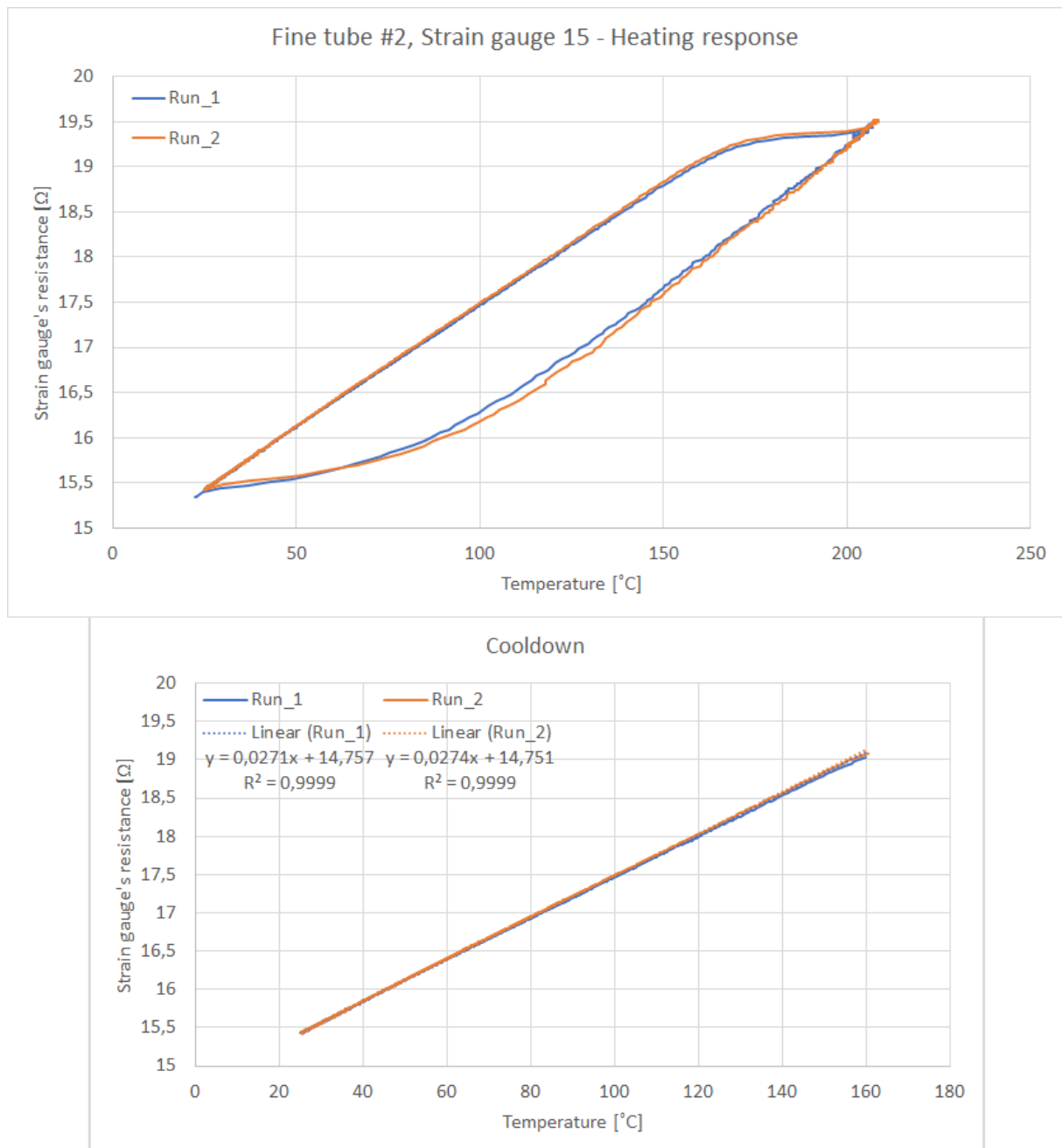


Figure A3-16: Heat response measurements on finegrained tube #2 strain gauge 15.

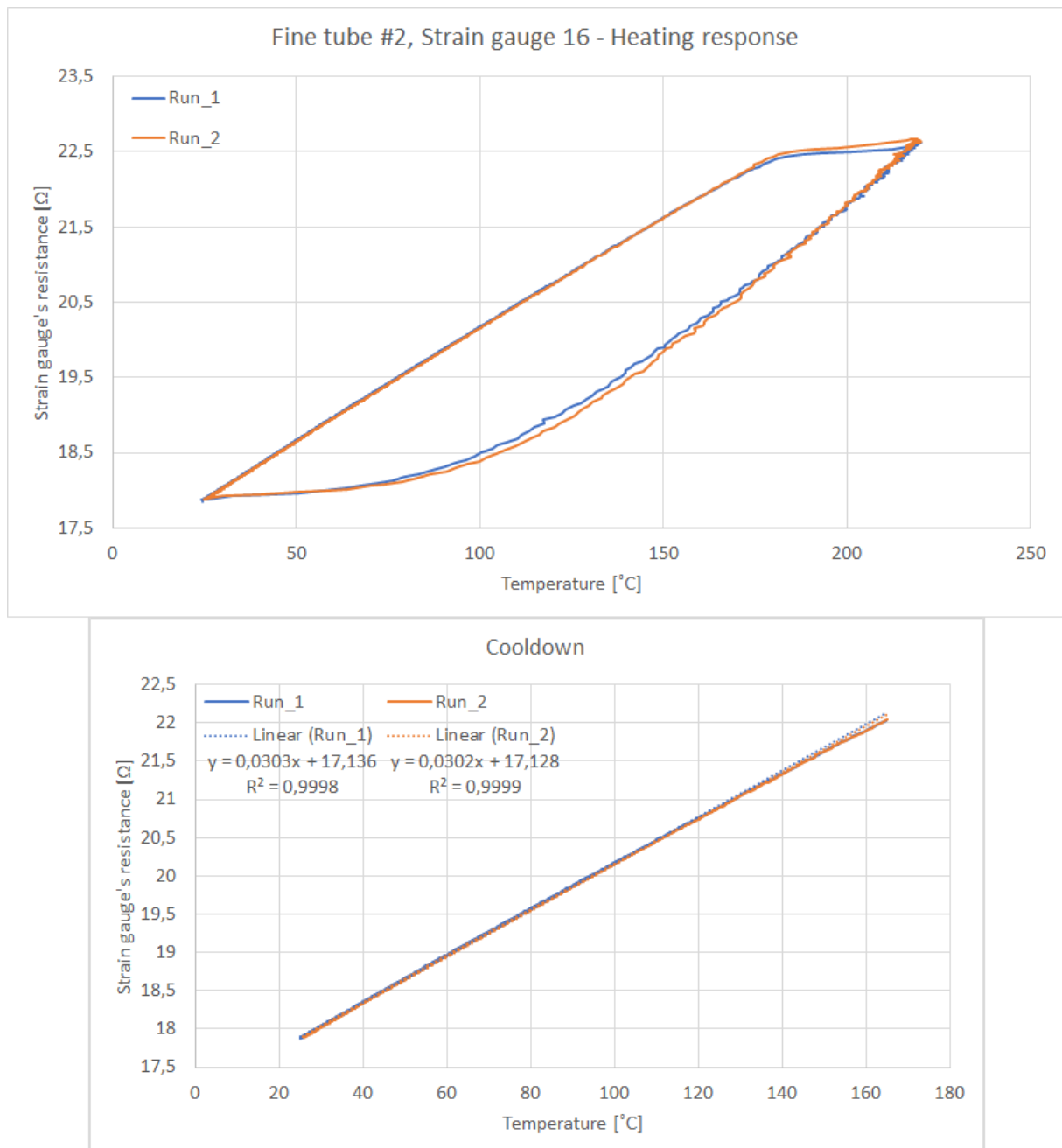


Figure A3-17: Heat response measurements on finegrained tube #2 strain gauge 16.

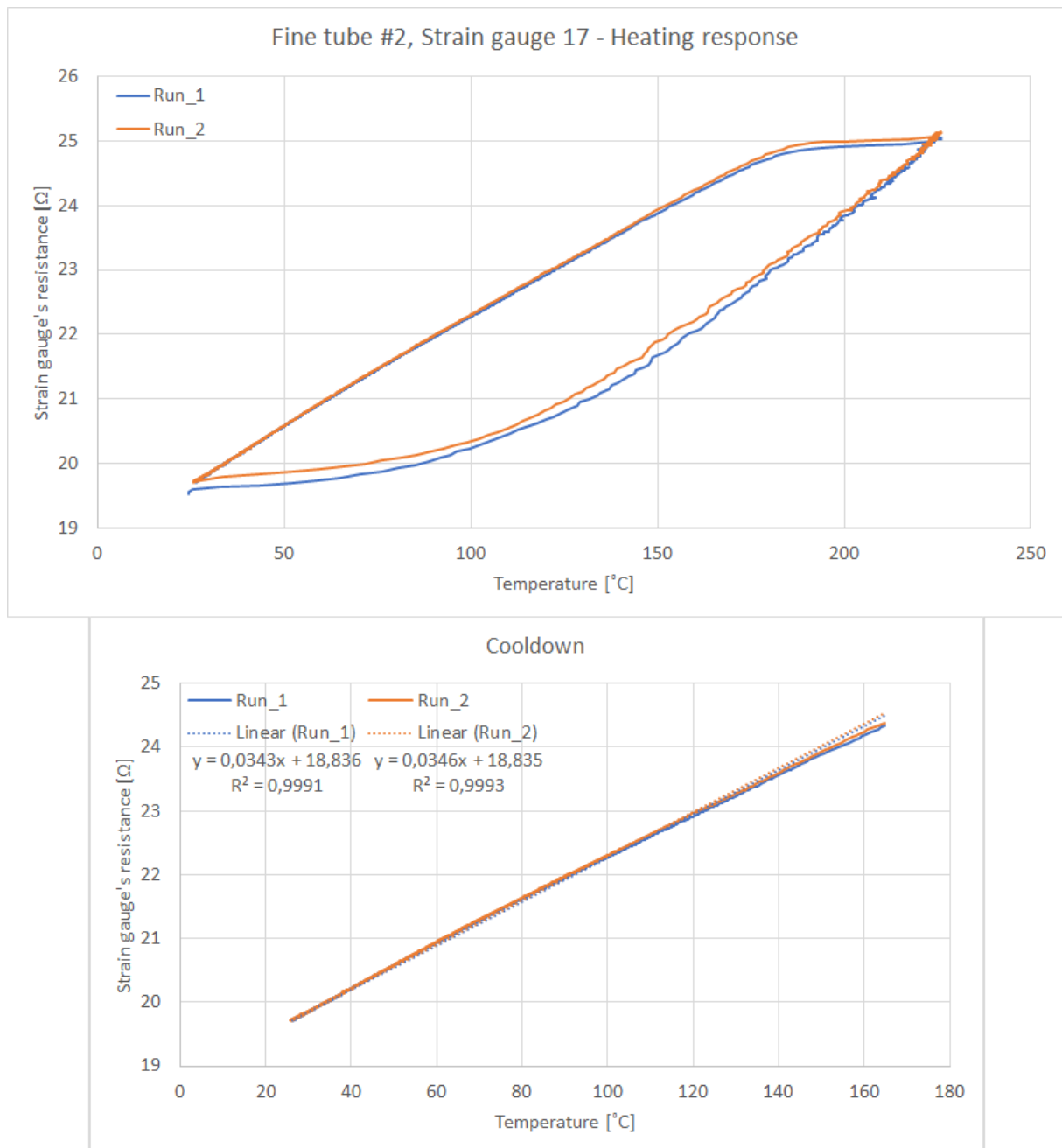


Figure A3-18: Heat response measurements on finegrained tube #2 strain gauge 17.

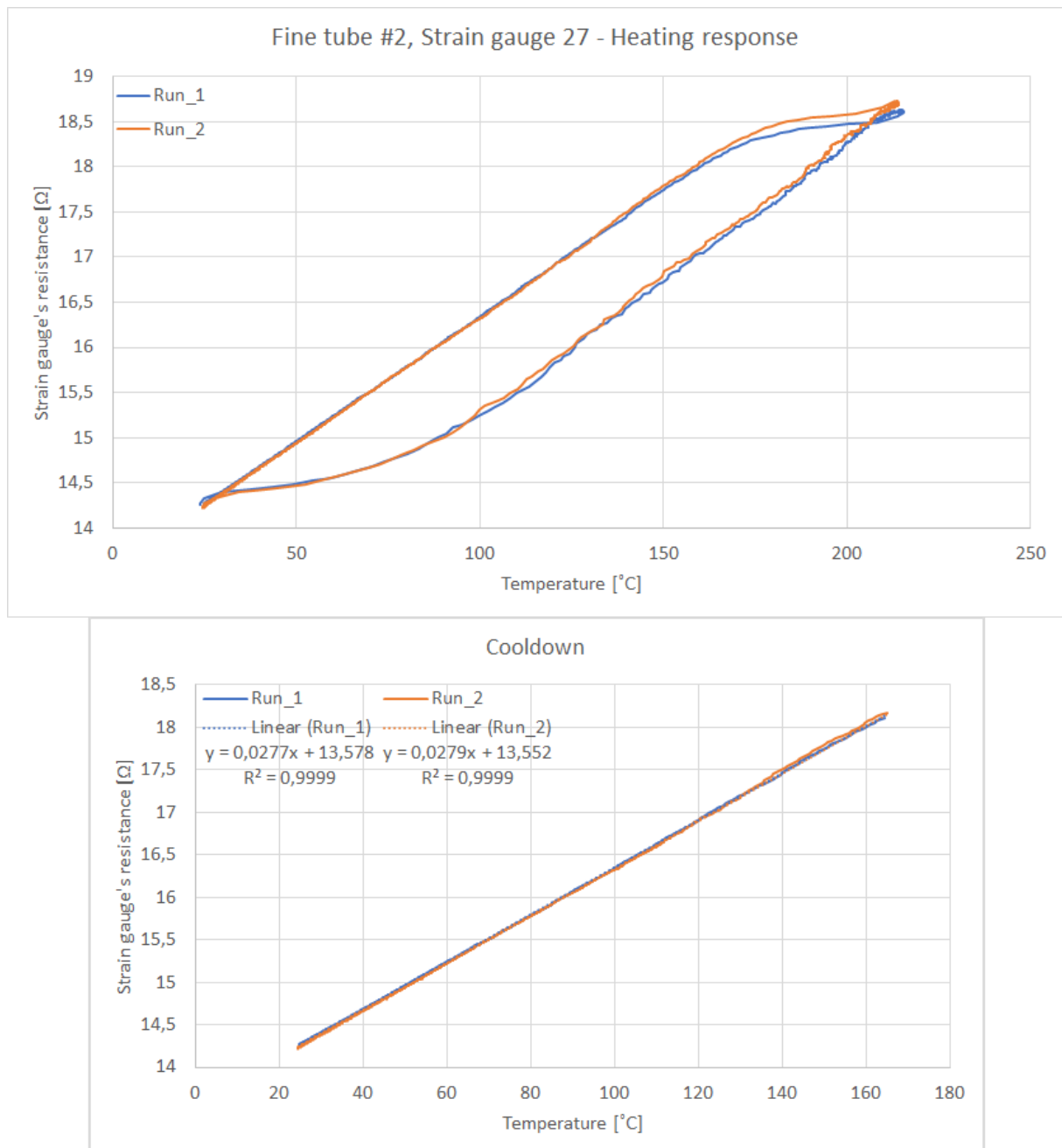


Figure A3-19: Heat response measurements on finegrained tube #2 strain gauge 27.

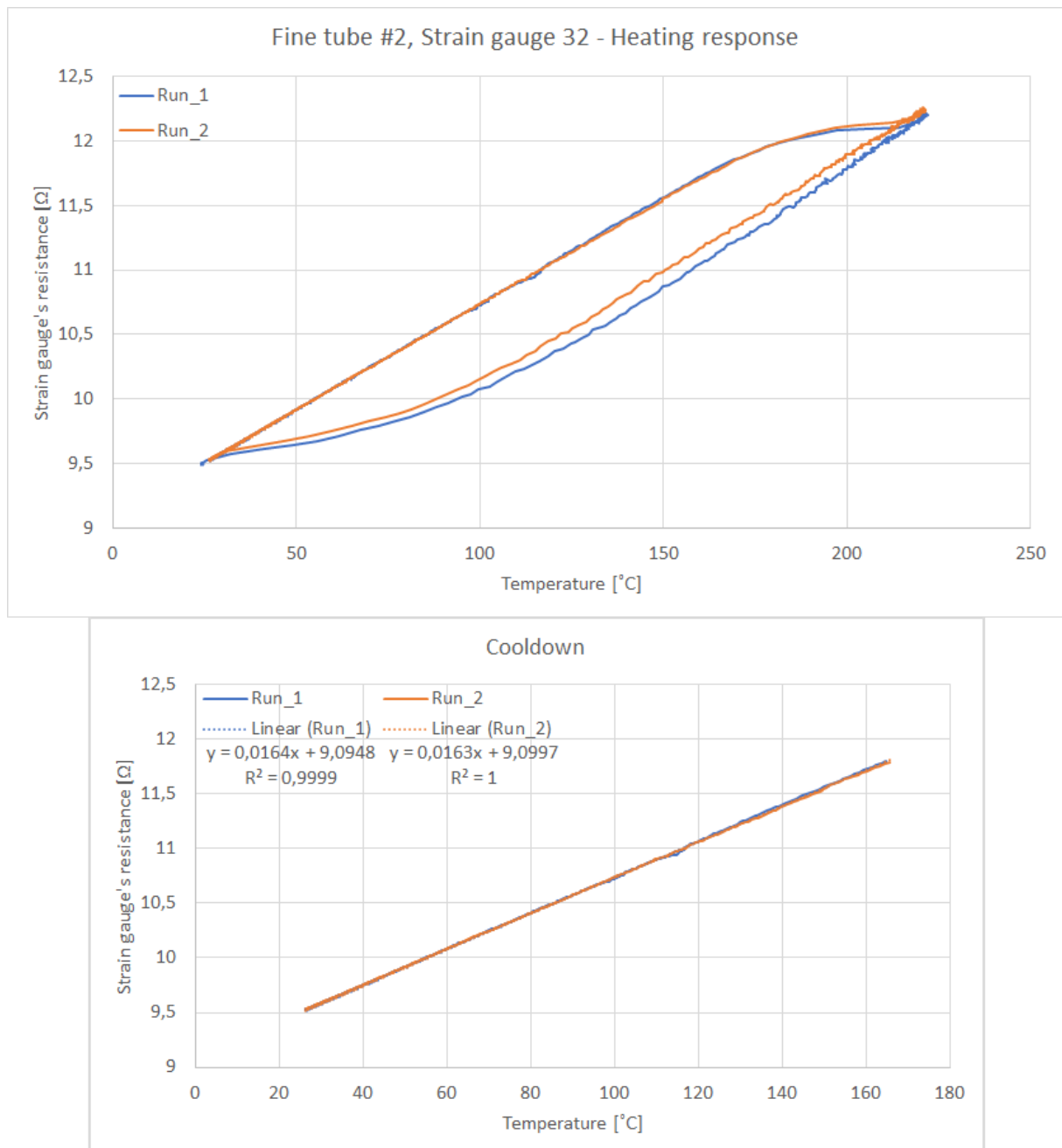


Figure A3-20: Heat response measurements on finegrained tube #2 strain gauge 32.